

INVESTIGATION OF REFRACTORY HIGH ENTROPY ALLOYS FOR EXTREME  
ENVIRONMENT APPLICATIONS

REBECCA ALEXANDRA ROMERO

Doctoral Program in Materials Science and Engineering

APPROVED:

---

Ramana Chintalapalle, Ph.D., Chair

---

Shailendra K. Varma, Ph.D.

---

Arturo Bronson, Ph.D.

---

Ahmed A. El-Gendy, Ph.D.

---

Irene Beyerlein, Ph.D.

---

Stephen L. Crites, Jr., Ph.D.  
Dean of the Graduate School

Copyright ©

by

Rebecca Alexandra Romero

2022

## **Dedication**

Throughout my entire academic journey, I have had several people who have stuck by my side and supported me through both the good times and bad. I cannot express how much I appreciate the role that every one of my family, friends, and loved ones has played. To my parents, thank you for being my biggest supporters and helping me grow into the person I am today. None of this would have been possible without you. Your unconditional love and guidance have gotten me here. To my Grandma Dora, you have been my rock through it all and I am proud to be your granddaughter. Completing this journey with you by my side has been one of the most rewarding things I could have done. And for Jeffrey, thank you for getting me through the last couple of years. There are days I don't know that I could have done this without you. I appreciate the patience and understanding you've had.

INVESTIGATION OF REFRACTORY HIGH ENTROPY ALLOYS FOR EXTREME  
ENVIRONMENT APPLICATIONS

by

REBECCA ALEXANDRA ROMERO

DISSERTATION

Presented to the Faculty of the Graduate School of  
The University of Texas at El Paso  
in Partial Fulfillment  
of the Requirements  
for the Degree of

DOCTOR OF PHILOSOPHY

Doctoral Program in Materials Science and Engineering

THE UNIVERSITY OF TEXAS AT EL PASO

May 2022

## **Acknowledgements**

I feel honored to have been a part of the MMBME family here at UTEP. The support offered by the entire department has been a wonderful experience. Thank you to all the professors who have helped mentor and guide me throughout both my undergraduate and graduate career. A special thank you to Dr. Binata Joddar, Dr. S.K. Varma, and Dr. Stella Quinones, you all have supported me and helped make this possible. Your belief has helped me push through along the way. I would like to thank my advisor, Dr. Chintapalle Ramana, for providing me the opportunity to work on this project and for awarding me opportunities to further my career. I would also like to thank my committee members, Dr. S.K. Varma, Dr. Arturo Bronson, Dr. Ahmed El-Gendy, and Dr. Irene Beyerlein. I appreciate your time and guidance, for which this project would not have been possible.

I am grateful for the generous funding contributions, including the Patricia and Jonathan Rogers Scholarship for Graduate Engineering Students and the Nuclear Regulatory Commission that assisted me to complete my degree.

I extend my deepest appreciation and sincere gratitude to all.

## Abstract

High entropy alloys (HEAs) have emerged as an exciting class of materials with the potential for a wide range of structural, high-temperature applications. HEAs may be defined on a compositional basis as five or more principal elements in equimolar ratios. This definition led to the term “high entropy” due to the high configurational entropy which is obtained with principal elements in these amounts. The combination of elements has contributed to materials that may favor solid-solution phases over intermetallic phases and have the potential to possess highly desired material properties including high yield and creep strength. The inclusion of refractory metals into these alloys further expands their application potential. In fact, several refractory high entropy alloys (RHEAs) have been explored in recent years. The MoNbTaW RHEA has been one of the first and most significant ones in this family. While current interests span various compositions, the attention is focused on CrNbTaVW and CrMoNbTaW RHEAs for their application in extreme environments. The CrMoNbTa in the as-received condition processed through vacuum arc melting was found to be a multiphase microstructure containing three phases. The microstructure was assessed after a 6-hour anneal in the temperature range of 600-900°C for which it was thermally stable. The oxidation resistance was evaluated in the temperature range of 600-1400°C for both 12 and 24 hours, obtaining a moderate oxidation resistance. The surface oxidation scale was found to consist of two main oxides of Cr-Nb-Ta and Ta-Nb-W which become more defined at high temperatures. Atomistic simulations on the dislocation behavior for this alloy family were also performed. The stress required to move a dislocation improved in HEA compositions as compared to the pure metals. It was found that Cr-containing compositions obtain higher strength values which were believed to be influenced by the increase in lattice distortion. Long dislocations of pure metals and HEA compositions were evaluated in both a void-free and

void-containing lattice. The presence of an obstacle such as a void improved the strengthening of pure metals and HEAs. The combined experimental and theoretical results of the present work provide fundamental insights into these RHEAs to design advanced materials for high-temperature applications.

## Table of Contents

Dedication .....	iii
Acknowledgements .....	v
Abstract .....	vi
Table of Contents .....	viii
List of Tables .....	xi
List of Figures .....	xiii
Chapter One: Introduction .....	1
1.1 History of High Entropy Alloys.....	1
1.2 Concepts of High Entropy Alloys.....	2
1.3 Core Effects of High Entropy Alloys.....	6
1.3.1 High Entropy Effect.....	7
1.3.2 Lattice Distortion Effect .....	8
1.3.3 Sluggish Diffusion Effect .....	9
1.3.4 “Cocktail” Effect.....	9
1.4 Taxonomy of High Entropy Alloys .....	10
1.5 Refractory High Entropy Alloys .....	10
1.5.1 Basic Properties of Common Refractory Elements .....	11
1.5.2 Oxidation Data of Refractory Metals.....	12
1.5.3 Hume-Rothery Rules for Refractory Metals.....	13
1.5.4 Potential Applications for Refractory High Entropy Alloys.....	14
1.5.5 Mechanical Properties of Refractory High Entropy Alloys.....	16
1.5.6 Oxidation of Refractory High Entropy Alloys.....	19
1.5.7 Annealing of Refractory High Entropy Alloys.....	20
1.6 Atomistic Simulations and Plastic Deformation Behavior of High Entropy Alloys.....	21
Chapter Two: Research Problem .....	24
2.1 Introduction.....	24
2.2 Statement of the Problem.....	24
2.3 Significance of the Study .....	25

2.4 Research Objectives.....	26
Chapter Three: Experimental Procedures .....	27
3.1 Fabrication of the Alloys .....	27
3.2 Characterization of the As-Received Alloys.....	27
3.3 Oxidation Experiments .....	27
3.4 Oxidized Sample Characterization .....	28
3.5 Annealing Experiments.....	28
3.6 Annealed Sample Characterization.....	29
Chapter Four: Experimental Results and Discussion.....	30
4.1 CrNbTaVW Alloy.....	30
4.1.1 X-Ray Diffraction .....	31
4.1.2 Oxidation of a CrNbTaVW HEA .....	32
4.1.2.1 Cross-Sectional Substrate-Oxide Interface .....	33
4.1.2.2 Surface Analysis .....	38
4.1.2.3 Oxide Growth-High Temperature XRD .....	40
4.1.2.4 Further Discussion .....	42
4.2 CrMoNbTaW Alloy .....	43
4.2.1 As-Received Characterization of the CrMoNbTaW HEA.....	43
4.2.1.1 SEM/EDS Analysis.....	43
4.2.1.2 Microhardness.....	45
4.2.2 Annealed Characterization.....	46
4.2.3 Oxidation of a CrMoNbTaW HEA.....	49
4.2.3.1 12 Hour Oxidation .....	50
4.2.3.2 24 Hour Oxidation .....	55
4.3 Discussion of Alloys .....	58
Chapter Five: Atomistic Simulations Results and Discussion.....	61
5.1 Introduction.....	61

5.2 Molecular Statics Simulation Details.....	62
5.3 Molecular Statics Results.....	64
5.3.1 Lattice Parameters and Elastic Constants .....	64
5.3.2 Generalized Stacking Fault Energy .....	66
5.3.3 Local Slip Resistance.....	74
5.3.3.1 Peierls Stresses in Pure Metals and A-atom Potential Based MPEAs....	74
5.3.3.2 LSR Values: Mean and Distribution.....	76
5.3.3.3 Slip Plane Anisotropy .....	79
5.3.3.4 Correlation Between the Ideal Shear Strength and the Mean LSR.....	83
5.3.4 Lattice Distortion .....	84
5.3.5 Further Discussion .....	86
5.4 Molecular Dynamics Simulation Details .....	88
5.4.1 Molecular Dynamics Results .....	89
5.4.1.1 Critical Resolved Shear Stresses in Pure Metals .....	91
5.4.1.1 Critical Resolved Shear Stresses in HEAs.....	93
Chapter Six: Conclusions.....	97
References.....	100
Vita 109	

## List of Tables

Table 1: Basic properties of the six refractory metals used in this work.....	12
Table 2: Oxide formation energies of common oxides of constituent elements used in this work. .....	13
Table 3: Crystal structure, atomic radius, electronegativity, and valence of each constituent elements and the binary combinations to abide the Hume-Rothery rules. ....	14
Table 4: Specific alloy compositions of two RHEAs. ....	27
Table 5: Equipment information and operating parameters. ....	29
Table 6: Microhardness values of the as-received CrMoNbTaW alloy of the polished sample. .	46
Table 7: Microhardness results of the annealed samples at their respective temperatures after 6 hours.....	49
Table 8: Lattice parameter and elastic constants for pure metals. Both MS and experimental values are provided. ....	65
Table 9: Lattice parameter and elastic constants of the four MPEAs calculated by MS and DFT. Experimental values are provided, when available. Spin-polarization is not considered in any DFT calculations. MSSNAP results were based on a spectral neighbor analysis potential [23A]. Subscripts A and V denote results based on A-atom potentials and simple rule of mixtures, respectively. ....	65
Table 10: USFE values (in mJ/m <sup>2</sup> ) of pure metals from both MS and DFT calculations. For Cr, DFT results without spin-polarization are presented here. ....	70
Table 11: Ideal shear strength values (in GPa) of the reference pure metals for both MS and DFT calculations. For Cr, DFT results without spin-polarization are presented here. ....	73
Table 12: Peierls stresses and LSR values, in units of MPa, of (a) pure metals, (b) MPEAs based on simple rule of mixtures estimation, (c) MPEAs based on A-atom potentials, and (d) MPEAs based on alloy potentials.....	75
(a) Peierls stresses of six pure metals .....	75
(b) Simple rule of mixtures estimation of the LSR in MPEAs using the reference pure metals Peierls stress.....	75
(c) Peierls stresses of four MPEAs using the <i>A</i> -atom potentials .....	75
(d) Mean LSR values of four MPEAs using the alloy potentials. Note, there is no standard deviation for the MoNbTaW screw dislocation on the {110} plane as there was only one calculable result. ....	76
Table 13: COV across all planes for each dislocation. ....	81
(a) COV of the four MPEAs based on alloy potentials across all three planes for each dislocation type.....	81
(b) COV of the four MPEAs based on A-atom potentials across all planes for the edge dislocation. ....	81
(c) COV of the Peierls stresses of the individual metals across all planes for the edge dislocation. ....	81
Table 14: Screw-to-edge ratios in (a) pure metals, (b) MPEAs with A-atom potentials, and (c) MPEAs with alloy potentials. ....	82
(a) Screw-to-edge ratio of the Peierls stresses in pure metals .....	82
(b) Screw-to-edge ratio of the Peierls stresses in <i>A</i> -atom potential-based MPEAs.....	83
(c) Screw-to-edge ratio of the LSR in alloy potential-based MPEAs.....	83
Table 15: Calculated lattice distortion $\delta$ values for the four MPEAs. ....	85

Table 16: CRSS of pure metals for both gliding and void-containing lattice.....	92
Table 17: CRSS for gliding and void-containing lattices. ....	94

## List of Figures

Figure 1: The entropy of mixing based on the number of elements in an equimolar alloy.....	5
Figure 2: Calculated Configurational Entropies of Traditional Alloys of data obtained from [18i]. .....	6
Figure 3: A schematic representation of the relationship between the structure, properties, processing, and performance of materials.....	7
Figure 4: Comparison of a perfect lattice and a distorted lattice.....	8
Figure 5: XRD data of the as-fabricated CrNbTaVW alloy produced by vacuum arc melting....	32
Figure 6: Oxide-layer substrate interface of the sample oxidized for 24 hours at 700 <sup>0</sup> C. EDS spot analysis is included for reference.....	34
Figure 7: Color mapping of the oxide-layer substrate interface of the sample oxidized for 24 hours at 700 <sup>0</sup> C. EDS spot analysis is included for reference.....	35
Figure 8: Interface of the sample oxidized for 24 hours at 700 <sup>0</sup> C.....	36
Figure 9: Interface of the substrate-oxide layer of the sample oxidized at 800 <sup>0</sup> C for 24 hours showing severe cracking and porosity at the interface.....	37
Figure 10: Interface of the substrate-oxide layer indicating the thickness of the sample oxidized at (a) 700 <sup>0</sup> C and (b) 800 <sup>0</sup> C.....	38
Figure 11: Surface of the oxide layer at 700oC after 48h in the BSE mode. The two main oxides are visible, the granular Cr oxide containing Ta and Nb with low amounts of V and W present. A whisker-like W oxide growing outwards from the Cr oxide.....	39
Figure 12: Surface of the oxide layer of the 800oC after 48h sample in the BSE mode. The granules of the Cr oxide have become more defined and contain a higher content than that seen at 700oC. The W oxide has become thicker and is more prominent.....	40
Figure 13: Surface of the oxide layer at a) 700oC for 48h and b) 700oC for 48h. The difference between the morphology is visible.....	40
Figure 14: In-situ XRD of the CrNbTaVW HEA.....	42
Figure 15: Microstructure of the as-received CrMoNbTaW fabricated by vacuum arc melting..	44
Figure 16: Microstructure of the as-received CrMoNbTaW alloy showing grain boundaries with Cr precipitation.....	45
Figure 17: Microstructures of the samples at their respective annealing temperatures after 6 hours.....	47
Figure 18: EDS color mapping of the four annealed samples at each respective temperature after 6 hours. The corresponding map sum spectrum providing the overall composition is provided in atomic percentage.....	48
Figure 19: Oxidation curves of the mass change per surface area after 12 and 24 hours of oxidation in air versus time.....	50
Figure 20: Surface oxide morphologies of the scale at each respective temperature after 12 hours of oxidation in air.....	51
Figure 22: EDS color maps of the oxide scale after 12 hours of oxidation in air at 1100 <sup>0</sup> C.....	53
Figure 22: EDS color maps of the oxide scale after 12 hours of oxidation in air at 600 <sup>0</sup> C.....	52
Figure 23: EDS color maps of the oxide scale after 12 hours of oxidation in air at 1300 <sup>0</sup> C.....	53
Figure 24: XRD of the oxidized samples after 12 hours of oxidation in air.....	54
Figure 25: Surface oxide morphologies of the scale at each respective temperature after 24 hours of oxidation in air.....	56
Figure 27: EDS color maps of the oxide scale after 24 hours of oxidation in air at 1400 <sup>0</sup> C.....	57

Figure 26: EDS color maps of the oxide scale after 24 hours of oxidation in air at 1100°C.....	56
Figure 28: XRD of the oxidized samples after 24 hours of oxidation in air.....	58
Figure 29: GSFE curves of four MPEAs on a) {110}, b) {112}, and c) {123} planes based on MS simulations using the alloy and A-atom potentials (subscript “A”).....	69
Figure 30: Average USFE values of MPEAs in the three planes and the COV.....	70
Figure 31: Average ideal shear strength (ISS) values of four MPEAs in three slip planes and the COV for each composition .....	73
Figure 32: Distribution of the LSR of the four MPEAs on the (a) {110} edge plane, (b) {110} screw plane, (c) {112} edge plane, (d) {112} screw plane, (e) {123} edge plane, and the (f) {123} screw plane.....	79
Figure 33: Mean local slip resistance (MPa) versus the ideal shear strength (GPa) for (a) edge and (b) screw dislocations in the four MPEAs. ....	84
Figure 34: Plot of (a) normalized LSR, (b) normalized USFE, and (c) normalized ideal shear strength, with respect to the lattice distortion, in four MPEAs.....	86
Figure 35: Depiction of the dislocation position according to the values indicated on the stress- strain curve.....	90
Figure 36: The stress-strain curves of pure metals in a void-free lattice. ....	91
Figure 37: The stress-strain curves of pure metals in a void-containing lattice. ....	92
Figure 38: The strengthening effect of void-containing lattices.....	93
Figure 39: The ratio of the CRSSvoid/CRSSglide to represent the strengthening effect of voids present in the lattice. ....	96
Figure 39: The CRSS of the gliding and void-containing cases of the HEAs as a function of x, Mo content .....	95

## **Chapter One: Introduction**

### **1.1 History of High Entropy Alloys**

Looking back through history, as far as the Stone Age, material alloying has been an important concept for the applications of everyday life. Some of the earliest metallic alloys to come about included bronze, steel, and copper alloys. Many of these early alloys followed the concept of conventional alloying techniques: using a single principal component and then adding small additions of various other components to enhance the material. Materials research has commonly focused on improving the properties of conventional alloys until a new concept arose in 2004. This year marked the first two publications on multicomponent alloys. The Yeh et al. group studied the CuCoNiCrAl<sub>x</sub>Fe system and found that the alloys exhibited a simple structure rather than a complex one, as was expected, containing intermediate and intermetallic phases [1]. The Cantor et al. group also studied an equiatomic FeCrMnNiCo alloy which formed a single FCC solid solution [2]. The result of such simple solid solution structures was believed to have been a result of the high entropy obtained from the equiatomic amounts of each element. This gave rise to the name high entropy alloys (HEAs), as they are commonly referred to now. While many in the HEA community believe 2004 marks the beginning of this alloy research, both the Yeh group and Cantor group began research on this work several years prior [3]. During the 1990s, Yeh began experimenting with multicomponent alloys, as he believed a high entropy of mixing because of the components would contribute to a reduced number of phases. Until 2004, the work on these studies was only published as twelve master's theses. [4-15]. The Cantor group also began their work prior to the first published article in 2004 [3]. In 1981 Cantor had an undergraduate student begin work on the FeCrMnNiCo alloy. This work was continued by a subsequent master's student. The work of both students was only published as theses prior to 2004 but contributed to the bulk

of the published article. Both Yeh and Cantor are renowned as pioneers of high entropy alloys and sparked what has led to nearly 20 years of materials research.

## 1.2 Concepts of High Entropy Alloys

A formal, agreed-upon definition of high entropy alloys has been discussed and disputed consistently as research has continued. Some researchers have regarded high entropy alloys be defined based on composition, while some believe that entropy is the primary factor. Regardless of definition, the main objective of high entropy alloys is motivated by creating single-phase solution alloys rather than those with intermetallic or intermediate phases. The belief is that alloys of this nature will exhibit superior properties to those obtained by conventional alloys. There are three primary definitions that have been accepted to define high entropy alloys and are subsequently discussed below.

The work of Yeh et al. provided the first composition-based definition of high entropy alloys. The work in 2004 stated that HEAs are defined as those alloys composed of five or more principal elements in equimolar ratios [1]. This work allowed the possibility to extend the scope of alloys for the composition-based definition by noting that these alloys may contain principal elements of a composition ranging between 5 and 35% atomic percent. The definition based solely on composition does not use entropy as a factor and places no condition on the formation of solid solution formation [16]. This composition-based definition provides a vast space for potential alloy compositions.

High entropy alloys may also be classified considering the magnitude of entropy of an alloy. Entropy is considered based on a thermodynamic system that attempts to reach equilibrium by minimizing the value of Gibbs free energy of a system [17] following

$$G = H - TS \quad (1)$$

Prediction of the lowest energy state of an alloy may be compared with the free energy of mixing ( $\Delta G_{mix}$ ) of different states to identify which bears the lowest  $\Delta G_{mix}$ . The changes in free energy of mixing can be identified by

$$\Delta G_{mix} = \Delta H_{mix} - T\Delta S_{mix} \quad (2)$$

where  $\Delta H_{mix}$  is the enthalpy of mixing and  $\Delta S_{mix}$  is the entropy of mixing [17]. According to the Boltzmann hypothesis, the configurational entropy of mixing for an n-element equimolar alloy is calculated from:

$$\Delta S_{mix} = R\ln(n) \quad (3)$$

Where R is the gas constant (8.314 J/mol K) [1]. Figure 1 below plots the entropy of mixing calculated following Equation 3 according to the number of equimolar components used in an alloy. The plot illustrates that an increase in the number of elements increases the entropy of mixing for a system, which is believed to contribute to the solid solution phase formation. A value of five elements is chosen as the lower bounds, as it is considered the point at which the entropy of mixing will counterbalance the enthalpy of mixing, thus minimizing the value of the free energy of mixing [17].

Following the principle of calculating the entropy of mixing, alloys can be classified based on the magnitude of entropy from the number of elements utilized for equimolar alloys. Multiprincipal element alloys can be classified following the criteria [17]:

Low Entropy Alloys:  $\Delta S_{conf} \leq 0.69R$

Medium Entropy Alloys:  $0.69R \leq \Delta S_{conf} \leq 1.61R$

High Entropy Alloys:  $\Delta S_{conf} \geq 1.61R$

The plot within figure one calculates the configurational entropy for various  $n$ -values of elements. A value of five elements satisfies the definition of a high entropy alloy. The entropy-

based definition outlined above classifies alloys based solely on equiatomic compositions, however, the potential exists that the alloy may not always be equiatomic. To evaluate alloys that are not equiatomic based on entropy, Yeh [18] outlined an alternative way to evaluate the configurational entropy for a system. The configurational entropy of a system ( $\Delta S_{\text{config}}$ ) can be calculated by the summation equation:

$$\Delta S_{\text{config}} = -R \sum_{i=1}^n X_i \ln X_i \quad (4)$$

where  $X_i$  is the mole fraction of the  $i$ th component and  $R$  is the gas constant [18]. A lower bound of  $1.5R$  was selected as a reasonable value to classify an HEA since it is just below the equiatomic value of  $1.61R$ , yet higher than the value of  $1.39R$  for an equimolar quaternary alloy and believed to be large enough to compete with the enthalpy of mixing. Thus, to classify alloys that are not equiatomic, the following criteria applies:

Low Entropy Alloys:  $\Delta S_{\text{conf}} \leq 1R$

Medium Entropy Alloys:  $1R \leq \Delta S_{\text{conf}} \leq 1.5R$

High Entropy Alloys:  $\Delta S_{\text{conf}} \geq 1.5R$

For both classifications, whether equiatomic or not, alloys may generally be regarded as “high entropy” alloys when containing five or more principal elements, “medium entropy” when containing three or four principal elements, and “low entropy” alloys when containing only one or two principal elements. Using data obtained from [18], figure two plots the configurational entropies of commonly used commercial alloys. It is evident that most commercial alloys have a low entropy, with some ranging into the medium range and none reaching the high entropy value above 1.5R. This indicates that HEAs may have a greater potential to promote solid solution formation and thus lead to enhanced materials properties.

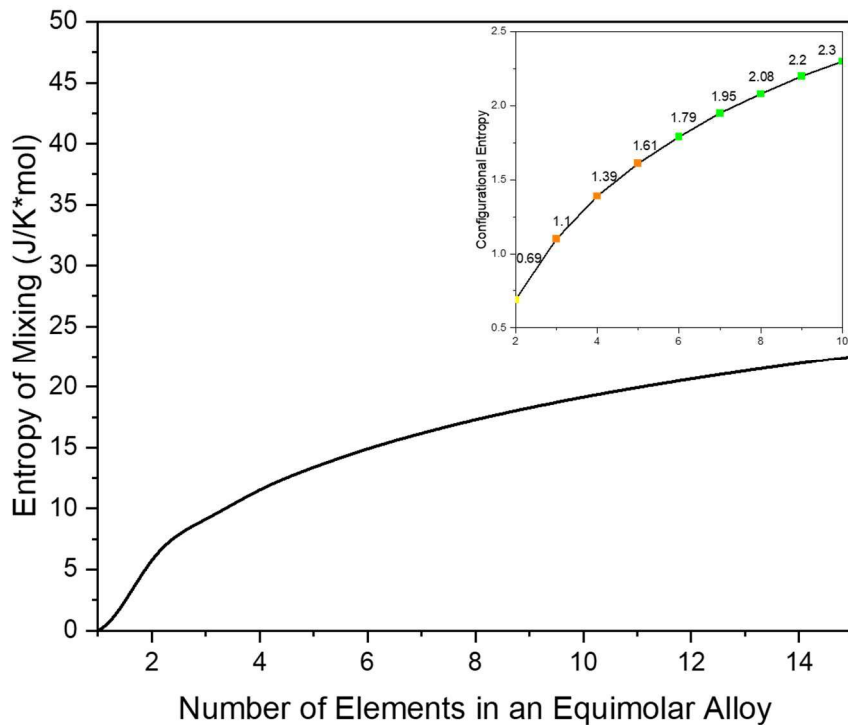


Figure 1:The entropy of mixing based on the number of elements in an equimolar alloy.

Because there are many different combinations of alloys that can exist following both the composition and entropy-based definitions, some researchers have combined the two definitions to narrow the scope of alloys that can be classified as a high entropy alloy. There have also been

interpretations that an HEA must be a single-phase solid solution, which has been a primary motivation for HEAs as they are preferable over intermetallic phase formation.

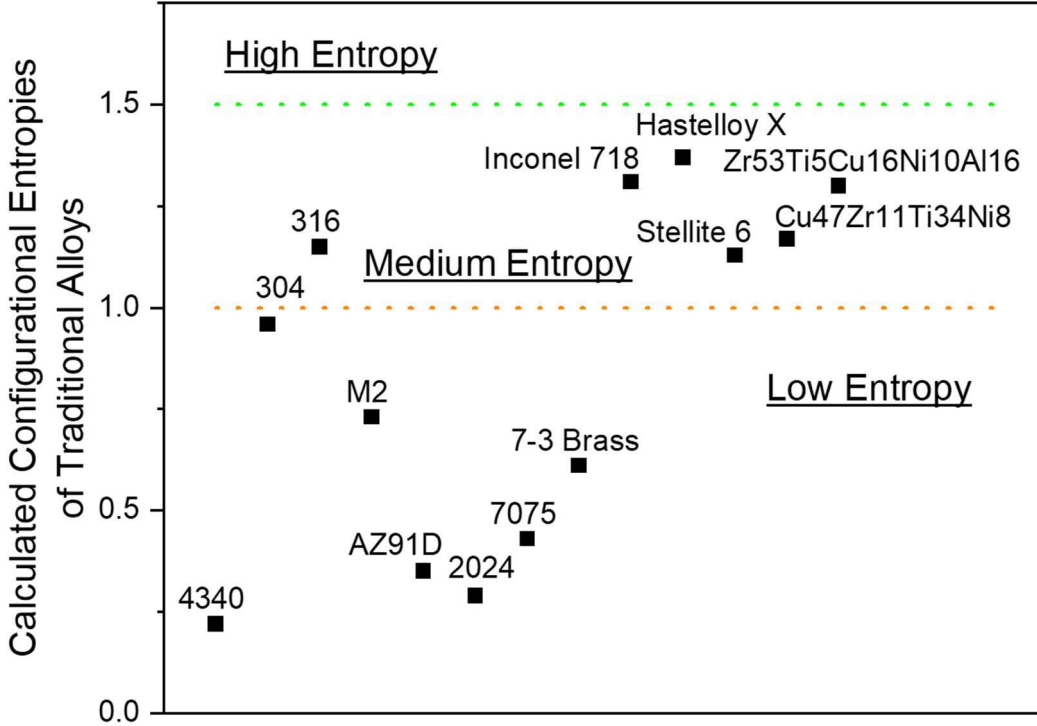


Figure 2: Calculated Configurational Entropies of Traditional Alloys of data obtained from [18].

### 1.3 Core Effects of High Entropy Alloys

The basis of materials design is the relationship between the structure, processing, performance, and properties of a material. Several factors may affect this relationship during the design of an alloy to obtain the desired outcome. Figure 3 illustrates the correlation between these factors. It is evident that the structure of a material is related to the composition used and results in a microstructure that may be affected by the processing technique used to manufacture such alloy. This resulting microstructure can affect the properties exhibited by the material which all play into the performance. This understanding of a core physical metallurgy principle can

help to improve materials. In high entropy alloys, there are four main effects that are considered to play a role in the enhanced properties.

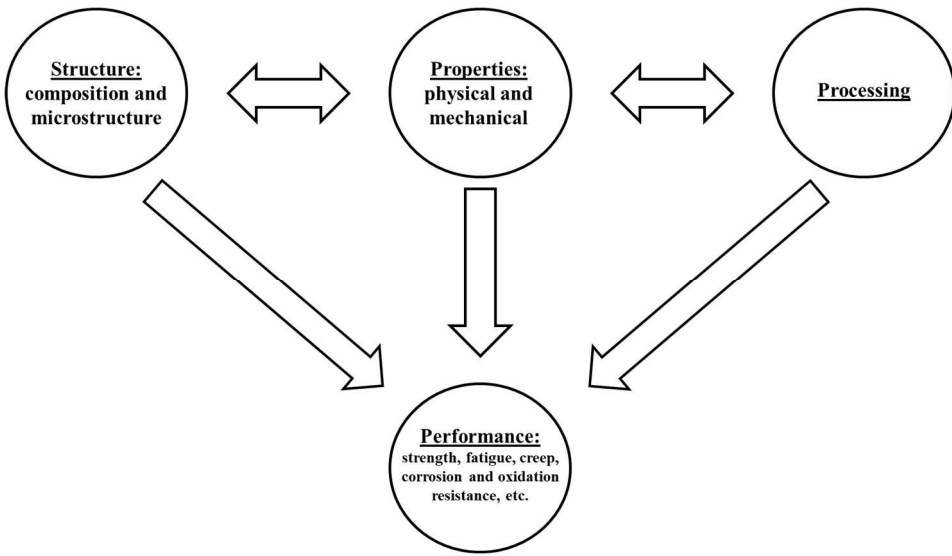


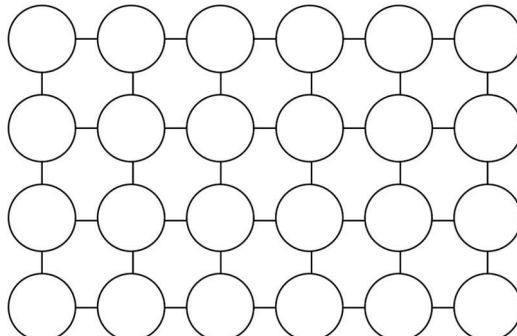
Figure 3: A schematic representation of the relationship between the structure, properties, processing, and performance of materials.

### 1.3.1 High Entropy Effect

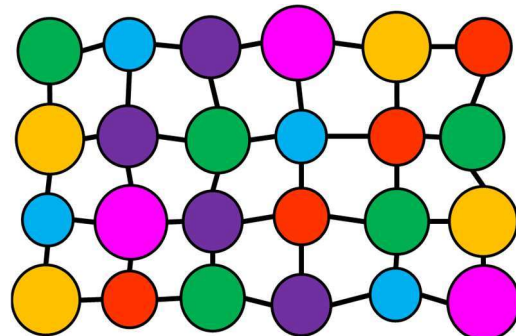
The high entropy effect stems from the coined name, thus an increased configurational entropy with five or more elements may favor solid-solution phases over competing for intermetallic or intermediate phases [16]. If a single-phase solid solution is formed in an alloy, this would make for a much simpler microstructure than what may be expected. The formation of such solid solution phases is believed to be promoted by the high entropy, particularly at high temperatures [19]. The resulting microstructure may otherwise exhibit a more complex structure including intermetallic compounds that are brittle and difficult to understand. For this reason, the formation of intermetallic compounds often tries to be avoided.

### 1.3.2 Lattice Distortion Effect

When evaluating HEAs structurally, there exists a size difference amongst the different atoms that randomly occupy lattice sites in a matrix. Because of such atomic size differences, there is a certain degree of lattice distortion caused. This lattice distortion is uncertain in various positions and is said to contribute to the excess configurational entropy, thus adding to the overall total configurational entropy of a system [16]. Lattice distortion has been shown to have a positive effect on the material properties, including an increase in hardness and strength, x-ray diffraction peak intensity reduction, and a reduction in the electrical and thermal conductivities [19]. These properties have also been shown to be relatively insensitive to temperature. A schematic representation of lattice distortion in a matrix containing different atoms in random lattice sites is demonstrated in Figure 4. It is evident that a matrix of single atoms results in a perfect lattice while an HEA matrix results in a distorted lattice. The entire solute matrix of an HEA will produce a lattice in which every atom in the lattice site has a different first neighboring atom and therefore suffer a certain degree of distortion.



(a) matrix of one single element resulting in a perfect lattice



(b) matrix of multiple elements resulting in a distorted lattice

Figure 4: Comparison of a perfect lattice and a distorted lattice.

### ***1.3.3 Sluggish Diffusion Effect***

Sluggish diffusion of atoms has also been proposed in HEAs as it may lower the diffusion rate of atoms and therefore, phase transformations in the matrix [19]. For phase transformation to occur, a cooperative diffusion of different atoms is necessary. If the rate of diffusion of atoms is reduced, the overall transformation rate of alloys is reduced. It has been noted that the slowest diffusing elements will often determine the transformation rate. The variation of atoms in occupied lattice sites causes an irregular diffusion of vacancies or atoms. Though experimental observations are limited because of the difficult nature of experiments, sluggish diffusion has been observed in a CoCrFeMnNi HEA in which it was observed that substitutional diffusion was difficult and higher activation energies were required [20]. A mechanism for sluggish diffusion was proposed: atoms along a diffusion path experience large fluctuations in lattice potential energy causing a large diffusion barrier due to the variation of atoms along a diffusion path.

### ***1.3.4 “Cocktail” Effect***

The last of the four main core effects are termed the “cocktail” effect. This description is less of a scientific one and more of a descriptive term used to accentuate the pleasure associated with a positive outcome in alloy design. This description was first presented by Ranganathan [21] using the term “multimetallic cocktails”. In his publication, he highlights how alloy design began as an accidental discovery and as research has progressed, unusual combinations have continued to provide ‘super’ properties [21]. The importance of the cocktail effect is that one may obtain exceptional results from unexpected synergies [16] which describes much of the HEA research.

## **1.4 Taxonomy of High Entropy Alloys**

As previously described, according to the varying definitions surrounding high entropy alloy classifications, there exists a vast composition space of alloys. Once an alloy is classified as a high entropy alloy, it can further be described based on the principal constituent elements which make up the alloy. Since the high entropy alloy inception, nearly two decades of research have resulted in a multitude of alloy compositions. Many of these alloys have been comprised of nearly 40 elements, spanning the use of elements included, but not limited to, alkaline earth metals, transition metals, metalloids, and even non-metals in some cases [16]. Based on the elements utilized, such HEAs can be classified into an alloy family. There have been seven alloy families described thus far: 3d transition metals HEAs, refractory metal HEAs, light metal HEAs, lanthanide transition metal HEAs, precious metal HEAs, brass and bronze HEAs, and interstitial compound HEAs [16]. Though there exist HEAs belonging to all seven alloy families, the two which have been the most widely studied are the refractory metal and 3d transition metal families with the latter being the most popular. The focus of this study is on alloys classified as refractory HEAs.

## **1.5 Refractory High Entropy Alloys**

HEAs classified in the refractory alloy family consist of elements that contain at least four refractory elements [16]. These elements include Cr, Hf, Mo, Nb, Ta, Ti, V, W, and Zr. Refractory metals are those classified based on their high melting temperature. Various definitions exist defining the exact melt temperature of these metals, but it may generally be stated as any temperature higher than iron ( $1535^{\circ}\text{C}$ ) [22]. These metals are a group of transition metals whose interatomic bonding possesses high strength, allowing them to have a high melting point,

mechanical strength, and electrical resistance. For this reason, they are commonly known as being heat-resistant materials [22i].

As previously stated, this alloy family has not been studied as in-depth as those in the 3d transition family, though has gained popularity in recent years for its potential to be used in high-temperature applications. The utilization of refractory elements into high entropy alloys was first developed by Senkov et al. in 2010 [23]. At that time, high entropy alloy research had focused on the use of late transition metals (Co, Cu, Fe, Ni, etc.) and there had been no exploration about using refractory elements. HEAs designed using refractory elements were called refractory high entropy alloys (RHEAs). The main objective was to create a metallic alloy for high-temperature, load-bearing structures, and thermal protection [24].

### ***1.5.1 Basic Properties of Common Refractory Elements***

Understanding the role each element can play in an alloy during design requires the knowledge of the basic properties inherent to each constituent element. Refractory elements are classified because of their high melting temperatures, making them desirable for high-temperature applications. Table 1 outlines the key properties of each element utilized in this study including the melting point, density, lattice parameter, Young's modulus, and coefficient of thermal expansion (CTE), all of which are important aspects that may affect an alloy's behavior. The elements outlined all have melting points above 1800<sup>0</sup>C, ranging from 1875-3380<sup>0</sup>C. They also have a wide range of density values, with V having the lowest at 6.1 g/cm<sup>3</sup> to W, which has a very high density of 19.3 g/cm<sup>3</sup>. The differences in the lattice parameter will give rise to the lattice distortion that will be experienced in the matrix, especially with the inclusion of Cr, which has a small lattice parameter of 2.885 Å relative to the other elements included. The Young's modulus and coefficient of thermal expansion (CTE) variation also indicate that the mixture of these metals

results in different properties. Evaluating the differences in the elemental properties play a role in the alloy design. For example, it is possible to create a high-strength material with the inclusion of W or Mo, but this will result in a high-density material. If the opposite is desired, i.e., a low-density material, then V can be used but will result in a sacrifice in strength. By evaluating and understanding the properties innate to each element, the role which they play in the resultant alloy properties can be further identified.

Table 1: Basic properties of the six refractory metals used in this work. Data obtained from [22].

Element	Melting Point (°C)	Density (g/cm³)	Lattice Parameter (Å)	Young's Modulus (GPa)	Coefficient of Thermal Expansion (10⁻⁶ per °C)
Cr	1875	7.19	2.885	279	8.4
Mo	2610	10.28	3.147	329	4.9
Nb	2468	8.57	3.301	105	7.1
Ta	3000	16.6	3.303	186	6.5
V	1919	6.1	3.024	128	8.3
W	3380	19.3	3.165	390	4.6

### 1.5.2 Oxidation Data of Refractory Metals

Since oxidation is a primary aspect of this work, identifying the potential oxides which may form and the point at which they may form is also important. Table 2 outlines some of the notable oxides that form because of each constituent element. Note that this table only outlines binary oxides, however high entropy alloys have the potential to form several complex oxides that may be difficult to identify and characterize.

Table 2: Oxide formation energies of common oxides of constituent elements used in this work.  
Data obtained from [25].

Oxide	Remarks	Structure	Heat of Formation (H <sub>298</sub> , kJ/kmole)	Melting Point (°C)	Color
Cr <sub>2</sub> O <sub>3</sub>		Trigonal	1142.0	2334 ± 25	Green (dark)
MoO <sub>2</sub>	Oxidizes to MoO <sub>3</sub>	Monoclinic	548.5	1927	Dark Brown
MoO <sub>3</sub>		Rhombohedral	755.0	801 ± 2	Green/Yellow
NbO <sub>2</sub>	Oxidizes to Nb <sub>2</sub> O <sub>5</sub> upon heating	Tetragonal	797.0	2080 ± 20	Blue/Black
Nb <sub>2</sub> O <sub>5</sub>		Varies	1905.0	1490 ± 20	White/Grey/Black
Ta <sub>2</sub> O <sub>5</sub>	α and β phase exist	Rhombohedral	2047.0	1785 ± 30	White
VO		Cubic	410.0	1830 ± 20	Grey/Black
V <sub>2</sub> O <sub>3</sub>	Oxidizes to V <sub>2</sub> O <sub>5</sub> upon heating	Trigonal	1239.0	1970 ± 20	Black
V <sub>2</sub> O <sub>5</sub>		Rhombohedral	1560.0	670-685	Red/Yellow/Orange/Brown
V <sub>3</sub> O <sub>5</sub>		Monoclinic		1827	
WO <sub>2</sub>	Oxidizes to WO <sub>3</sub>	Monoclinic	573.6	1570	Brown
WO <sub>3</sub>		Tetragonal	840.9	1470-2130	Yellow/Green/Blue

### 1.5.3 Hume-Rothery Rules for Refractory Metals

One major aspect of high entropy alloys is that they may preferentially form solid solutions over intermetallic or intermediate phases. Because of this, it is imperative to confirm that the constituent elements used in high entropy alloys can form solid solutions. To confirm this, the Hume-Rothery rules for solid solutions can be applied. The Hume-Rothery Rules are as follows:

- 1      Similar atomic radii (less than 15% difference)
- 2      Similar electronegativity
- 3      Similar crystal structure
- 4      Similar valence

The six elements used in this work were all compared and evaluated to see if they met such rules. Table 3 outlines the binary groups of elements. All sets of elements in binary combination meet the requirements of the Hume-Rothery rules and show they can form solid solutions.

Table 3: Crystal structure, atomic radius, electronegativity, and valence of each constituent elements and the binary combinations to abide the Hume-Rothery rules. Data obtained from [22].

	Crystal Structure	Atomic Radius	Electronegativity	Valence
Cr	BCC	129	1.56	6
Mo	BCC	140	1.30	6
Nb	BCC	147	1.23	5
Ta	BCC	147	1.33	5
V	BCC	135	1.45	5
W	BCC	141	1.40	6
Cr-Mo	Same	<b>9%</b>	<b>17%</b>	Similar
Cr-Nb	Same	<b>14%</b>	<b>21%</b>	Similar
Cr-Ta	Same	<b>14%</b>	<b>15%</b>	Similar
Cr-V	Same	<b>5%</b>	<b>7%</b>	Similar
Cr-W	Same	<b>9%</b>	<b>10%</b>	Similar
Mo-Nb	Same	<b>5%</b>	<b>5%</b>	Similar
Mo-Ta	Same	<b>5%</b>	<b>2%</b>	Similar
Mo-V	Same	<b>4%</b>	<b>12%</b>	Similar
Mo-W	Same	<b>1%</b>	<b>8%</b>	Similar
Nb-Ta	Same	<b>0%</b>	<b>8%</b>	Similar
Nb-V	Same	<b>8%</b>	<b>18%</b>	Similar
Nb-W	Same	<b>4%</b>	<b>14%</b>	Similar
Ta-V	Same	<b>8%</b>	<b>9%</b>	Similar
Ta-W	Same	<b>4%</b>	<b>5%</b>	Similar
V-W	Same	<b>4%</b>	<b>3%</b>	Similar

#### 1.5.4 Potential Applications for Refractory High Entropy Alloys

The interest in HEAs has focused largely on the superior mechanical properties they may obtain. The extensive options leave the possibility for several different industries and applications which may include, extreme temperature environments, catalytic applications, chemical environments, defense applications [26]. The alloy class of RHEAs display great potential for the

extreme temperature environments because of their functional and structural properties. The main objective behind the development of RHEAs has been to create a structural class of materials that could withstand such extreme, high-temperature environments. Refractory metals are commonly used in alloys for high temperature or extreme environment applications, including within the aerospace, nuclear, and chemical industries. They are also commonly used in corrosive environments. Potential commercial applications of these types include land-based gas turbines, heat exchanger tubing in the chemical process industry, nuclear reactors, and various components in the aerospace industry including propulsion systems [24]. In addition to high-temperature applications, RHEAs may also be useful in applications currently using conventional refractory metals and alloys or superalloys.

Much of the research has focused on surpassing the properties of the commercial alloys and superalloys, such as nickel-based, iron-based, titanium based, and cobalt-based alloys. Such alloys used in commercial applications require a combination of high-temperature strength (including tensile, fatigue, and creep) and environmental tolerance (including oxidation, corrosion, and wear). One example of such applications includes gas turbine blades and vanes which operate at temperatures up to  $1000^{\circ}\text{C}$  [24].

Aerospace applications present an especially difficult environmental challenges because of the changes in temperatures and pressures which the components may experience. The material design must also be conscious of the weight and density of the material to reduce fuel consumption, operating costs, and pollution and must select components due to their lightweight features [27]. The authors in [27] provide an in-depth review of HEAs, including RHEAs and other families, that have potential for aerospace applications.

Another avenue that has been explored for RHEAs has been as nuclear energy components, for example in fusion reactors. Nuclear reactors pose particularly severe materials environments that include a combination of high temperature and stresses, contact with chemically aggressive coolants, and aggressive radiation fluxes [28]. The promise and expansion of nuclear power worldwide has created a demand for materials to be used in such applications. Two HEAs focused on vanadium were studied that were believed to be favorable for nuclear fusion applications [29]. Two alloys of V-Cr-Mn and V-Cr-Mn-Ti were examined because of the low activation elements chosen. The alloys formed a single BCC phase, which is beneficial for fusion applications. The group of alloys showed good promise for further development and use of HEAs in nuclear fusion applications. Other studies of RHEAs have shown great promise which also targeted nuclear applications as the intended use [30-32].

Some less common applications explored for RHEAs have been WC-based matrix body drill bits [33] and use in medical applications [34], both of which showed great possibility in its respective application.

### ***1.5.5 Mechanical Properties of Refractory High Entropy Alloys***

The interest in high entropy alloys has grown largely in the past two decades because of the promise of superior mechanical properties. In both 3D transition metals and refractory high entropy alloys, encouraging experimental results have been obtained, however, the focus of this work will be placed on refractory high-entropy alloys. Two refractory HEAs marked the start of these propitious results: a quaternary WN<sub>x</sub>TaMo alloy and a quintenary WN<sub>x</sub>MoTaV alloy [23]. Both alloys were the first of their kind to be studied in equiatomic amounts containing all refractory alloys. The alloys both maintained a BCC structure and had some indications of a disordered solid solution. The quaternary alloy obtained an average microhardness value of H<sub>V</sub> =

4455 MPa and the quintenary alloys had an average microhardness of  $H_V = 5250$  MPa, both of which are significantly higher than that of pure elements [23]. The increased hardness of the quintenary alloy was attributed to the addition of V, which has a smaller atomic radius and therefore introduced lattice strains into the matrix, a core effect of HEAs. The addition of V was also believed to have had a solid solution-like strengthening mechanism, as there was no significant difference in grain size.

The exciting results of the quaternary and quintenary alloys boosted further evaluation of these alloys at elevated temperatures. The same alloy compositions, a quaternary WN<sub>x</sub>TaMo alloy, and a quintenary WN<sub>x</sub>MoTaV alloy were investigated from room temperature up to 1600<sup>0</sup>C to identify the ductile-to-brittle transition temperature (DBTT) and the temperature dependence on the yield strength [35]. For deformation at room temperature, the alloys exhibited a yield strength of 1058 MPa and 1246 MPa respectively. The fracture mode indicates that the ductile-brittle transition temperature (DBTT) for the alloys are above room temperature. Across the 600-1000<sup>0</sup>C temperature range, both alloys displayed good plastic flow and only saw a slight decrease in yield strength within this range. At a temperature of 1600<sup>0</sup>C, the quaternary alloy yield strength decreased to a value of 405 MPa while the quintenary alloy had a comparable yield strength of 477 MPa. Both alloys were able to maintain a dendritic microstructure up to 1400<sup>0</sup>C. Though the decrease in yield strength from room temperature to 1600<sup>0</sup>C may appear large, when compared to two commercially used superalloys, both alloys show competitive, and even superior, strength values, especially at elevated temperatures. At temperatures below 800<sup>0</sup>C, the quintenary alloy has commensurable values to Inconel 718. Above 1000<sup>0</sup>C both alloys exhibit far greater strength values and indicate they would be suitable candidates in high temperature commercial applications [35].

Additional studies based around the MoNbTaW and MoNbTaVW alloys began after the two articles published by the Senkov group. A similar MoNbTaV quaternary alloy was studied at room temperature and was able to obtain results exceeding that of the MoNbTaW quaternary alloy. The MoNbTaV alloy had a maximum yield stress of 1.5 GPa [36], compared to the ~1 GPa obtained by the MoNbTaW alloy. Though the yield stress was higher, the microhardness values were comparable, obtaining a value of  $H_v = 4947$  MPa compared to the  $H_v = 4455$  MPa in the MoNbTaW alloy. Similar studies continued to expand on the two alloys. A set of  $Ti_xNbMoTaW$  ( $x=0, 0.25, 0.5, 0.75, 1$ ) refractory high entropy alloys were evaluated [37]. The yield strength value of 996 MPa for the composition containing no Ti content (MoNbTaW) was comparable with that of the Senkov study [23] at room temperature. The addition of Ti increased the yield strength, and as the Ti amount increased, the yield strength correspondingly increased. For the composition  $Ti_1NbMoTaW$ , the yield strength reached a high of 1455 MPa [37]. The strengthening was attributed to a solid solution hardening effect and indicates that alloying can effectively be done to improve the strength and ductility of such RHEAs.

Since the induction of RHEAs by the Senkov group in 2010 [23], several studies have been conducted to evaluate the mechanical properties of this alloy family both at room temperature and elevated temperatures. Studies including the five main refractory elements originally used by Senkov (Mo, Nb, Ta, V, and W) have varied the amounts of alloying additions and processing techniques, many showing promising results [38-43]. As further studies have been done, there have been several reviews that have now been published to compile and compare the encouraging results of many of the RHEAs [24,44,45].

### **1.5.6 Oxidation of Refractory High Entropy Alloys**

Refractory elements have commonly been disregarded in terms of oxidation resistance due to their poor performance in elemental form. For instance, above 800<sup>0</sup>C Mo forms gaseous oxides known to evaporate quickly [46]. V is easily oxidized, forming V<sub>2</sub>O<sub>5</sub>, which has a low melting point of 690<sup>0</sup>C [47]. W is also capable of forming an easily evaporated oxide, WO<sub>3</sub> at 1150<sup>0</sup>C [48]. While some other refractory elements, such as Nb, may not form oxides that easily evaporate or volatize, they have a high solubility of oxygen [49]. While many refractory elements do not form protective oxides scales, one of importance does: Cr. Cr is known to form a protective oxide scale, chromia (Cr<sub>2</sub>O<sub>3</sub>). For this reason, it has been used in several commercial alloys, including stainless steels and Ni-based superalloys. The inclusion of Cr into several refractory high entropy alloys has proven beneficial. For example, an AlSiTiCrNbMoTa RHEA was deemed oxidation resistant, forming a protective CrTaO<sub>4</sub> oxide scale [50]. In addition to adding elements beneficial for oxidation resistance, the high concentrations of constituent elements are believed to slow the diffusion of oxygen [44], relating back to one of the core effects of HEAs: sluggish diffusion.

Oxidation studies on these RHEAs have shown that despite large amounts of refractory elements present, they can still exhibit acceptable, if not good, oxidation resistance. A MoWAlCrTi RHEA showed a surprisingly good oxidation resistance after 40 hours of exposure at 1000<sup>0</sup>C [51]. The alloy followed a parabolic rate law which indicated that the oxide scale growth progressed through solid state diffusion. A similar NbMoCrTiAl RHEA was also evaluated with and without Si addition [52]. The RHEA without Si addition showed only a moderate mass gain during oxidation in air at temperatures of 900 and 1000<sup>0</sup>C, following a linear rate law. The addition of 1 at. % of Si moderately improved the oxidation resistance, but still followed a linear rate law, indicating that selective alloying in low amounts may be beneficial for enhancing oxidation

resistance. Similarly, the specific use of Nb was found to enhance oxidation resistance during cyclic oxidation in a NbTiHfCrGeSi multiphase alloy by promoting the formation of the protective oxide CrNbO<sub>4</sub> and hampering the formation of other complex oxides, such as Ti<sub>2</sub>Nb<sub>10</sub>O<sub>29</sub> [53].

Various studies have been conducted on the oxidation behavior of RHEAs to improve alloy compositions given their strong potential to retain superior mechanical properties at high temperatures. Oxidation studies conducted include assessing the oxidation performance and different elevated temperatures and hold times [54, 55], optimization of oxidation resistance techniques, i.e., pack cementation [56], effect of constituent elements, and alloy composition [57], and oxidation mechanisms [58]. Though various processes have been investigated, all studies maintain the same goal of mitigating base material degradation through the formation of a barrier against the oxidizing environment [59].

### ***1.5.7 Annealing of Refractory High Entropy Alloys***

An avenue not commonly explored as often as other aspects are the annealing and heat treatments of high entropy alloys. Annealing can be done to homogenize or recrystallize a material or even assess the thermal stability of a material. A few studies on high entropy alloys highlight this. For example, a CrNbTaVW RHEA was subjected to a 6 hour anneal at 600, 700, and 800°C [60]. The annealing treatment did not cause any significant modifications to the microstructure and the retention of the structure shows evidence of sluggish diffusion, a key element of high entropy alloys. Similarly, a WTaMoNbTi exhibited a high phase stability in the temperature range from room temperature to 2000°C [61]. The RHEA consisted of a single BCC structure of dendritic grains which grew into equiaxed grains at 1600°C. This alloy also indicated a strong resistance to softening because of dynamic recrystallization. Various other studies have been done on different RHEAs to further investigate the phase transformations and stability of microstructures [62-64].

Knowledge of phase transformations at elevated temperatures is of key importance to the high temperature behavior of these materials, as the microstructure is directly related to the material properties. The sparse studies about the annealing of high entropy alloys leaves a vast potential of work to be done in this area and proves to be an emerging aspect of research to assess the thermal stability. Further investigation into this aspect of high entropy alloys may also reveal more details and mechanisms of sluggish diffusion and provide further evidence of this fundamental characteristic.

## **1.6 Atomistic Simulations and Plastic Deformation Behavior of High Entropy Alloys**

Machine learning has demonstrated to be an advantageous and reliable route for further understanding novel materials, including high entropy alloys. This method has proven to be notably helpful at the atomic and nano level. Due to the difficulty and time-consuming nature of experiments used to investigate atomic-level mechanisms, machine learning simulations provide a relatively efficient and easy way to gain knowledge about a material's behavior at such a level and evaluate several alloy compositions at one congruent time.

Atomistic calculations can provide insight into various alloy compositions and help predict the materials behavior, including the plastic deformation behavior. Studies on the plastic deformation behavior of HEAs have exhibited exciting results that coincide with many experiment results [65-70]. To understand the plastic deformation behavior of a material, the knowledge of the dislocation movement through the metal is required [71]. In body-centered cubic (BCC) crystals, dislocation glide can occur on various planes under different conditions and will usually occur on the maximum resolved shear stress planes [72]. The Peierls stress is a measure related to the dislocation glide in a pure metal, which is the resolved shear stress required to move a dislocation over at least one lattice site [73]. In HEA systems, the complement of the Peierls stress

is the local slip resistance (LSR) [74]. In a CoCrFeNiMn alloy and its subsystems, the slip resistances calculated by a Peierls-Nabarro model were much larger than those in typical FCC pure metals [75]. This indicated that the high yield strength of the alloys could be a direct result of the increased slip resistance. Various atomistic simulations have been performed to understand the plastic deformation behavior of both face-centered cubic (FCC) and BCC MPEAs, many of which were discussed by [76] and [77]. Recent experimental studies on the plastic deformation behavior of MPEAs are in good agreement with atomistic simulation studies. The yield stresses of Al<sub>1.2</sub>CrFeCoNi micropillars were shown to be insensitive to temperature changes, differing from pure metals and dilute alloys [78]. The observed temperature insensitivity was attributed to the dynamic recrystallization involving dislocation tangles and the formation of dislocation cell structures. Further expansion of the effect of MPEA micropillars used a mixture of molecular dynamics simulations and transmission electron microscopy (TEM) characterization to shed light on deformation mechanisms in these alloys. The simulations and TEM observations both revealed that size effects on yield/flow stress and strain hardening were the result of dislocation mechanisms [79]. This indicates that simulations may be a good starting point prior to experiments and indicates the importance that dislocations can have.

For the dislocation motion to occur, bonds must be broken and formed across the crystalline glide planes, which can be compared to shearing two halves of a crystal across a plane[80]. The energy required to shear the plane is the generalized stacking fault energy (GSFE) [81, 82]. The GSFE has been used as a baseline measure for designing MPEAs of various chemical compositions [83]. The addition of small amounts of Co ( $0.25 \leq x \leq 2$ ) to AlCo<sub>x</sub>CrFeNi was found to enhance the ductility and strength based on the evaluation of GSFE curves, as well as to provide insight into the surface energy values of different slip planes. GSFE calculations are useful for studying

the effect of different element concentrations and compositions and how they affect the plastic deformation behavior [84].

In addition to dislocations, metallic alloys often contain other material defects such as voids and precipitates. Defects such as these may be expected to enhance the strengthening of a material by acting as an obstacle to dislocation motion. Atomistic simulation studies have found interesting results on the mechanisms related to dislocation motion and their interactions with barriers to dislocation motion in both FCC and BCC metals [85-87]. The results indicate that obstacles present in a matrix may be a beneficial contribution but has yet to be largely explored in HEAs and other multi-principal element alloys. The lack of research surrounding these alloys leaves an emerging avenue to explore given the promise in pure metals.

## **Chapter Two: Research Problem**

### **2.1 Introduction**

High entropy alloys (HEAs) were first introduced as a formal alloying concept in 2004 by Yeh et al. [1] and Cantor et al. [2]. Since its inception, the materials research community has taken an active role in investigating the potential these alloys have in commercial applications. Nearly two decades of research have led to different HEA alloy families, each with different intended applications. One of such alloy families which have emerged and show exciting promise is refractory high entropy alloys (RHEAs). Senkov et al. [23] first proposed using refractory metals as constituent elements in HEAs because of their high melting points and high-temperature application potential. The two studied RHEAs consisted of equiatomic WNbMoTa and WNbMoTaV, both of which showed excellent mechanical strength, even at elevated temperatures. These results prompted the promise this class of materials and embolden the research community to begin focus on these materials. Because of the ample combination of elements that can be utilized in high entropy alloys, several studies have been done on various alloy compositions. Though many have revolved around the original W-Nb-Mo-Ta alloy, there are still several avenues which can be explored to create an optimal material for high temperature and extreme environment applications.

### **2.2 Statement of the Problem**

The scope of this work is to study the high-temperature behavior of two refractory high entropy alloys to be used in extreme environments. The goal is to investigate the high-temperature properties and characteristics of a CrNbTaVW and CrMoNbTaW alloy. Work on the CrNbTaVW alloy was a continuation of previous work that was already completed, and work done on the CrMoNbTaW was compared to evaluate which of the two would be most compatible in extreme

environments applications. The CrNbTaVW was found to be oxidation resistant up to 800<sup>0</sup>C, so the oxidation layer surface and the interface between the metal and oxide layer was further investigated to identify the type of oxides forming and which constituent elements play a role in the oxidation behavior. The CrMoNbTaW exchanged Mo for V because of the volatility and poor oxidation resistance of V. It is also possible for V to form intermetallic Laves phases which is often not desired so the swap for Mo eliminates this possibility, as Mo does not form an intermetallic Laves phase. The high-temperature studies include oxidation studies to evaluate the oxidation resistance and annealing studies to assess the thermal stability of the alloy. These results will be compared with atomistic simulations performed at room temperature to further assess the plastic deformation behavior and relate that to the strength of the material.

### **2.3 Significance of the Study**

The vast space of compositions which exist within the definition of high entropy provides thousands of potential alloys. Insight and information into various alloy compositions provides the HEA community with more data to further evaluate potential candidates for use in commercial applications. The variation of studies included in this research provides a good overall assessment to decide if these alloy compositions have potential in commercial applications. The work to be done on the CrNbTaVW RHEA continues to work of [55] and [60] where the alloy was determined to have a good oxidation resistance at temperatures up to 800<sup>0</sup>C for three days in air, however, could not withstand temperatures in the range of 1000<sup>0</sup>C-1400<sup>0</sup>C. The alloy was also found to be thermally stable up to 800<sup>0</sup>C after no microstructural changes were seen after annealing for 6 hours. There have been no other studies found in literature which examine this alloy composition. The second alloy composition, CrMoNbTaW, has only been identified once in literature in [56]. The HEA was fabricated via powder milling and then pack cemented to observe the beneficial effects

of pack cementation. The characteristics of the base alloy was not studied in depth, therefore making the experiments performed in this work novel to the research community.

## **2.4 Research Objectives**

The specific research objectives of this work are outlined as follows:

1. Investigate two novel refractory high entropy alloys.
2. Evaluate the interface between the metal and oxide layer in the CrNbTaVW alloy to understand the surface oxide layer and identify predominant oxides and understand the role which the constituent elements may play in the oxidation behavior.
3. Characterize the as-received CrMoNbTaW alloy and investigate the high temperature properties.
4. Perform atomistic simulations at room temperature to understand the plastic deformation behavior and relate this to the strength characteristics of this alloy family.

## Chapter Three: Experimental Procedures

### 3.1 Fabrication of the Alloys

The CrNbTaVW and CrMoNbTaW alloys were procured from Plasmaterials in Livermore, California. Both alloys were processed through vacuum arc melting in equiatomic proportion using pure metals of at least 99.9% purity. Each sample was cut by electric discharge machining into 5x5x5 mm cubes. The specific alloy compositions are outlined in Table 4.

Table 4: Specific alloy compositions of two RHEAs.

Alloy	Composition (% atomic)					
	Cr	Mo	Ta	Nb	V	W
CrNbTaVW	20	0	20	20	20	20
CrMoNbTaW	20	20	20	20	0	20

### 3.2 Characterization of the As-Received Alloys

The alloys were examined in the as-received condition. The microstructure was examined by optical microscopy (OM), scanning electron microscopy (SEM), and energy dispersive x-ray spectroscopy (EDS). The phases and structure of the alloys were identified by x-ray diffraction (XRD). XRD analysis was performed on an unmounted sample. Prior to the examination, the sample was cleaned in an ultrasonic cleaner for 2 minutes in ethanol. The sample was then mounted in a hydraulic mounting press. After mounting, the sample was polished using standard metallographic techniques to 800 grit.

### 3.3 Oxidation Experiments

The samples to be oxidized were approximately 5x5x5 mm cubes. Each sample was ultrasonically cleaned for 2 minutes in ethanol and weighed three times and then averaged from

the as-received condition before exposure to lab air in its respective oxidation temperature and time (600, 800, 1000, 1100, 1200, 1300, 1400°C; 12 or 24 hours). Samples were heated and cooled at a rate of 10°/min. Each sample was placed in the center of a covered alumina crucible and placed directly below the thermocouple within the furnace. The same furnace was used for each oxidation experiment. The experiments were performed in a SentroTech ST Muffle Box furnace. The mass gain per unit area (mg/cm<sup>3</sup>) as a function of time and temperature is used to determine the oxidation resistance of each alloy.

### **3.4 Oxidized Sample Characterization**

The oxidized samples were weighed after removal from the furnace after cooling to room temperature and recorded. Each sample was weighed three times and averaged amongst the measurements. The oxidation products were characterized by SEM, EDS, and XRD. The parameters and characteristics of the equipment used for analysis are outlined in Table 5. The surface morphology was observed using SEM and EDS.

### **3.5 Annealing Experiments**

The samples to be annealed were approximately 5x5x5 mm cubes. Each sample was ultrasonically cleaned from the as-received condition for 2 minutes in ethanol prior to exposure to lab air in its respective temperature (600, 700, 800°C) for 6 hours. Samples were heated and cooled at a rate of 10°/min. Each sample was placed in the center of a covered alumina crucible placed directly below the thermocouple within the furnace. The same furnace was used for each oxidation experiment. The experiments were performed in a Sentro Tech ST Muffle Box furnace. After annealing, each sample was mounted in a hydraulic mounting press. After mounting the samples were prepared using standard metallographic techniques to 800 grit.

### 3.6 Annealed Sample Characterization

The annealed samples were mounted in a hydraulic mounting press and then polished following standard metallographic procedures to 800 grit. The microstructure was analyzed through SEM and EDS analysis. The structure and phases were examined by XRD. The equipment parameters and details are outlined in Table 5.

Table 5: Equipment information and operating parameters.

Equipment	Parameters/Operating Conditions
Optical Microscopy	Olympus GX53
SEM/EDS Hitachi SU 3500	Accelerating Voltage: 30 KV Probe Current: 90-120 $\mu$ A Working Distance: 8-12 mm
SEM/EDS Hitachi SU-4800 Scanning electron microscope equipped with energy dispersive spectrometer	Accelerating Voltage: 25 KV Probe Current: 8-12 mm Working Distance: 8-12 mm
X-Ray Diffraction Bruker D8 Discover X-Ray Diffractometer	Radiation: Cu-K $\alpha$ ( $\lambda=1.54 \text{ \AA}$ ) Step: 0.02 $^{\circ}$ Time/Step: 0.5 sec No. of Steps/Scan: 3084
Microhardness	Duramin A300
Analytical Balance	Sartorius Analytical Balance Model MC210S
Pace Technologies Terapress TP-7500 Hydraulic Mounting Press	Heating Temperature: 200 $^{\circ}$ F Heating Pressure: 30 Pa Heating Time: 8 minutes

## **Chapter Four: Experimental Results and Discussion**

Two RHEAs were evaluated to investigate their high-temperature behavior and evaluate if they may be suitable for extreme environments. A CrNbTaVW alloy in equiatomic proportions was first evaluated and found to have adequate oxidation resistance up to 800<sup>0</sup>C in previous studies reported in literature [45i]. V was believed to be a detrimental factor for the oxidation resistance, for which it was exchanged with Mo in the second alloy. The hope is that the exchange of Mo would offer better oxidation resistance and provide some increased strength. The second alloy evaluated is an equiatomic CrMoNbTaW alloy. The findings from both alloys are presented here.

### **4.1 CrNbTaVW Alloy**

The results of experimental studies on the as fabricated and annealed equiatomic CrNbTaVW microstructures were published and reported in [60]. The alloy exhibited a multiphase microstructure consisting of five different phases. The phases listed below will be referenced in subsequent sections.

- Phase One: Round and bright white, W-rich phase containing trace elements of Cr and V
- Phase Two: Dark gray, cloudy, V-rich phase containing moderate amounts (10-18%) of Cr, Ta, Nb, and small amounts of W
- Phase Three: Grainy, Cr-rich structure containing a mixture of Ta-Cr solid solution and Laves phase
- Phase Four: Light gray, cloudy, Nb-rich phase containing moderate amounts (10-18%) of Cr, Ta, V, and small amounts of W
- Phase Five: Laves phase (VTa<sub>2</sub>) identified as dark black areas

After annealing for 6 hours at 600, 700, and 800<sup>0</sup>C, the microstructure did not exhibit any significant changes, retaining a multiphase microstructure. In the examined temperature range, there was no evidence of phase transformation and therefore considered to be thermally stable.

The alloy was further examined for its oxidation resistance and reported in [55]. The metal loss was considered reasonable and therefore has adequate oxidation resistance up to 1000<sup>0</sup>C for three days in air. Above temperatures of 1000<sup>0</sup>C, the alloy was not able to withstand oxidation products formed. Two main oxides were identified: one of a cylindrical shape consisting of Ta and W and one of a granular or nodular shape of Nb and Cr. At 1200<sup>0</sup>C, the presence of V appeared on the surface of the oxide scale [55]. Based on the promising results of the alloy reported in [55], the interface of the metal and oxide layer was investigated along with the surface oxide layer.

#### ***4.1.1 X-Ray Diffraction***

The XRD data presented in Figure 5 below had not yet been reported. The five metals used are all BCC metals and as indicated in the XRD, the alloy retains a BCC structure. Three main peaks at 39<sup>0</sup>, 58<sup>0</sup>, and 73<sup>0</sup> align to a BCC structure. The smaller peaks present are identified as Ta peaks. The lattice parameter is calculated as 3.1759 Å from the XRD scan.

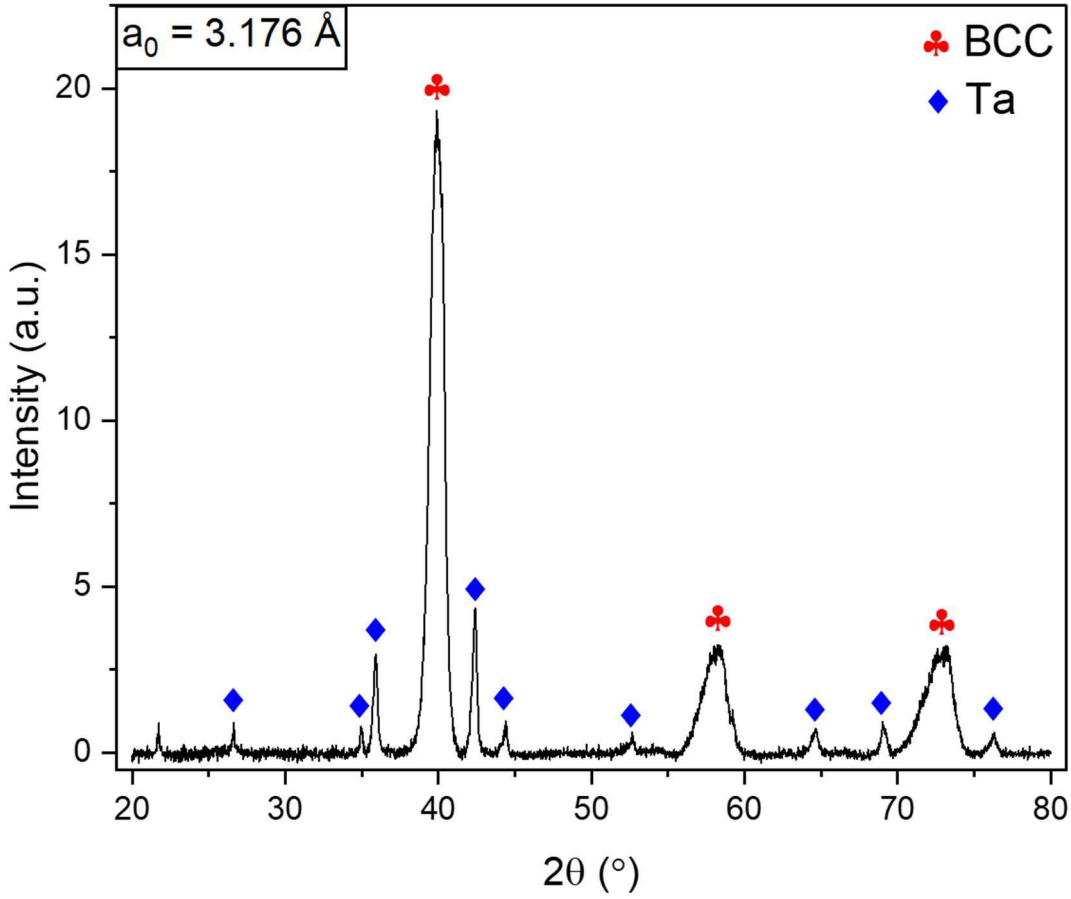


Figure 5: XRD data of the as-fabricated CrNbTaVW alloy produced by vacuum arc melting.

#### ***4.1.2 Oxidation of a CrNbTaVW HEA***

The promising results obtained reported in [55] up to  $800^\circ\text{C}$  led to further exploration of the interface and surface characteristics of the oxide scale. The substrate-oxide layer interface was observed at  $700$  and  $800^\circ\text{C}$  after 24 hours of oxidation in air. To evaluate the morphology and composition of the oxide scale, the surface was investigated at  $700$  and  $800^\circ\text{C}$  after 48 hours of oxidation in air.

#### **4.1.2.1 Cross-Sectional Substrate-Oxide Interface**

The composition and microstructure of the alloy was near nominal following the findings originally reported in [60]. The microstructure present below the oxide layer of the oxidized sample is presented in Figure 6. EDS spot analysis was performed in various locations to estimate the composition in different areas. The bulk microstructure consisting of five phases of the oxidized sample matches that of the as received sample reported in [60] and is considered as a basis for this work. Medium gray areas noted as B and D in the figure are visible near the interface. These are the previously identified phase 3 that consists of a Cr-rich structure with a mixture of a Ta-Cr solid solution and a Laves phase. There is significant cracking within the phases, especially in area B. An area marked as E shows some presence of O, but is Ta-rich. The remaining four elements contain similar amounts ranging from 12.9-18.9%. A darker grey area is visible next to location D. This dark grey area is suspected to be a Ta-rich oxide indicated by the EDS analysis. The large, dark pore near the bottom left-hand corner of the image is similar in shape and morphology of a  $\text{VO}_x$  pore which was identified in an  $\text{NbCrMoTiVAl0.5}$  alloy.[36] The  $\text{VO}_x$  pores identified in the  $\text{NbCrMoTiVAl0.5}$  alloy were found to have most likely formed because of fusion or volatilization of a  $\text{V}_2\text{O}_5$  oxide. A low melting point of  $\text{V}_2\text{O}_5$  at  $670^\circ\text{C}$  is likely to have been a contributing factor to this. [37] The authors suspect that the large pore identified near the interface in Figure 6 may be of similar formation.

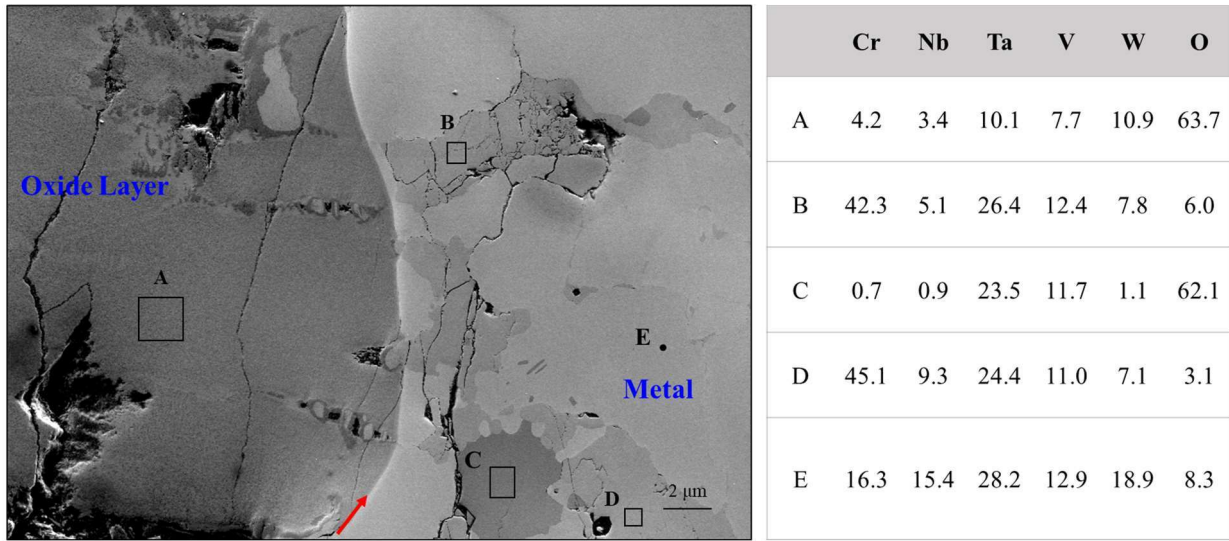


Figure 6: Oxide-layer substrate interface of the sample oxidized for 24 hours at 700<sup>0</sup>C. EDS spot analysis is included for reference.

Figure 7 confirms the presence of the five phases previously identified within the substrate [60]. The areas believed to be these phases are noted in Figure 7 by its respective phase number. Both Ta and Cr elements appear to stay in solution in the substrate and do have a strong presence in the oxide layer, which is evident in the EDS elemental mapping. Cracking and voids are present at the interface boundary which grow upward into the oxide layer and is indicated in Figure 7. Nb and W are the two main elements that appear most in the oxide layer. There is no significant constituent element within the oxide layer. A Nb-rich mixed oxide was found just above the interface at locations A and B, while a W-rich oxide was found in the center of the oxide layer in the area marked C and D where Cr, V, and Ta were present in similar amounts in both the oxides. V-rich areas are visible in the substrate near the interface as indicated by the color maps. Voids and significant cracking at the boundary layer that grows outwards into the oxide layer are visible.

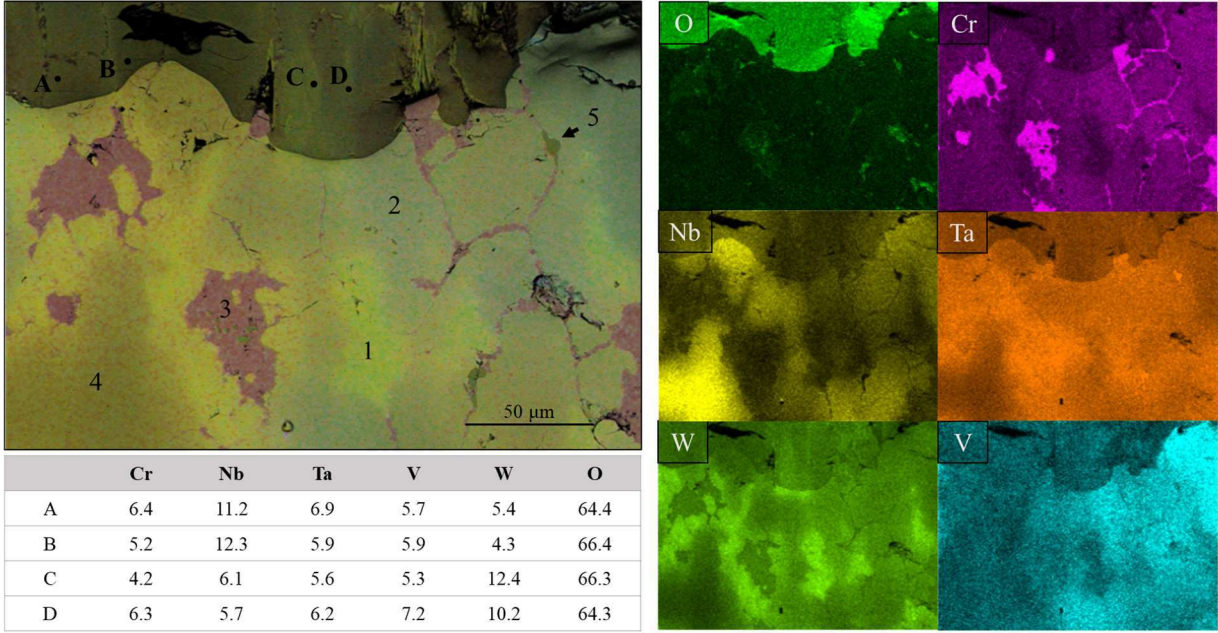


Figure 7: Color mapping of the oxide-layer substrate interface of the sample oxidized for 24 hours at 700°C. EDS spot analysis is included for reference.

Figure 8 illustrates the nonuniformity of the oxide layer, which appears as a thick, porous layer. The pores are suspected to be associated with the presence of W and Ta in the oxide layer in areas near each other because of the difference in coefficient of thermal expansion (CTE). [88, 89]. A large difference in CTE can cause one oxide product may cool faster, which in this case is W, and causes a difference in contraction leaving a void space. This also contributes to significant internal stresses seen within the oxide scale. In this case, W has a CTE of approximately  $4.8 \times 10^{-6}$ , while Ta has a CTE of approximately  $6.7 \times 10^{-6}$ . Tungsten appears vertically in the oxide layer, indicating an upward directional growth of the oxide layer. This is visible through the EDS elemental mapping where strings of W appear throughout the layer. Ta clusters around neighboring regions of W in the oxide layer. Clusters of a W-Ta oxide appear above the surface layer and within some of the large pores, which are highlighted in the mapping. Nb, Cr, and V appear to remain in solution in the substrate, except for Cr, which appears in small amounts throughout the oxide layer.

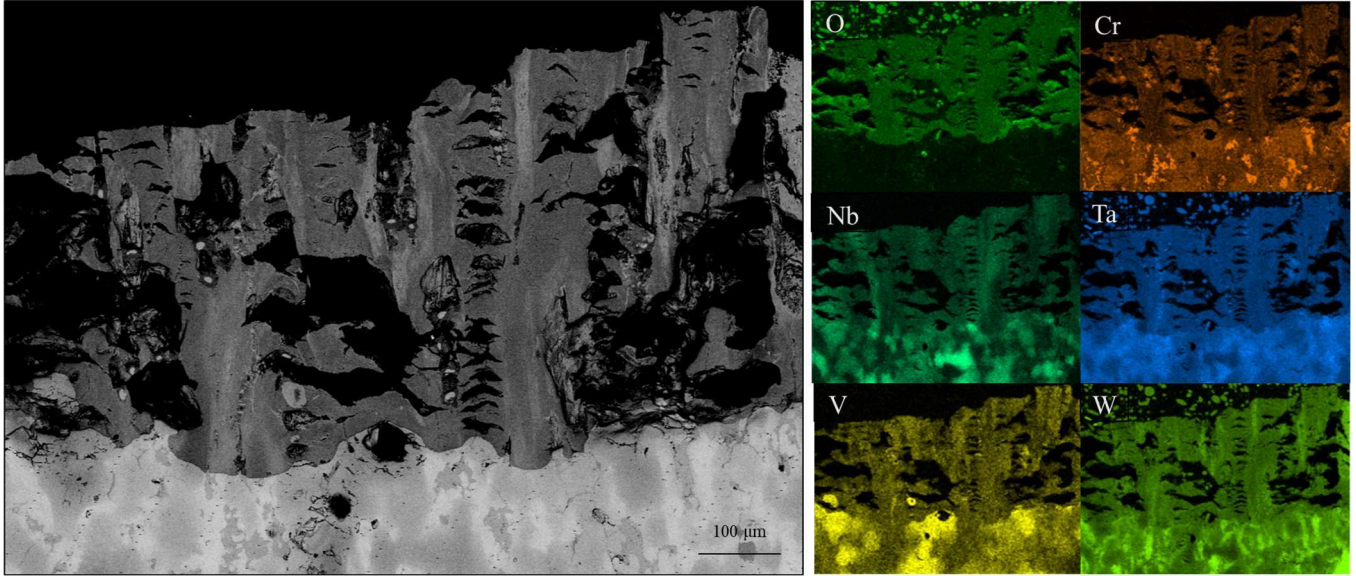


Figure 8: Interface of the sample oxidized for 24 hours at  $700^{\circ}\text{C}$ .

The cross-section of the interface of the oxidized sample at  $800^{\circ}\text{C}$  for 24h is shown in Figure 9. A significant amount of porosity and separation crack appears at the interface, like what was seen at  $700^{\circ}\text{C}$ , possibly due to the occurrence of spallation. The porosity is once again believed to be a result of a V-oxide that melted or the difference in CTE between Ta and W. No single element appears to predominate in the oxide layer, though there are areas of a Cr-rich and W-rich oxide dispersed throughout. Figure 10 shows a similar oxide layer to that at  $700^{\circ}\text{C}$ , which is non-uniform and porous in nature. V appears in small clusters, closer to the interface area and center of the oxide layer. There is no V that appears at the surface of the oxide layer. W again shows a linear, directional upward growth from the interface dispersed throughout the oxide layer. Cr appears in clusters spread relatively evenly throughout the oxide layer. Nb and Ta do not appear heavily throughout the oxide layer, however, Ta remains in the substrate just below the interface.

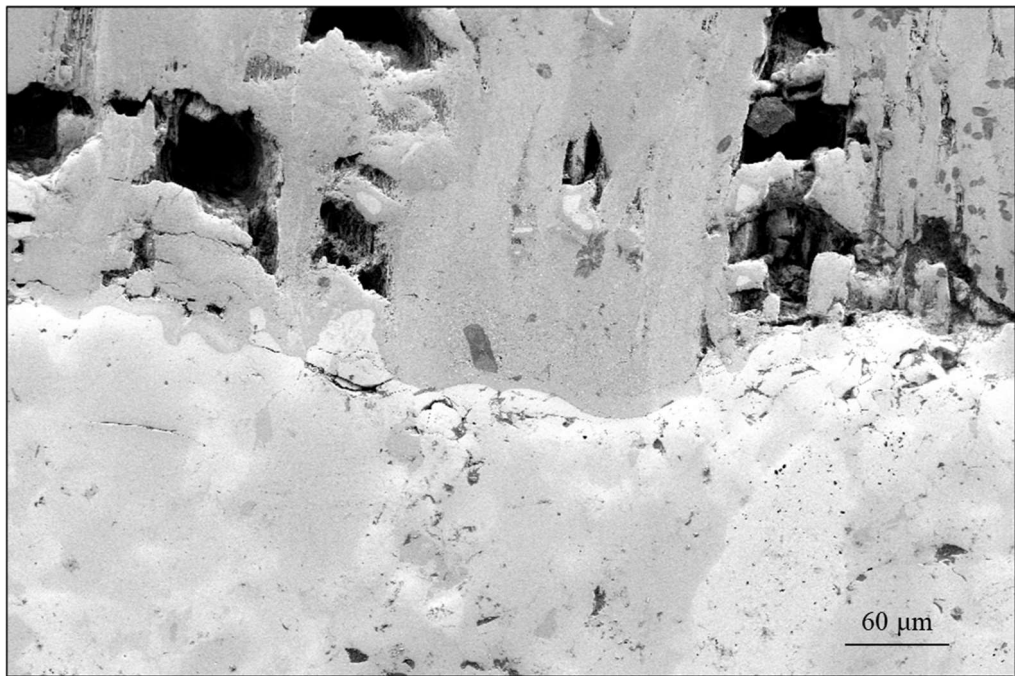


Figure 9: Interface of the substrate-oxide layer of the sample oxidized at  $800^{\circ}\text{C}$  for 24 hours showing severe cracking and porosity at the interface.

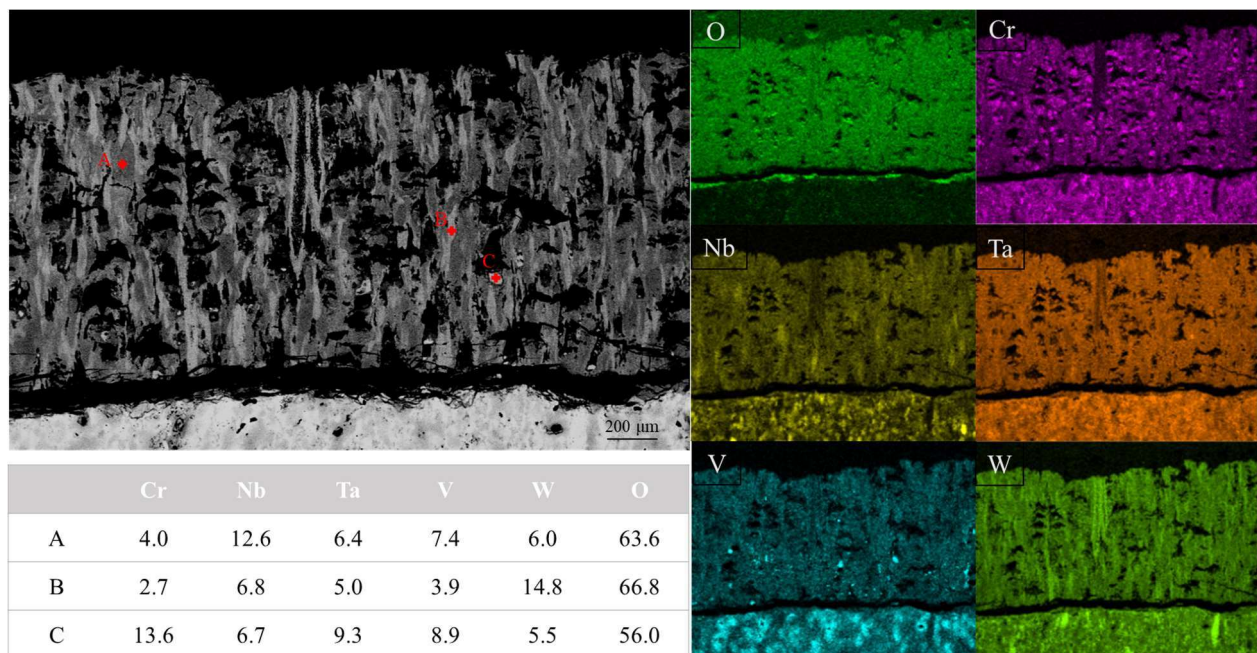


Figure 10: Interface of the substrate-oxide layer of the sample oxidized at  $800^{\circ}\text{C}$  for 24 hours with corresponding EDS color mapping.

Figure 11 indicates the thicknesses of the oxide layer at its respective temperature. The thickness of the 700°C sample ranges from 391.2 µm to 461.1 µm and is found to be a little less than those measured of the alloy CrMoNbTaV, which ranged from 530 µm to 1132 µm, though these measurements were taken at temperatures in the range of 900°C to 1100°C for 25 hours [54]. The thickness of the oxide layer at 800°C is much larger than the 700°C sample, more than doubling in thickness. The thickness of the oxide layer, is relatively even, which was measured ranging from 1.313 mm to 1.379 mm.

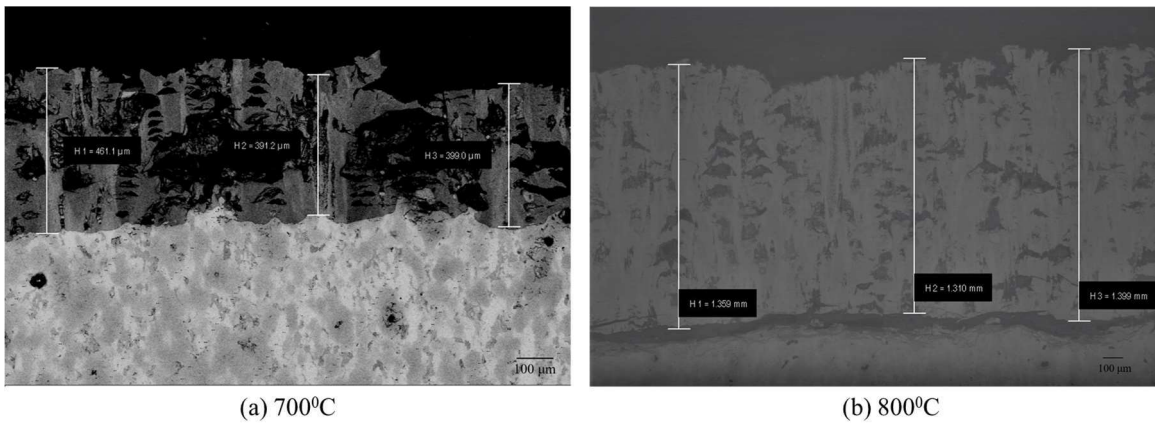


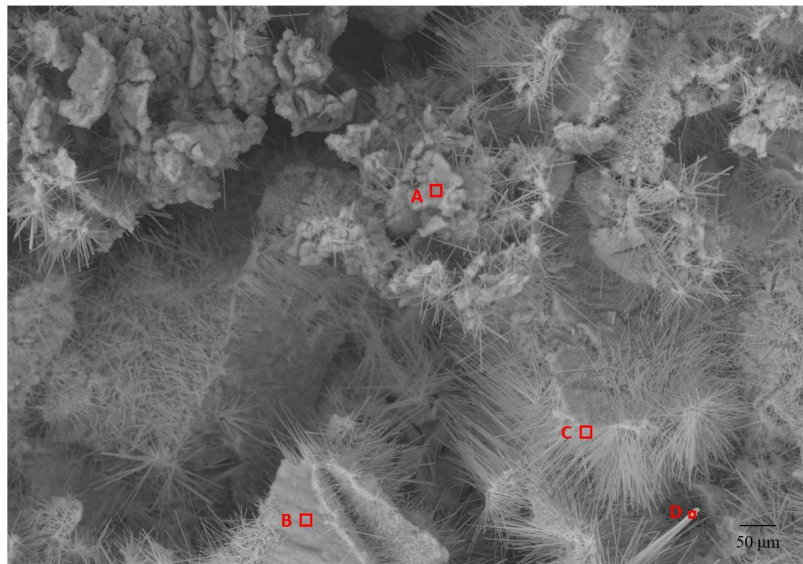
Figure 11: Interface of the substrate-oxide layer indicating the thickness of the sample oxidized at (a) 700°C and (b) 800°C.

#### 4.1.2.2 Surface Analysis

Additional surface analysis of the oxide layers was performed to examine the morphology and chemical composition of oxide scales grown at 700°C and 800°C after 48 hours to compare with the cross-section analysis. At both temperatures, the oxides show a similar physical morphology, however, the oxide layer is denser, containing less porous space, in the 800°C sample.

Figure 12 shows the top surface of the 700°C sample oxidized for 48 hours. Evidently, a very porous oxide, spread throughout the surface can be seen. There are two prominent oxides present, one of a Cr-rich oxide with Ta and Nb present with small amounts of W and V. The Cr-

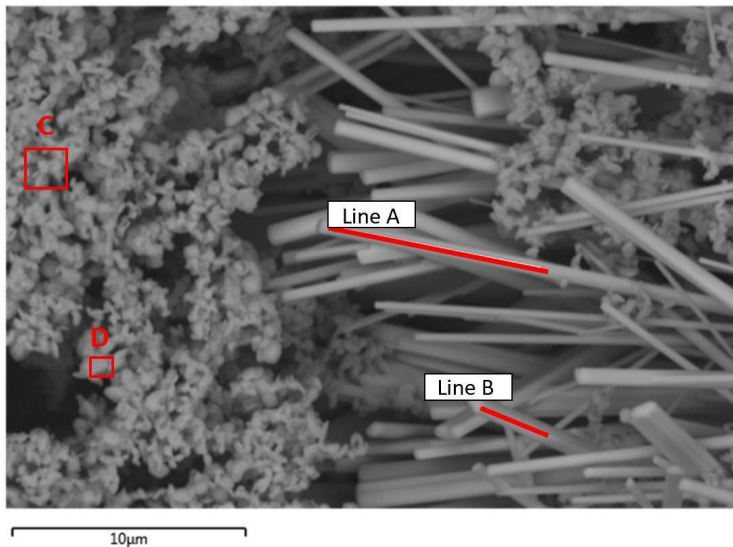
rich oxide has a granular structure. Extending out of the Cr oxides are W-oxide whiskers, which appear to be fine in nature. The W-oxide whiskers are believed to be the other main oxide present, which grow outwards and appear as the lighter structures in the image. This is the most prominent oxide present on the top surface of the oxide layer.



	A	B	C	D
O	49.78	54.05	62.25	53.47
V	4.43	9.01	3.53	4.24
Cr	20.69	11.99	3.83	3.11
Nb	8.06	6.91	5.53	7.55
Ta	12.06	9.69	10.98	12.60
W	4.98	8.35	13.88	19.03
Total	100.0	100.0	100.0	100.0

Figure 102: Surface of the oxide layer at 700°C after 48h in the BSE mode. The two main oxides are visible, the granular Cr oxide containing Ta and Nb with low amounts of V and W present. A whisker-like W oxide growing outwards from the Cr oxide.

The 800°C sample oxidized for 48 hours can be seen in Figure 13. The structure is similar to the 700°C sample; however, the W oxides are more prevalent and have become more defined. The difference in the oxide structure at the surface can be seen in Figure 14. The most prominent oxides present are once again a Cr-oxide and a W-oxide. The W-oxide has grown longer and thicker than what was seen in the previous sample. This is indicative that the oxides grow with an increase in temperature. The granular Cr-oxide is once again present but has become more defined and rounded and has a higher Cr content than at 700°C. Both images utilized EDS to confirm the chemical compositions of the oxides.



	Line A	Line B	C	D
O	70.8	73.8	58.0	54.3
V	2.2	2.5	3.7	5.1
Cr	1.2	0.0	20.0	16.5
Nb	8.0	7.3	6.7	7.4
Ta	5.6	5.8	8.1	8.0
W	12.2	10.6	3.5	8.7
Total	100.0	100.0	100.0	100.0

Figure 13: Surface of the oxide layer of the 800°C after 48h sample in the BSE mode. The granules of the Cr oxide have become more defined and contain a higher content than that seen at 700°C. The W oxide has become thicker and is more prominent.

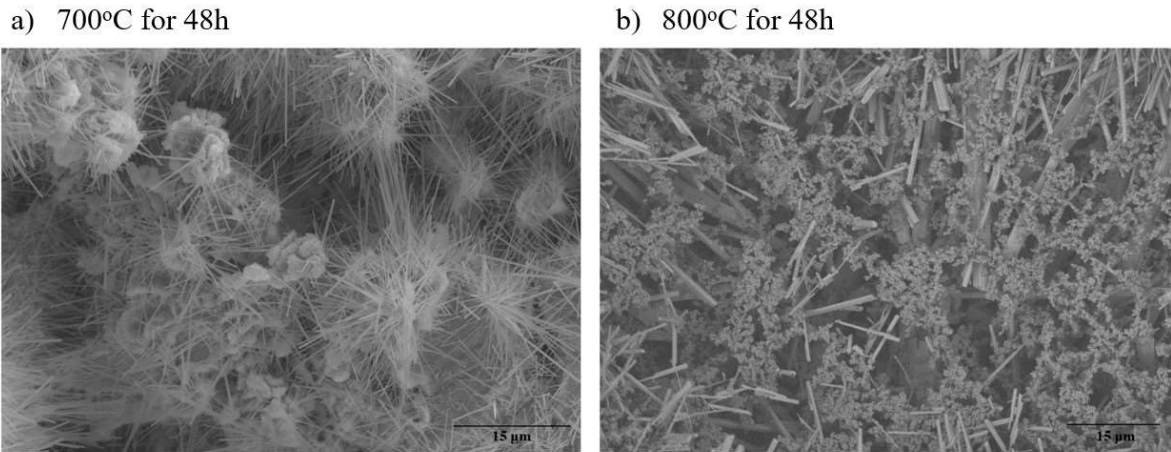


Figure 14: Surface of the oxide layer at a) 700°C for 48h and b) 800°C for 48h. The difference in morphology is visible.

#### 4.1.2.3 Oxide Growth-High Temperature XRD

In-situ high temperature XRD was performed on an unoxidized sample with 100°C increments up to 800°C to understand the oxide growth with increasing temperature. Figure 15 shows the XRD data stacked vertically in terms of varying temperature. At 100°C, there are little

to no indications of oxide growth. The peaks indicate that the structure remains from the as-received state. There are no significant changes in peaks until  $700^{\circ}\text{C}$ , where it is visible that the structure begins to change. The main peaks identified are of metal compounds, except for Cr, which did not appear as a peak for any compounds. This continues as the temperature increases up till  $500^{\circ}\text{C}$ . There are small peaks of different V-oxides, indicating that V is the first element to oxidize. The peaks of V-oxides change from  $\text{V}_7\text{O}_3$  and  $\text{V}_{14}\text{O}_6$  to  $\text{VO}_2$  at  $600^{\circ}\text{C}$ , indicating that more oxygen is introduced into the system at higher temperatures. There is no indication of any proven type of protective oxides previously identified, including  $\text{CrTaO}_4$  and  $\text{Cr}_2\text{O}_3$  [40]. At  $700^{\circ}\text{C}$  peaks of  $\text{NbO}_2$  and  $\text{WO}_3$  appear, for which they are then identified again at  $800^{\circ}\text{C}$ .  $\text{Nb}_2\text{O}_5$  peaks also appear at this temperature, though this was not found in the cross section of the sample. None of the identified oxides suggested by the experimental data is protective, indicating that oxygen can diffuse into the material faster and explains the denser oxide layer at higher temperatures.

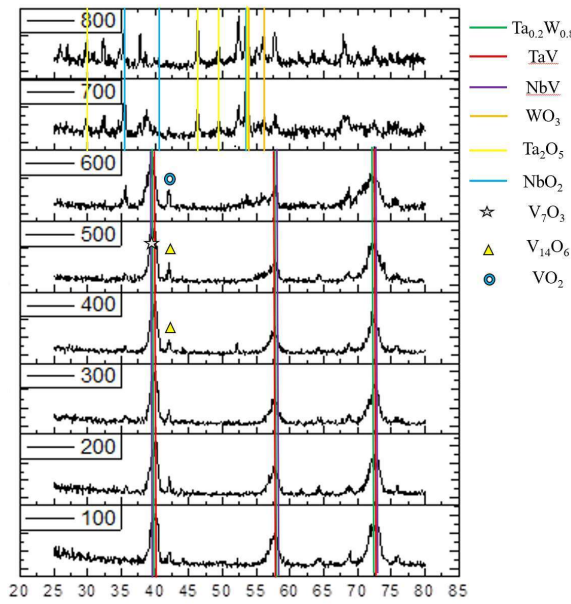


Figure 115: In-situ XRD of the CrNbTaVW HEA.

#### 4.1.2.4 Further Discussion

The SEM and EDS analysis performed in conjunction with the in-situ analysis provided further insight into how this material oxidizes, and the oxide layer forms. The XRD results showed up V oxide peaks forming at lower temperatures; however, this did not appear in the cross-sectional or oxide surface layers. This may potentially be due to the low melting point of some V oxides that create porous structures. Because the sample was only held at temperature for 20 minutes during the in-situ XRD, this most likely did not allow enough time for the oxide to melt and allowed for the detection of the V oxides, but when held for longer periods, the oxide was able to melt and was only detected near the interface, leaving large pores throughout the structure. Tungsten appeared throughout the oxide layer and at the surface at both 700<sup>0</sup>C and 800<sup>0</sup>C, which explains the detection of  $WO_3$ . This is believed to be the elongated, whisker-like oxide found at

the surface and vertically throughout the cross-sectional layer. It is possible that if the samples could oxidize at these temperatures for longer times, the individual oxides may form solid solutions or mixed spinels. Additional XRD measurements must be carried out on the oxides scales to confirm this. These results may shed some light on the effectiveness of the use of refractory metals in the HEA composition for surface and interface oxidation of the alloy. Although the oxidation rates of pure refractory metals, W, Ta, and Nb, are higher at elevated temperatures than those employed in this work, the observed trends, and differences at 700-800°C in these HEAs can be still accountable to their respective oxide formation. Undoubtedly, as evident in SEM and EDS analyses, all the metals in the HEA oxidize and form their respective solid oxides. However, the outward growth of W-oxide, which also is the most prominent oxide present on the top surface of the oxide layer as indicated by the SEM and EDS analyses, may be due to the higher oxidation rate of W compared to Nb and Ta.

## **4.2 CrMoNbTaW Alloy**

### ***4.2.1 As-Received Characterization of the CrMoNbTaW HEA***

#### ***4.2.1.1 SEM/EDS Analysis***

Figure 16 presents the microstructure of the alloy in the as-fabricated condition after vacuum arc melting. The surface is very porous in nature. The EDS analysis confirms the overall composition to be equiatomic of the five constituent elements in the alloy. Unlike many HEAs studied in the literature, this CrMoNbTaW alloy exhibits a multiphase microstructure consisting of three phases. The phases identified here were done by contrast and compositional differences. A large, white phase is identified as a W-rich (43.0 at.%) phase containing slightly depleted amounts of Cr, Nb, and Ta of similar concentrations (14.8-16.4 at.%). Mo is also present in this W-rich phase, however at slightly lower amounts, just above 10 at.%. This phase is highlighted in

the figure. The second phase identified is a Mo-rich (30.2 at.%) containing amounts of Cr, Nb, and Ta in equiatomic amounts (20.2 at.%). This phase is a dark, nearly black area. As a counterpart to the W-rich phase, this phase is W-depleted in comparison to the other constituents, containing only 9.2 at.%. These two counterpart phases are sensible, as the Mo-W phase diagram is isomorphous, so it is reasonable that an area of enriched W would be Mo-depleted and vice versa when the area is Mo-enriched. The third phase is the gray regions surrounding the two previously mentioned phases. This is a matrix that is nearly equiatomic to the five constituent elements and marked as point 3 on the figure. These three phases are highlighted by the color mapping.

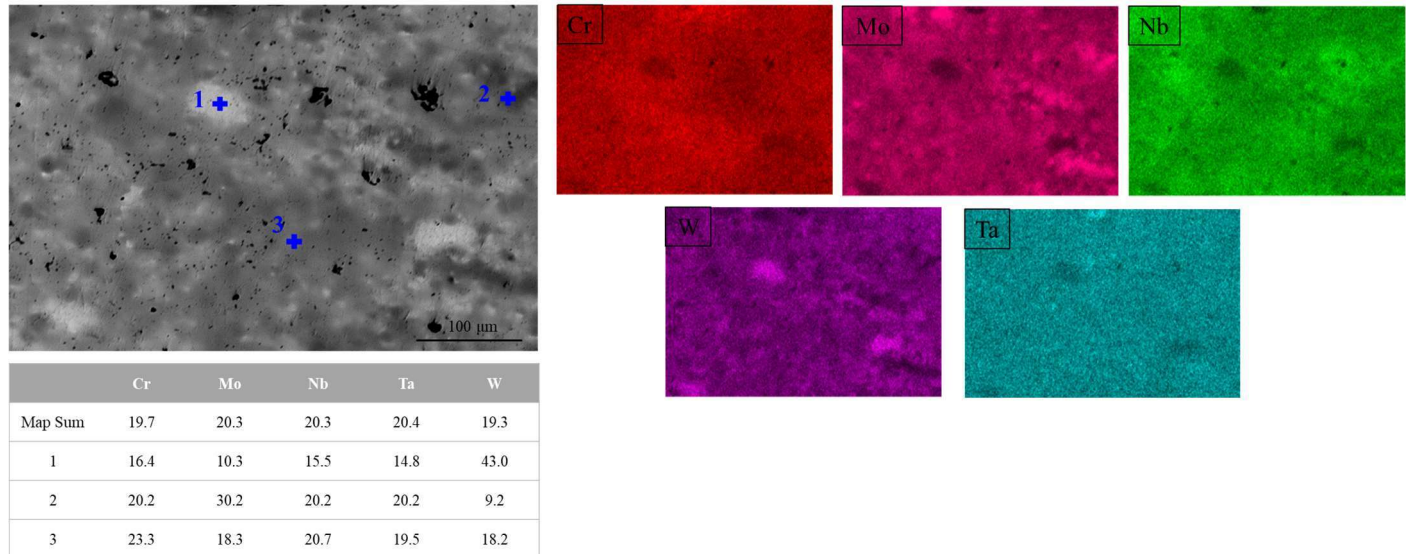


Figure 126: Microstructure of the as-received CrMoNbTaW fabricated by vacuum arc melting.

At increased magnification, grain boundaries can be seen on the sample surface. This is shown in Figure 17. The grain boundaries appear to extend out of pores on the surface. According to the color mapping, the voids and grain boundaries do not appear to contain Mo, Nb, or W. There appear to be two types of void areas, one containing Cr and one containing Ta, highlighted by the color mapping. The grain boundaries appear to be precipitated areas of Cr. The presence of such

grain boundaries was confirmed using optical microscopy which is the corresponding image on the right.

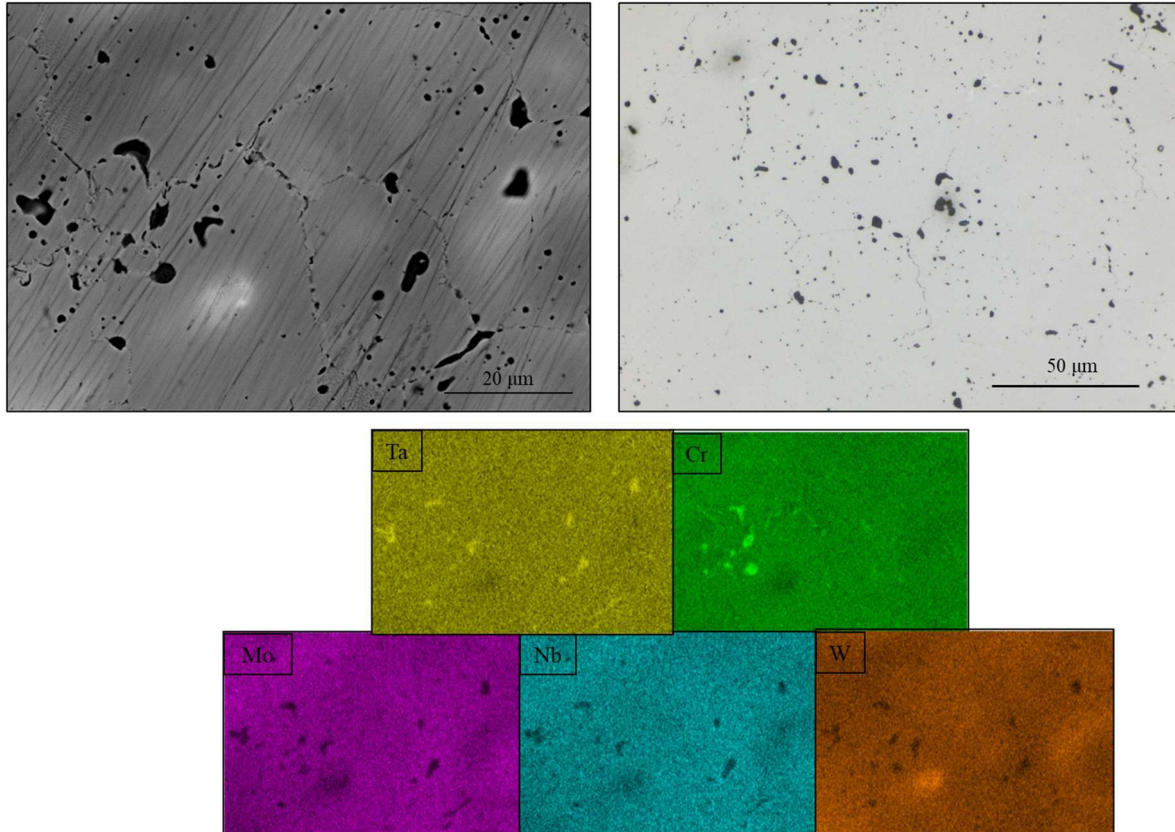


Figure 137: Microstructure of the as-received CrMoNbTaW alloy showing grain boundaries with Cr precipitation.

#### 4.2.1.2 Microhardness

The microhardness was measured in 10 randomly selected locations on the polished surface. Because the difference between the W-rich and Mo-rich phase were not visible through an optical lens, the measured locations were chosen in areas free of voids or precipitated grain boundaries. The tabulated results are presented in Table 6. The average value is  $H_V = 787 \pm 83.6$ . This is higher than the reported quaternary alloy, MoNbTaW alloy obtaining an average  $H_V = 454.3$ .

and a quinary MoNbTaVW alloy which obtained an average  $H_v = 535.3$  [23]. Another alloy of similar composition, though, obtained higher values than the one presented here. A CrMoNbTaV alloy obtained an average  $H_v = 950$  in interdendritic regions and  $H_v = 896$  in dendritic regions [54]. The interdendritic regions was noted as having a higher Cr content than the dendritic regions, citing the increase in hardness. The presence of Cr in the present alloy as compared to the two alloys presented in [23] is believed to have contributed to the increased hardness, as Cr appeared to increase hardness. On the contrary, the addition of V increased the hardness in [23], so it is reasonable to believe that the presence of V in [54] rather than Mo in this study is understandable for the inferior hardness values obtained in the presently studied alloy.

Table 6: Microhardness values of the as-received CrMoNbTaW alloy of the polished sample.

Location	1	2	3	4	5	6	7	8	9	10
$H_v$	628	805	790	851	851	665	827	769	884	843

#### 4.2.2 Annealed Characterization

The alloy was annealed at 600, 700, 800, and  $900^0\text{C}$  for 6 hours to assess the thermal stability of the alloys and identify if any phase changes occurred. Figure 18 presents the microstructures of the samples at their respective annealing temperature. The microstructures of the four annealed samples remain consistent with the identified multiphase microstructure in the as-received condition. There do not appear to be any significant phase changes or coarsening or refinement in the structure as the temperature changes. Figure 19 presents the EDS analysis for each of the annealed samples. The color maps of each of the respective annealing times also highlight the previously identified phases. Overall, the map sum spectrums of each of the EDS analyses show a near equiatomic composition.

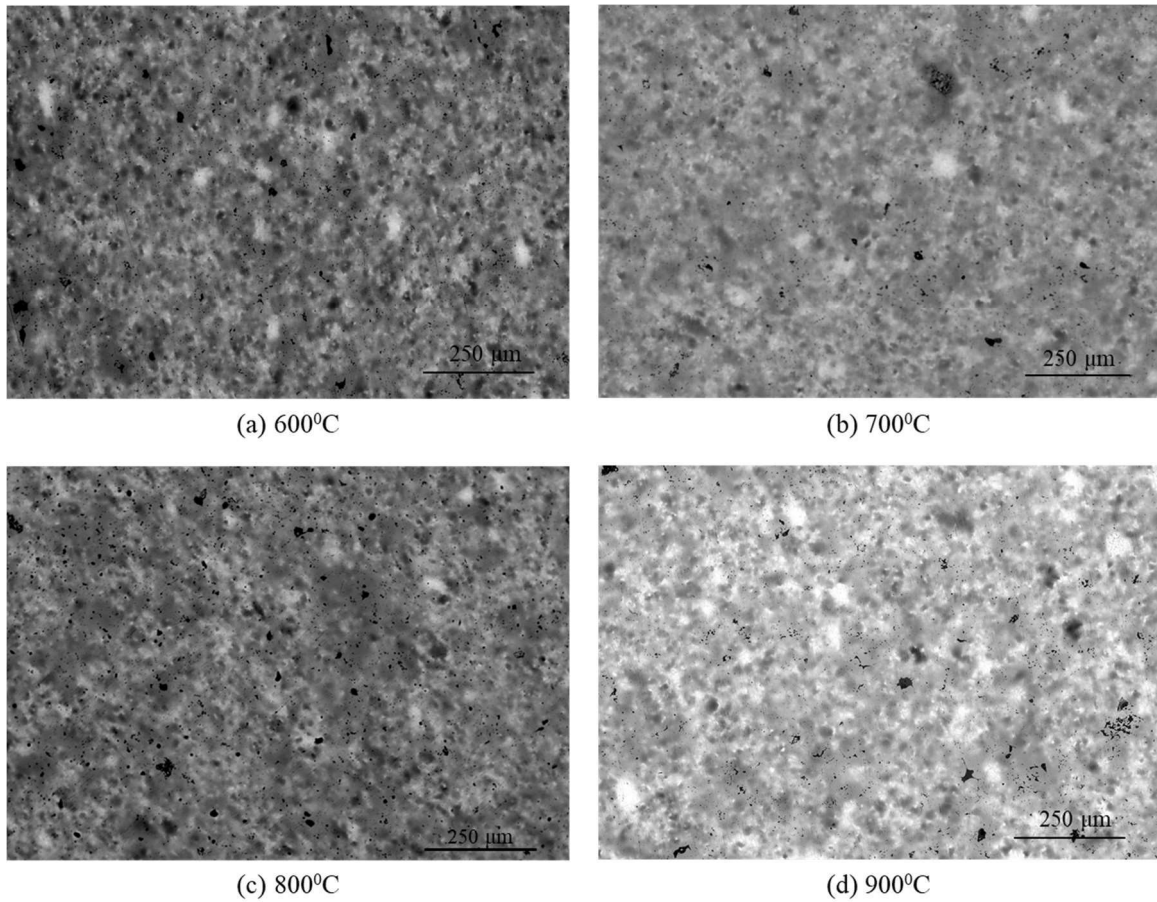
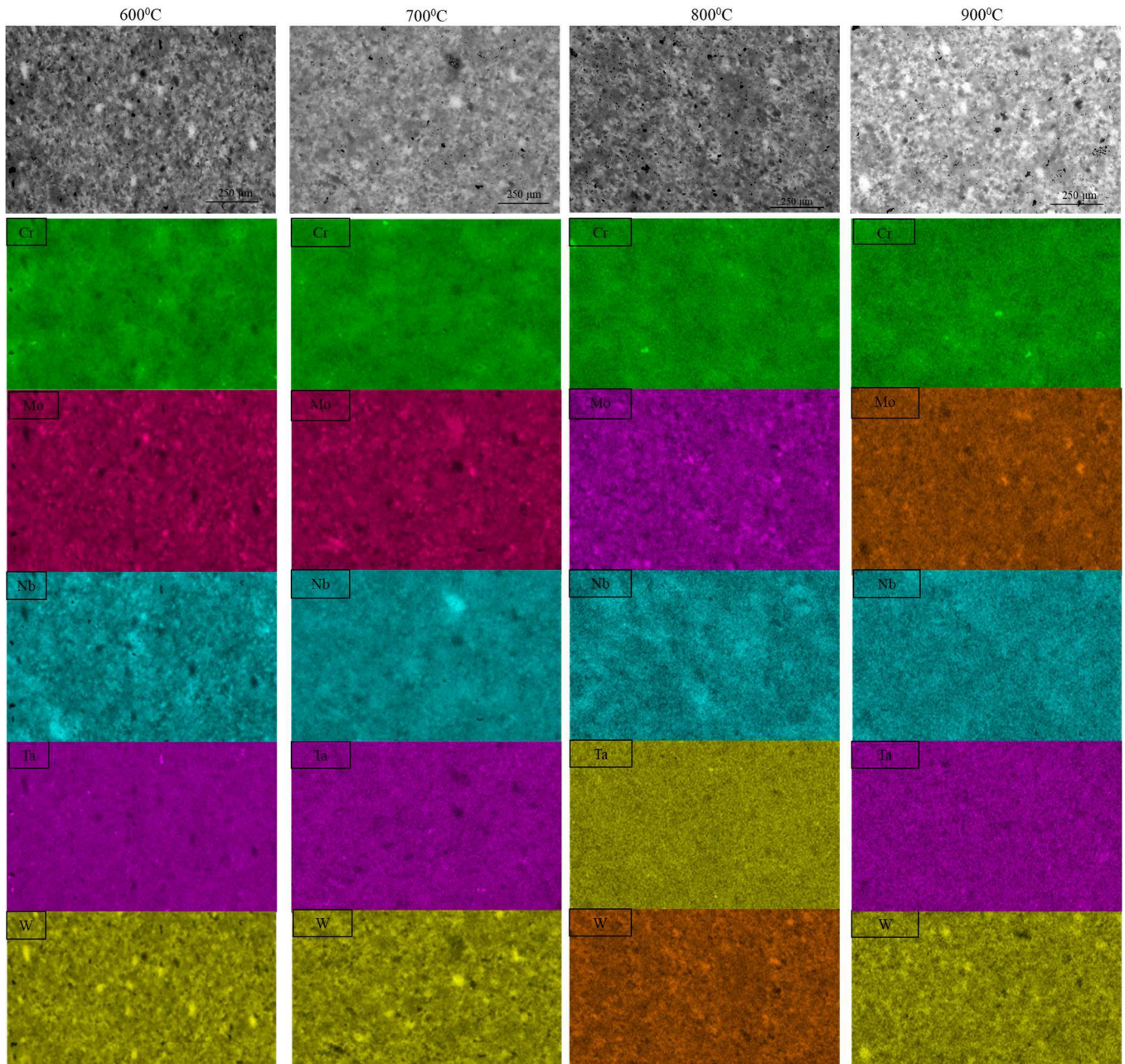


Figure 148: Microstructures of the samples at their respective annealing temperatures after 6 hours.



	Cr	Mo	Nb	Ta	W
600°C	20.7	20.3	19.1	20.3	19.6
700°C	20.8	20.2	19.3	20.3	19.4
800°C	21.0	19.9	18.8	20.6	19.7
900°C	21.3	19.8	18.5	20.6	19.8

Figure 19: EDS color mapping of the four annealed samples at each respective temperature after 6 hours. The corresponding map sum spectrum providing the overall composition is provided in atomic percentage.

The microhardness of each annealed sample was measured in five randomly selected areas on the polished surface. Like the way the as-received sample was measured, the reading was taken in matrix areas. The results are presented in Table 7. The microhardness of the annealed samples is all higher than the as received sample, but does not show a clear trend. The standard deviation is highest in the sampled annealed at 600<sup>0</sup>C and decreases as the annealing temperature decreases.

Table 7: Microhardness results of the annealed samples at their respective temperatures after 6 hours.

						Mean	Std. Dev.
<b>600<sup>0</sup>C</b>	859	851	843	790	723	812	57.2
<b>700<sup>0</sup>C</b>	776	827	769	756	812	788	30.1
<b>800<sup>0</sup>C</b>	867	843	867	835	820	846	20.5
<b>900<sup>0</sup>C</b>	797	776	820	835	820	809	23.2

#### 4.2.3 Oxidation of a CrMoNbTaW HEA

Samples were continuously exposed to lab air at various temperatures for 12 and 24 hours respectively. Figure 20 illustrates the mass change per unit surface area of the samples. The curves shown are at 12 and 24 hours at temperatures of 600, 800, 900, 1000, 1100, 1200, 1300, and 1400<sup>0</sup>C. At both 12 and 24 hours, the curves indicate a parabolic mass gain until 1100<sup>0</sup>C. At 1200<sup>0</sup>C, both at 12 and 24 hours, the mass change begins to decrease. At 1300 and 1400<sup>0</sup>C, the alloys show a mass loss. A curve fit is included for the 12-hour oxidation curve, as there indicated a slight increase from 1200 to 1300<sup>0</sup>C, however, because the difference is minimal, the variation is expected to be negligible.

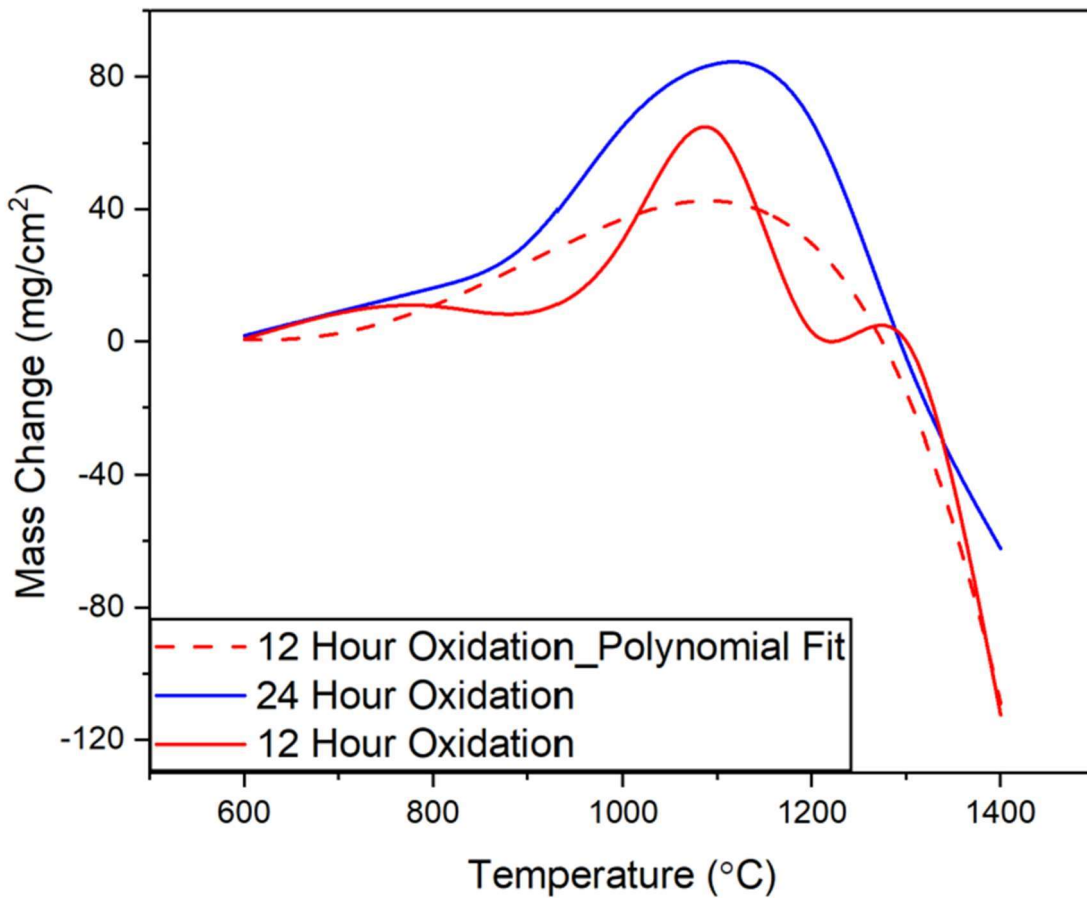


Figure 20: Oxidation curves of the mass change per surface area after 12 and 24 hours of oxidation in air versus time.

#### **4.2.3.1 12 Hour Oxidation**

The initial characterization and identification of the oxide scale after 12 hours of oxidation in the air are presented. SEM and EDS analysis are used to identify the morphology and composition of oxides present on the surface of the scale.

Figure 21 shows the progression of the oxide surface scale with increasing temperature. The oxide surface scale at 600°C begins as a very rough surface texture with no definite morphology. There are a few pores present on the surface, but generally, show the beginning stages of oxide growth. The sample oxidized at 800 and 900°C shows a similar rough surface but has more cracking along the surface and shows more oxide growth. At 1000°C, the oxide scale looks

as if it has grown outward more with rounded leaf-like shapes. The texture is still rough, like at 600 and 800<sup>0</sup>C. At 1100<sup>0</sup>C is when the oxide surface scale morphology begins to change, as there are small areas with some elongated areas of growth initiating. There is still cracking throughout the oxide scale but is not as rough as the texture was at lower temperatures. The oxide scale at 1200<sup>0</sup>C changes further, as the scale has a very granular texture and becomes more uniform. There is still significant cracking visible throughout the surface. At 1300<sup>0</sup>C, the surface of the oxide scale becomes more defined and there are now two definite morphologies of oxides: one of an elongated, rod-like structure, and one of a smaller, rounded, granular shape. The sample oxidized at 1400<sup>0</sup>C shows a coarsened, rod-like structure with a darkened, black structure dispersed on the oxides.

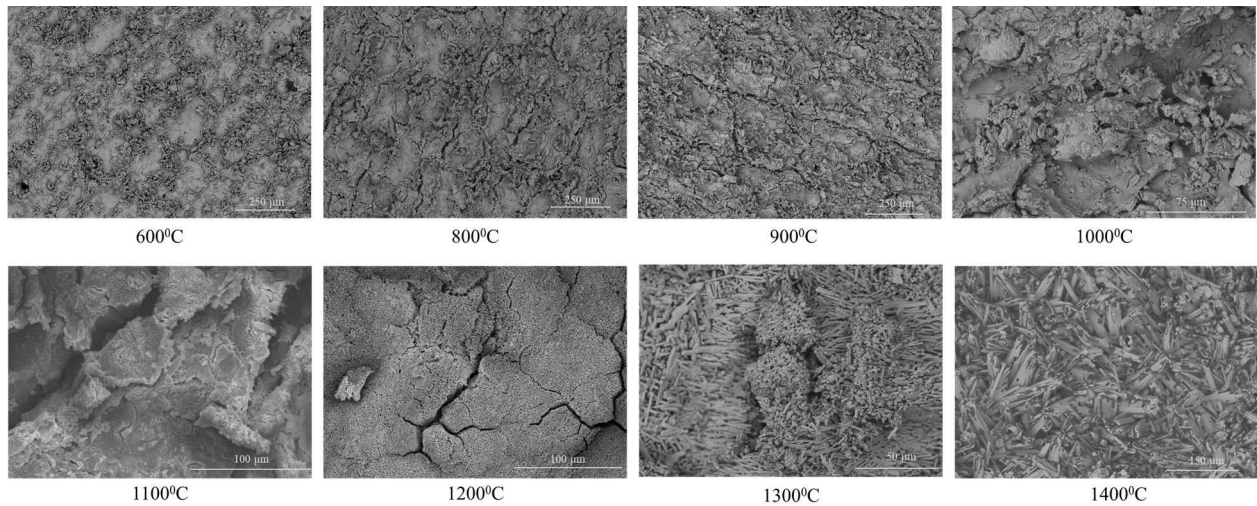


Figure 21: Surface oxide morphologies of the scale at each respective temperature after 12 hours of oxidation in air.

Figure 22 displays the color map of the oxide scale for the 600<sup>0</sup>C. The oxide scale is very uniform and does not indicate any segregation of any of the elements or concentrated areas. The map sum of the EDS spectrum identifies a nearly equiatomic amount of elements relative to one another. As the temperature is increased to 1100<sup>0</sup>C, Figure 23 shows where the morphology begins to change and that there is a clear indication that not only has the morphology changed, but the

chemical composition of the oxides present has changed as well. There are two distinct areas, one of a Cr-rich oxide and one depleted of Cr, a uniform mixture of Mo, Nb, Ta, and W. The Cr-rich area has a chemical composition very close to  $\text{CrTaO}_4$ , while the mixture has a composition of close to  $\text{NbTaO}_6$  with trace amounts of Mo and W. The other interesting characteristic at this temperature is that the Mo content present at the surface has significantly dropped, to only 0.6 at. %. At  $1400^{\circ}\text{C}$ , well-defined oxides are now visible and evident as shown in Figure 24. There are three types of oxides present, one that is Cr-rich with a composition of  $\text{CrTaO}_5$ . This is the focus of the image presented, as it is a rounded, granular structure. It is surrounded by a thick, elongated structure that is Nb-rich with a composition of  $\text{NbTaO}_6$ . Dispersed within the two oxides is a dark, globular oxide consisting of Ta and W containing an approximate composition of  $\text{TaO}_7$  with trace amounts of W. Mo is no longer present at the surface.

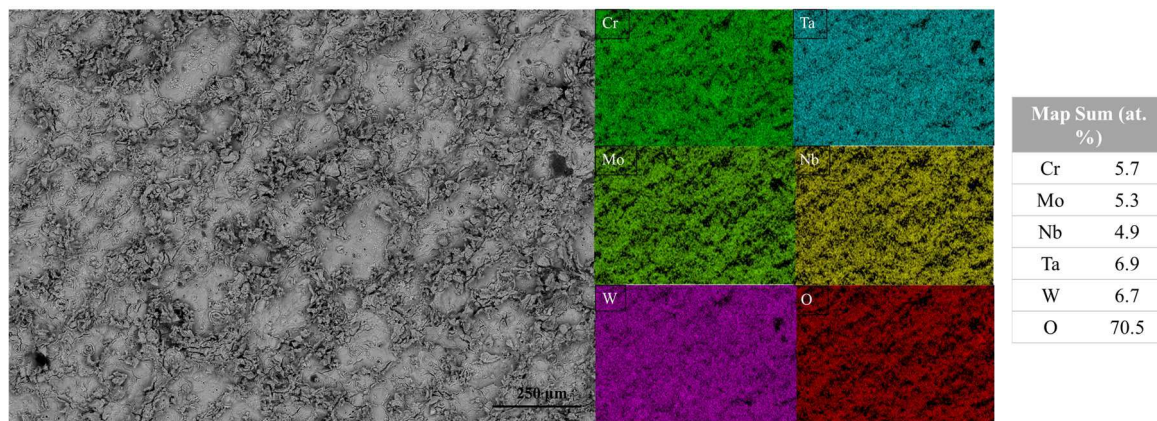


Figure 152: EDS color maps of the oxide scale after 12 hours of oxidation in air at  $600^{\circ}\text{C}$ .

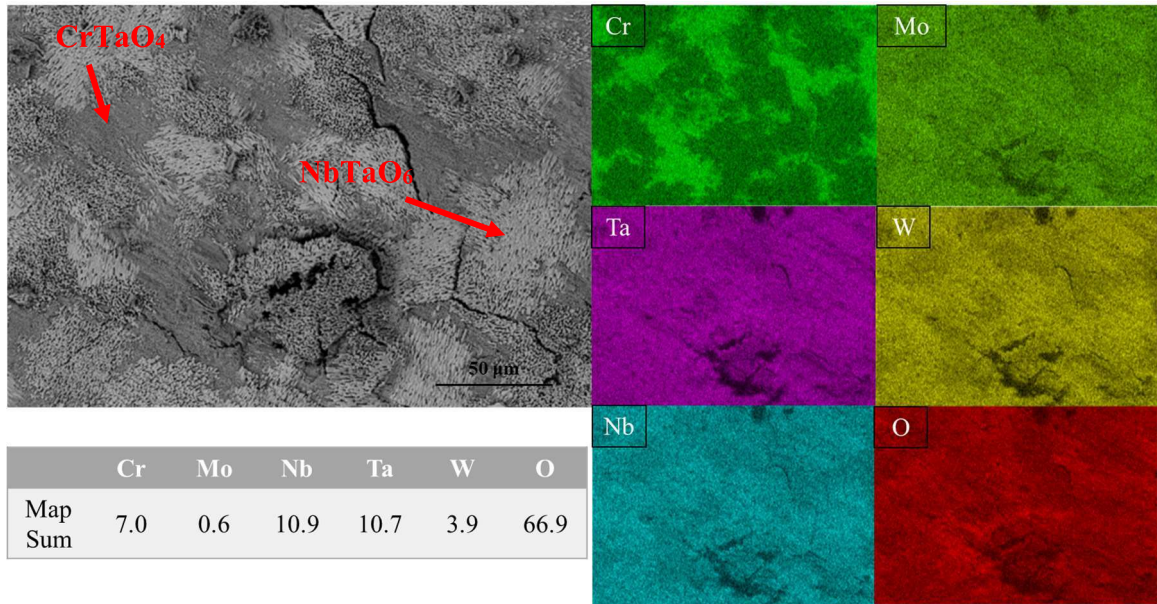


Figure 23: EDS color maps of the oxide scale after 12 hours of oxidation in air at 1100°C.

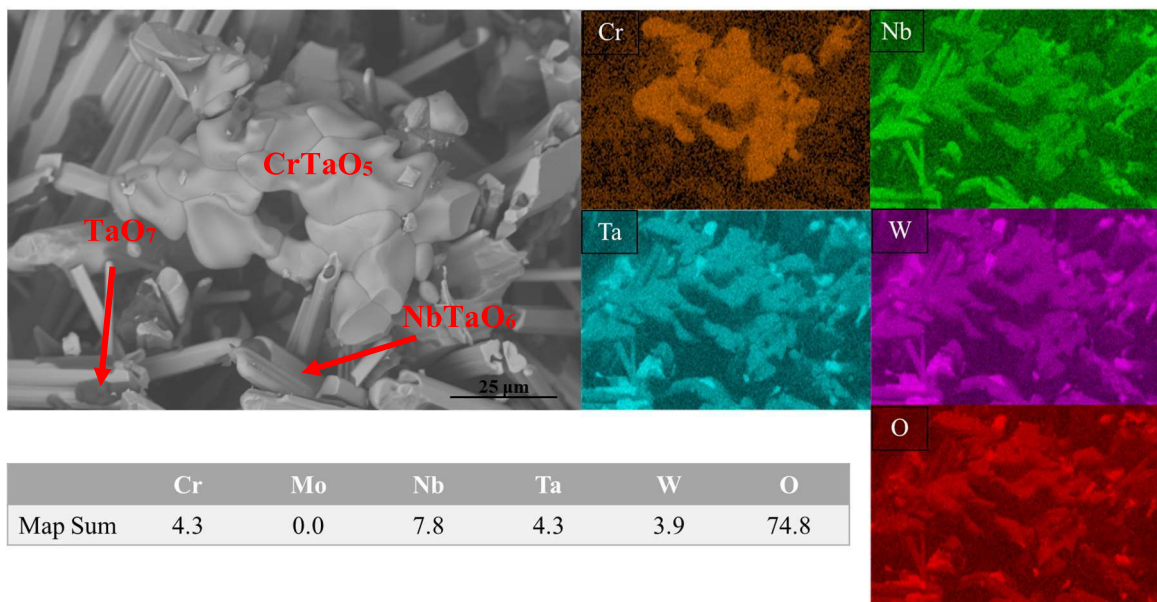


Figure 24: EDS color maps of the oxide scale after 12 hours of oxidation in air at 1400°C.

The XRD analysis was completed on samples after they were oxidized and cooled to room temperature. Figure 25 presents the XRD data of the samples at their oxidized temperature. At 600°C, the sample still retains some BCC peaks, similar to those identified in the as-received condition. There are also some peaks indicating a Ta<sub>2</sub>WO<sub>8</sub> structure and CrTaO<sub>4</sub> or CrNbO<sub>4</sub> structure. At 800°C the peaks related to the BCC structure are no longer visible, indicating the

surface has oxidized. The oxides seen are like those at 600°C. As the temperature increases, the peaks become stronger.

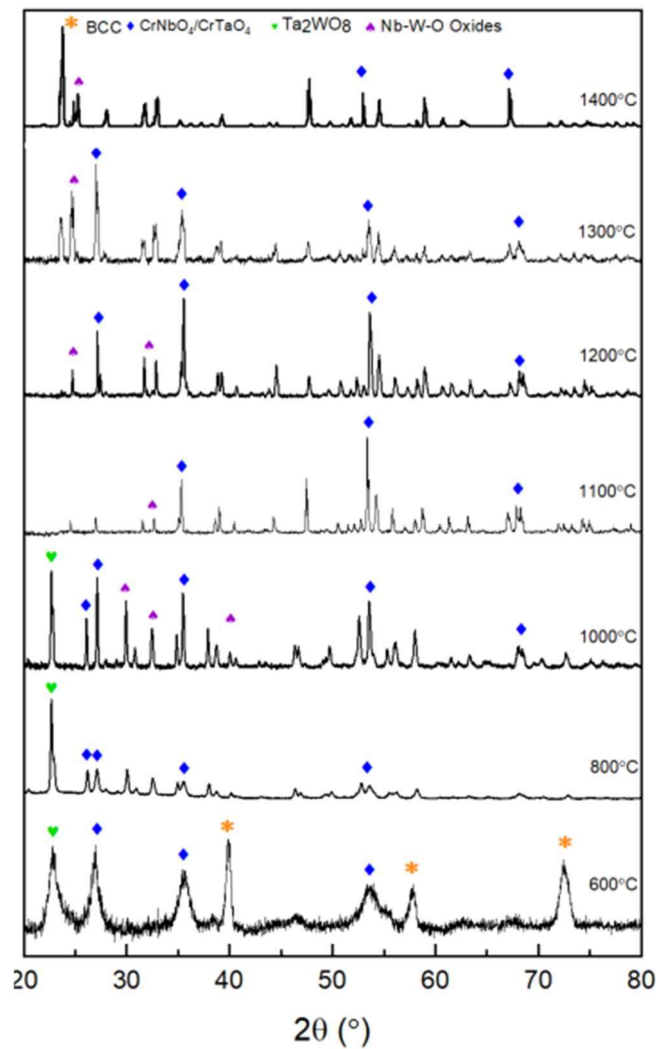


Figure 25: XRD of the oxidized samples after 12 hours of oxidation in air.

#### **4.2.3.2 24 Hour Oxidation**

Characterization and identification of the oxide scale after 24 hours of oxidation in the air are presented. SEM and EDS analysis are used to identify the morphology and composition of oxides present on the surface of the scale.

Figure 26 presents the surface of the oxide scales according to their respective oxidation temperature. The surface is showing a similar progression as during the 12-hour oxidation. At 600, 800, and  $900^{\circ}\text{C}$ , the oxide surface is very rough and shows cracking throughout. At  $1000^{\circ}\text{C}$  the scale has grown outwards and become more rounded and has porous areas visible. The morphology changes significantly at  $1100^{\circ}\text{C}$ , shown in Figure 27 where there are two distinct morphologies, one that is a rectangular, elongated structure and one that is smaller and appears as a clumped, granular structure. According to EDS spot analysis, there the granular, Cr-rich areas correspond closely to  $\text{CrTaO}_4$  following their atomic ratios, while the elongated structure has a composition of  $\text{NbTaO}_6$ . These areas are noted on the figure. These structures remain similar up until  $1400^{\circ}\text{C}$ , where the oxide, like at during 12 hours of oxidation, shows elongated rod-like oxides dispersed with dark, globular oxides as seen in Figure 28. This oxide appears to be Nb-enriched. Dispersed on top of the Nb-oxide are dark, globular oxides that are Ta and W enriched. The Nb-enriched oxide shows an atomic ratio relating to  $\text{NbTaO}_6$  which contain trace amounts of W, while the dark globular areas have a composition of  $\text{TaO}_5$ , showing less oxygen presence than the same oxide seen after 12 hours of oxidation. There are little amounts of Cr present that appear distributed throughout the oxide layer.

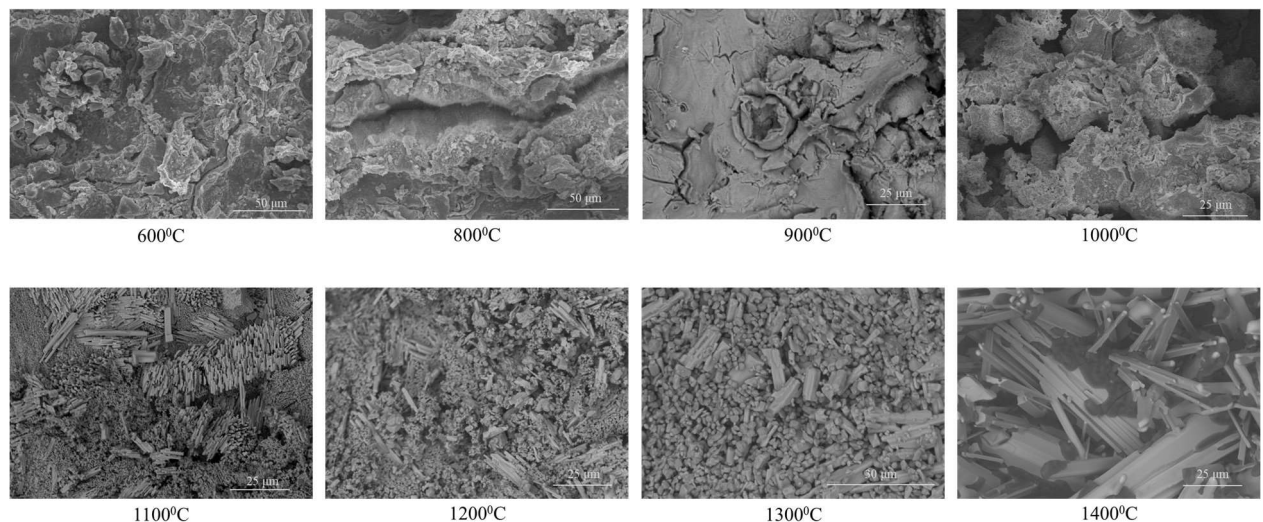


Figure 26: Surface oxide morphologies of the scale at each respective temperature after 24 hours of oxidation in air.

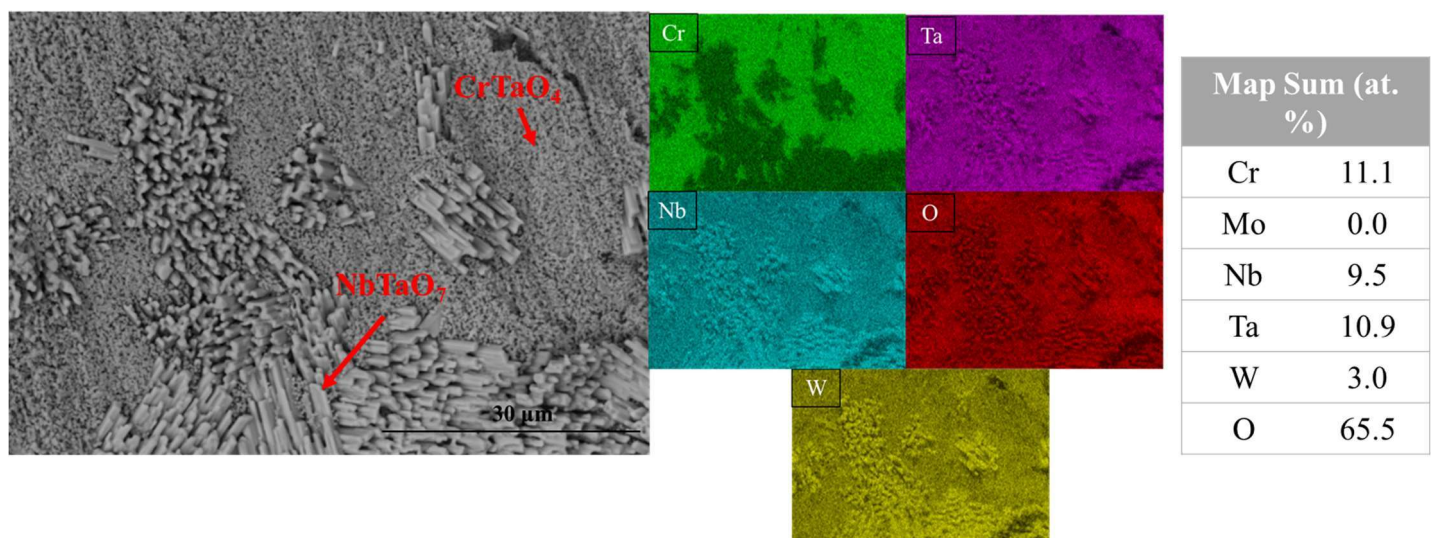


Figure 27: EDS color maps of the oxide scale after 24 hours of oxidation in air at  $1100^{\circ}\text{C}$

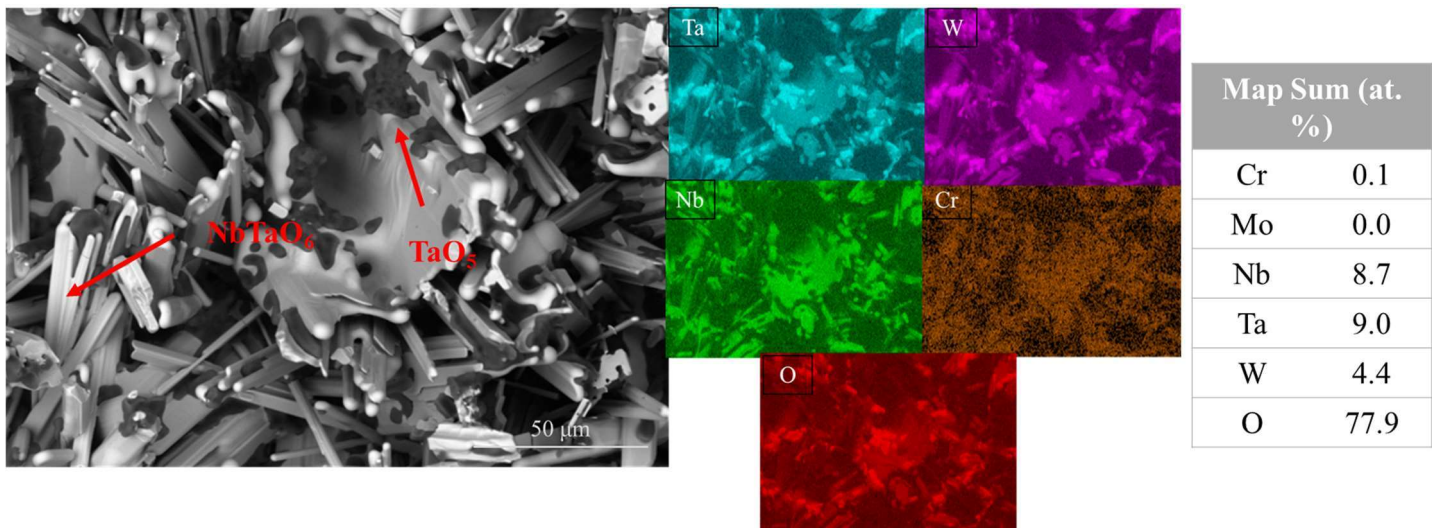


Figure 28: EDS color maps of the oxide scale after 24 hours of oxidation in air at  $1400^{\circ}\text{C}$

The XRD analysis run on the samples after they were oxidized and cooled to room temperature after 24 hours of oxidation is similar to those of 12-hour oxidation. Figure 29 presents the XRD data of the samples at their oxidized temperature. The  $600^{\circ}\text{C}$  sample still retains some BCC peaks, like those identified in the as-received condition. There are also some peaks indicating a  $\text{Ta}_2\text{WO}_8$  structure and  $\text{CrTaO}_4$  or  $\text{CrNbO}_4$  structure, along with peaks of a Cr-Nb nature. At  $800^{\circ}\text{C}$  the peaks related to the BCC structure are no longer visible. The oxides seen are like those at  $600^{\circ}\text{C}$  with the addition of peaks related to complex Nb-W oxides. As the temperature increases, the peaks become stronger and follow a structure of  $\text{CrTaO}_4$  or  $\text{CrNbO}_4$  and complex Nb-W oxides.

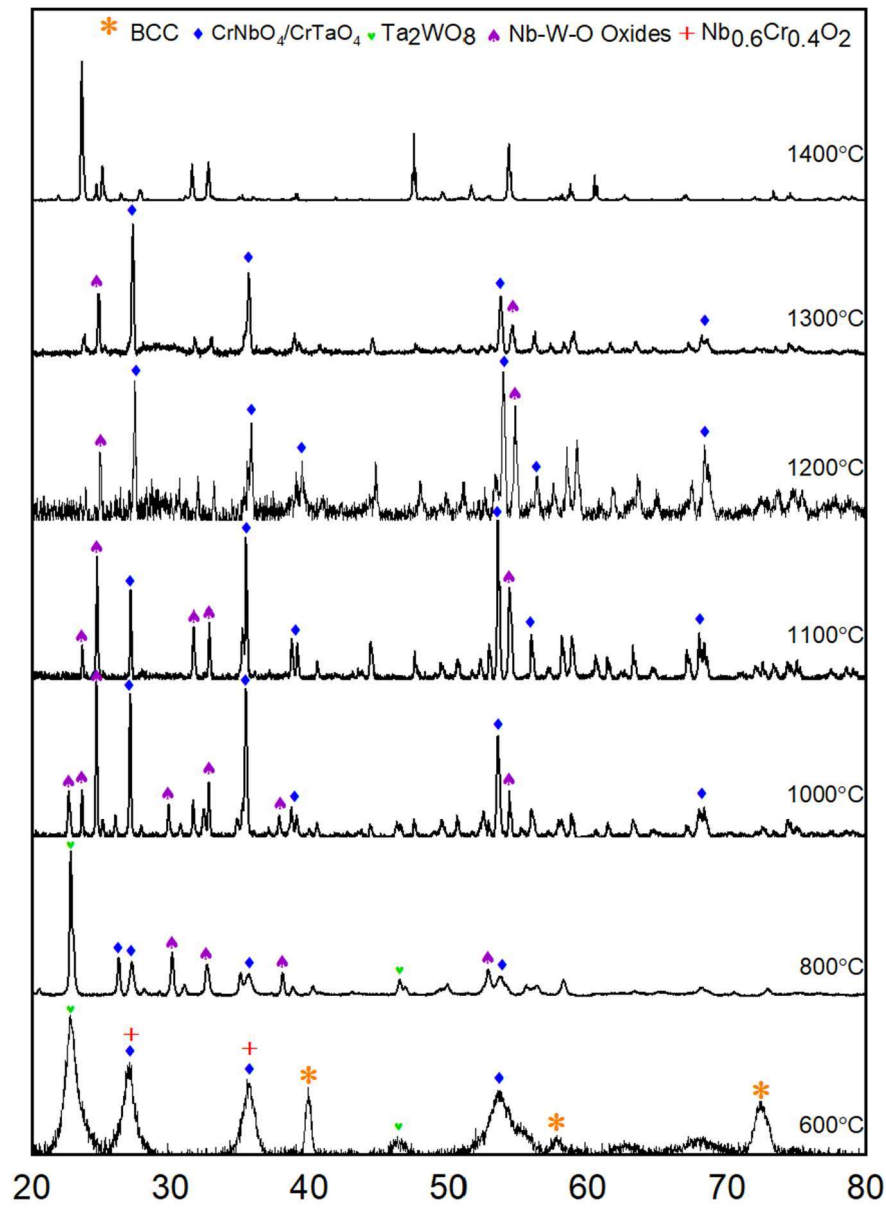


Figure 29: XRD of the oxidized samples after 24 hours of oxidation in air.

#### 4.3 Discussion of Alloys

Both a CrNbTaVW and CrMoNbTaW refractory high entropy alloy were evaluated for their potential in high temperature environments. The CrNbTaVW alloy had previously been deemed to have adequate oxidation resistance up to 800°C [55]. In this work, the oxidation of the

CrMoNbTaW alloy was evaluated in a similar way, however the oxidation resistance was considered adequate up to 1000°C after both 12 and 24 hours of oxidation. The surface oxides of both alloys were investigated and compared. Table 8 outlines the different oxides identified. The CrNbTaVW alloy exhibited two different oxides present at the surface up to 800°C, while the CrMoNbTaW alloy exhibited a uniform oxide scale with no clear structure. This shows that oxidation occurs more rapidly in the CrNbTaVW alloy, as oxidation does not appear to dominate the surface until 1100°C. Though they both do show some adequate oxidation resistance, neither alloys obtain the oxidation resistance of comparable commercial alloys, such as Inconel 718. For example, at 900°C after 24 hours of oxidation in air, Inconel 718 exhibits approximately 0.48-0.68 mg/cm<sup>2</sup> of mass gain [90], while the CrMoNbTaW alloy exhibited approximately 29 mg/cm<sup>2</sup>. This indicates that while these alloys have potential in high temperature environments, they do not yet show exceptional oxidation resistance, which is crucial in high temperature environments.

Table 8: Comparison of surface oxides in both alloys.

CrNbTaVW	CrMoNbTaW
<u>700-800°C (24 hours)</u> <ul style="list-style-type: none"> <li>• Granular, Cr-rich oxide</li> <li>• Elongated, rod-like W-rich oxide (<math>\text{NbTaW}_2\text{O}_{12}</math>)</li> <li>• Little V seen at the surface</li> </ul>	<u>600-1000°C (12, 24 hours)</u> <ul style="list-style-type: none"> <li>• Uniform oxide scale, no significant segregation of elements</li> <li>• Decreasing Mo content as temperature increases</li> </ul> <u>1100-1300°C (12, 24 hours)</u> <ul style="list-style-type: none"> <li>• Granular <math>\text{CrTaO}_4</math></li> <li>• Elongated <math>\text{NbTaO}_6</math></li> <li>• Trace amounts of W in both oxides</li> <li>• No Mo content</li> </ul> <u>1400°C (12, 24 hours)</u> <ul style="list-style-type: none"> <li>• Globular <math>\text{CrTaO}_5</math> (only after 12 hours)</li> </ul>

- |  |  |
|--|--|
|  | <ul style="list-style-type: none"><li>• Elongated rods of NbTaO<sub>6</sub></li><li>• Dark, globular oxides of TaO<sub>7</sub> dispersed on rods containing trace amounts of W</li></ul> |
|--|--|

## **Chapter Five: Atomistic Simulations Results and Discussion**

### **5.1 Introduction**

High entropy alloys have shown great promise in many research aspects and stimulated interest in further examination, however, difficulty processing and fabricating these alloys can be time consuming and expensive. Because of this, research efforts have been limited. On the other hand, as an easier, more efficient way of studying multiple chemical compositions, atomistic calculations can provide theoretical insight into various alloy compositions and help predict material behavior, including plastic deformation characteristics. The plastic deformation behavior of a series of multi-principal element alloys (4-component alloys) and high entropy alloys (5 and 6-component alloys) are examined. Four multi-principal element alloys (MPEAs) were evaluated: CrMoNbTa, CrNbTaW, MoNbTaV, and MoNbTaW. The goal is to understand what plastic deformation mechanisms may contribute to promising mechanical properties and evaluate what different chemical compositions have the potential to obtain the best strengths. Molecular statics (MS) simulations were performed on the four MPEA compositions to obtain the generalized stacking fault energy (GSFE) curves, and the local slip resistances (LSR) in both edge and screw dislocations on three different planes: {110}, {112}, and {123}. For comparison, the same calculations of the individual six pure metals were also evaluated, as well as the *A*-atom potential-based metals. As a further investigation, molecular dynamics (MD) simulations were conducted to understand the strength of a series of  $\text{CrMo}_x\text{NbTaVW}_{1-x}$  high entropy alloy families. Long dislocation lines (30 nm) were used of edge dislocations in the {110} and {112} plane and screw dislocations in the {112} plane. Both a defect-free and defect-containing (void) simulation cell were assessed to evaluate the strengthening effect of obstacles for a dislocation. The focus is placed on two main critical stresses: one that is required for the dislocation to glide in a void-free lattice

and one that is required for the dislocation to bypass a void. These critical stresses are known as the critical resolved shear stress. For reference, the individual pure metals were also evaluated.

## PART A: MOLECULAR STATICS

### 5.2 Molecular Statics Simulation Details

Large-scale atomic/molecular massively parallel simulator (LAMMPS) is used for MS work. The embedded-atom method (EAM) is used to describe the interatomic interactions of the four MPEAs evaluated. The six elemental potentials used are Cr [91], Mo [92], Nb [93], Ta [92], V [95], W [92]. The formulations of [95] and [96] are used as the basis of the cross interactions between the elements. This type of interatomic potential is termed the “alloy potential”. Of the four MPEA potentials, the MoNbTaW potential has been used in the literature [97]. For comparison, the *A*-atom potential will also be used, which provides a mean-field representation of the MPEA by approximating the interactions among different elements as a weighted average [98].

The lattice parameter,  $a_0$ , and the elastic constants  $C_{11}$ ,  $C_{12}$ , and  $C_{44}$  were calculated to assess the accuracy of the potentials used. A special quasi-random structure (SQS) [99] was built via ATAT [100] for each MPEA. Simple single crystalline structures were built for the pure metals and MPEAs with the *A*-atom potential. Following [101],  $a_0$  was calculated via the relaxation method. Elastic constants were obtained via the stress-strain method. The values were validated by DFT calculations.

GSFE curves and LSR values in the four MPEAs were calculated. The SQS was not used for these calculations; instead, a single crystal containing the same type of atoms was built for each MPEA which was based on the corresponding lattice parameter of each MPEA. To create the cell, one quarter of all atoms were randomly replaced with another type of atom, then another third of the remaining atoms are replaced with another type of atom, and then half of the remaining atoms

are replaced with another type of atom. The final simulation cell consisted of four types of atoms of equal amounts. 20 different atomic structures were built using 20 different sets of random number seeds. In the same MPEA, the simulation cells for GSFE curves and LR are built separately.

Relaxed GSFE curves along the  $<111>$  direction on  $\{110\}$ ,  $\{112\}$ , and  $\{123\}$  were calculated. Along each curve, 41 GSFE values were calculated. 20 different curves were obtained for each plane type in each MPEA. The unstable stacking fault energy (USFE),  $\gamma_{usf}$ , and the ideal shear strength,  $T_{is}$ , [102] were calculated from the GSFE curves. Further details of the simulation cell and calculation method can be found in [101]. The input files used for all GSFE calculations of the four MPEAs can be found in the GitHub repository: <https://github.com/shuozhixu/FLAM2020-GSFE>, GSFE curves of the six pure metals were provided for reference using the elemental potentials and four MPEA  $A$ -atom potentials were calculated.

All LSR calculations for edge and screw dislocations on the  $\{110\}$ ,  $\{112\}$ , and  $\{123\}$  planes were performed at 0K. A single edge or screw dislocation was inserted into a random atomic structure by applying the corresponding elastic displacement fields to all atoms. A shear strain was then incrementally increased ( $10^{-6}$  per step for screw and  $10^{-5}$  per step for edge) and applied until the dislocation moved at least one nm. 20 different LSR values were obtained for each MPEA of each dislocation and plane type. The mean, standard deviation, and coefficient of variation (COV) were then determined. Further details on the simulation cell and calculation methods can be found in [103]. The input files used for all LSR calculations of the four MPEAs can be found in the GitHub repository: <https://github.com/shuozhixu/FLAM2020-LSR>. The critical stresses required

for dislocation motion in pure metals in these cases are the “Peierls stresses”. The input files for these can be found in the GitHub repository: <https://github.com/shuozhixu/FLAM2020-PS>.

## 5.3 Molecular Statics Results

### 5.3.1 Lattice Parameters and Elastic Constants

The lattice parameters,  $a_0$ , elastic constants,  $C_{11}$ ,  $C_{12}$ , and  $C_{44}$ , and the Zener ratios of pure metals can be found in Table 9. The same calculations for the four MPEAs can be found in Table 10, along with the results based on  $A$ -atom potentials and simple rule of mixtures. The calculations presented are in good agreement with prior calculations according to [101]. In the MoNbTaV and MoNbTaW MPEAs, the calculated lattice parameters are consistent with the available experimental values of the alloys provided in the literature. Values calculated using the  $A$ -atom potentials and simple rule of mixtures are also consistent with the alloy potential, prior density functional theory (DFT) calculations, and experimental values (those available). In the CrNbTaW and CrMoNbTa compositions, the  $A$ -atom potential-based elastic constant calculations are lower than those calculated using the alloy potential. In the MoNbTaV and MoNbTaW compositions, the elastic constants using the  $A$ -atom potentials are similar.

Table 9: Lattice parameter and elastic constants for pure metals. Both MS and experimental values are provided.

	Method	$a_0$ (in Å)	$C_{11}$ (GPa)	$C_{12}$ (GPa)	$C_{44}$ (GPa)	$A_c$
Cr	MS [100]	2.881	398.03	93.45	103.56	0.68
	Exp [103]	2.885	348	67	100	0.71
Mo	MS [102]	3.135	458.76	167.84	114.32	0.79
	Exp [103]	3.147	465	163	109	0.72
Nb	MS [102]	3.3	263.56	125.28	35.03	0.51
	Exp [103]	3.301	245	132	28.4	0.5
Ta	MS [100]	3.303	262.59	157.74	82.33	1.57
	Exp [103]	3.303	264	158	82.6	1.56
V	MS [100]	3.026	263.93	120.19	38.37	0.53
	Exp [103]	3.024	230	120	43.1	0.78
W	MS [100]	3.165	522.54	204.22	160.76	1.01
	Exp [103]	3.165	523	203	160	1

The Zener ratio,  $A_c$ , is applied as a measure of the cubic elastic anisotropy. A value of unity represents ideal anisotropy. Three of the four MPEAs are nearly isotropic ( $A_c^{\text{MoNbTaW}} = 1.03$ ,  $A_c^{\text{MoNbTaV}} = 1.11$ ,  $A_c^{\text{CrNbTaW}} = 0.96$ ), while one is elastically anisotropic ( $A_c^{\text{CrMoNbTa}} = 0.72$ ) according to the alloy potentials. Results following the simple rule of mixtures provide similar results to MS results but are slightly elevated in the MoNbTaW and MoNbTaV compositions. The DFT calculations predict lower values of  $A_c$ , which consider all four compositions to be anisotropic.

Table 10: Lattice parameter and elastic constants of MPEAs calculated through MS and DFT and experimental values when available. Spin-polarization is not considered in any DFT calculations. Subscripts A and V denote results from A-atom potentials and simple rule of mixtures, respectively.

	Method	$a_0$ (in Å)	$C_{11}$ (GPa)	$C_{12}$ (GPa)	$C_{44}$ (GPa)	$A_c$
CrMoNbTa	MS [100]	3.171	320.33	144.34	68.68	0.78
	MS <sub>A</sub> [100]	3.175	262.11	111.36	54.28	0.72

	MS <sub>V</sub> [100]	3.16	330.50	130.00	80.00	0.80
	DFT [100]	3.179	333.89	145.19	58.69	0.62
CrNbTaW	MS [100]	3.179	333.18	161.81	82.03	0.96
	MS <sub>A</sub> [100]	3.188	277.43	127.31	64.21	0.86
	MS <sub>V</sub> [100]	3.16	345.00	140.00	92.75	0.90
	DFT [100]	3.189	332.1	161.93	60.2	0.71
MoNbTaV	MS [100]	3.206	263.72	144.15	66.43	1.11
	MS <sub>A</sub> [100]	3.204	263.32	144.69	68.91	1.16
	MS <sub>V</sub> [100]	3.19	301.00	143.25	65.78	0.83
	DFT	3.211	282.56	153.47	33.07	0.51
	Exp [104]	3.208	-	-	-	-
MoNbTaW	MS [100]	3.221	351.55	172.27	92.18	1.03
	MS <sub>A</sub> [100]	3.221	351.91	174.13	95.79	1.08
	MS <sub>V</sub> [100]	3.23	374.25	164.00	95.00	0.90
	MS <sub>SNAP</sub> [105]	3.244	399	166	80	0.69
	DFT [105]	3.242	377	160	69	0.64
	Exp [23]	3.2134	-	-	-	-

### 5.3.2 Generalized Stacking Fault Energy

Figure 30 presents the GSFE curves on all three slip planes in the four MPEAs. The calculations span a displacement over one periodicity distance along the  $z\langle 111 \rangle$  direction. The distance is also the Burgers vector magnitude of a full dislocation,  $b$ . GSFE curves based on both the alloy and  $A$ -atom potentials are shown.

The GSFE curves all reach a single peak value within the periodic length,  $b$ . The peak value is termed the USFE,  $\gamma_{\text{usf}}$ . There are no local minimum or metastable states. This is a particular characteristic exhibited by BCC metals [103, 107, 108].

The GSFE curves based on alloy potentials exhibit a slight deviation from the curves of  $A$ -atom potentials. This indicates an MPE effect that is the variation caused by the mixture of elements. As a result, even on the  $\{110\}$  plane whose GSFE curves are symmetric for pure metals, the USFE does not occur at a half lattice shift ( $b/2$ ) in most the MPEAs. This suggests that a single

GSFE calculation at  $b/2$  may not provide an accurate USFE and is related to the variation in the local atomic arrangement in which the MPEA is sampled. This variation suggests anisotropy in resistance to dislocation glide [103].

Figure 31 presents the summarized results of the mean USFE values. The CrNbTaW MPEA obtains the highest average USFE value, with the highest on the  $\{112\}$  plane. The MPEAs follow the order

$$\gamma_{\text{usf}}^{\text{MoNbTaV}} < \gamma_{\text{usf}}^{\text{MoNbTaW}} < \gamma_{\text{usf}}^{\text{CrMoNbTa}} < \gamma_{\text{usf}}^{\text{CrNbTaW}}$$

which holds on all three planes. For reference, the USFE values for pure metals can be found in Table 11. The USFE values of the pure metals on the three slip planes follow the order

$$\gamma_{\text{usf}}^{\text{V}} < \gamma_{\text{usf}}^{\text{Nb}} < \gamma_{\text{usf}}^{\text{Ta}} < \gamma_{\text{usf}}^{\text{Cr}} < \gamma_{\text{usf}}^{\text{Mo}} < \gamma_{\text{usf}}^{\text{W}}$$

The highest value of the pure metals,  $\gamma_{\text{usf}}^{\text{W}}$ , is approximately 300 mJ/m<sup>2</sup> higher than  $\gamma_{\text{usf}}^{\text{Mo}}$  on the three slip planes considered. As a result, the presence of W in CrNbTaW as opposed to Mo in CrMoNbTa can potentially explain the former's higher  $\gamma_{\text{usf}}$ . The same explanation can be applied to the difference in the MoNbTaW and MoNbTaV MPEAs and that between CrMoNbTa and MoNbTaV. Because  $\gamma_{\text{usf}}^{\text{V}}$  is the lowest calculated value among the pure metals, it is expected to contribute to a lower overall value in the MPEAs. Of the three planes studied for all pure metals and the four MPEAs, the  $\{112\}$  plane consistently attained the highest USFE value. When taken together, the highest USFE value was obtained by the CrNbTaW MPEA on the  $\{112\}$  plane. However, the COV is also the highest on the  $\{112\}$  plane. This large variation may be caused by changes in local chemical composition. Depending on the random atomic arrangement which was

surveyed, peak values may have occurred at larger ranges of values, which can cause a large COV. The variation may also relate to the size of sampled area. The smallest cross-sectional area used was in the {112} plane, approximately  $12 \text{ \AA}^2$ , while the {123} plane had the largest cross-sectional area, approximately  $58 \text{ \AA}^2$ . The increase in cross-sectional area leads to a lower COV, hence the lowest COV value in the {123} plane. The influence and size of the chemical environment has been proven to effect the variation in calculations [84].

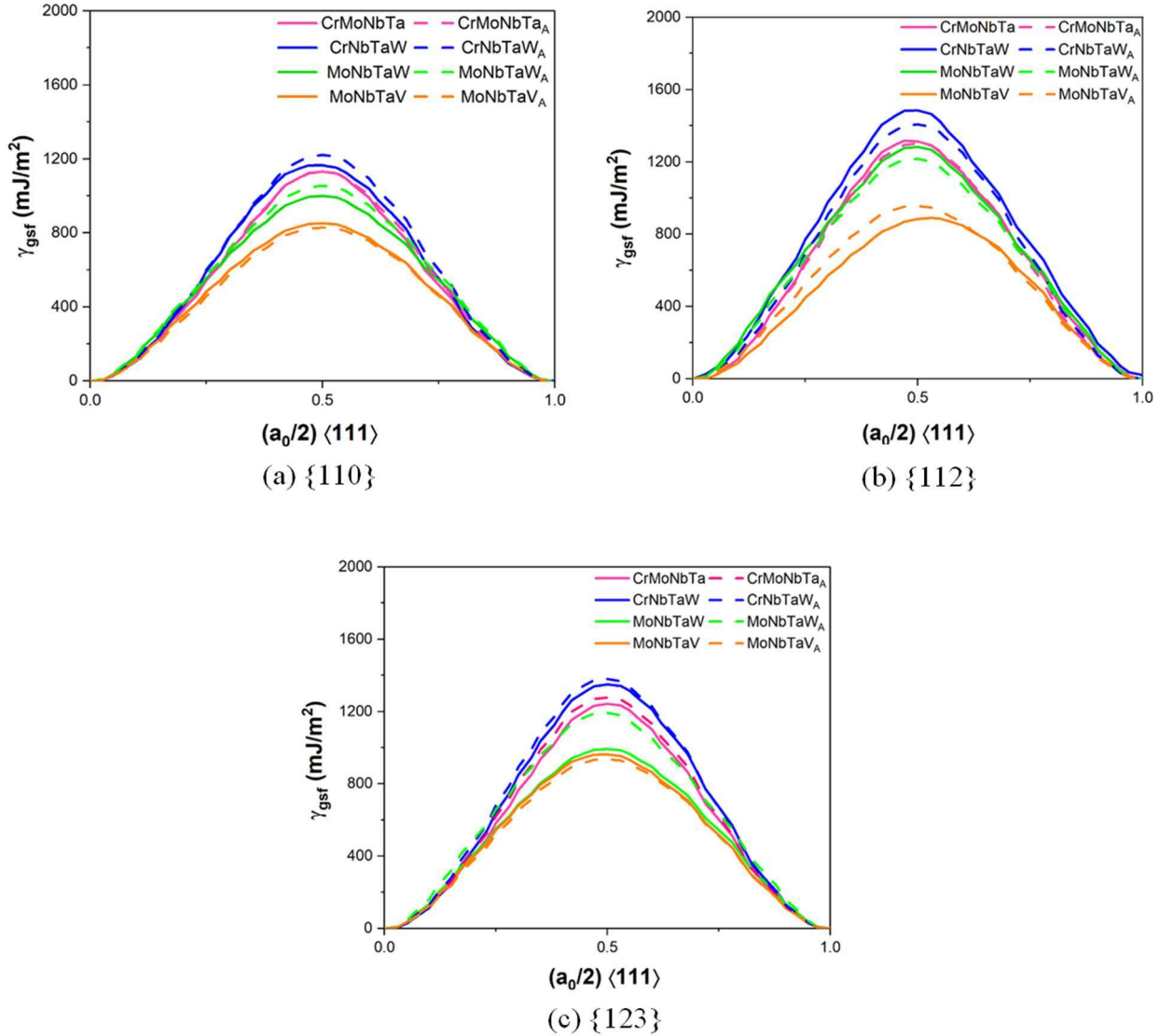


Figure 30: GSFE curves of four MPEAs on a)  $\{110\}$ , b)  $\{112\}$ , and c)  $\{123\}$  planes based on MS simulations using the alloy and A-atom potentials (subscript “A”).

Table 11: USFE values (in mJ/m<sup>2</sup>) of pure metals from both MS and DFT calculations. For Cr, DFT results without spin-polarization are presented here.

	Method	{110}	{112}	{123}
Cr	MS	1096	1265	1243
	DFT [106]	1565	1608	1628
Mo	MS [102]	1458	1689	1658
	DFT [106]	1443	1465	1481
Nb	MS [102]	605	697	685
	DFT [106]	677	769	767
Ta	MS [107]	751	868	852
	DFT [106]	724	838	832
V	MS	581	669	657
	DFT [106]	701	816	792
W	MS [107]	1740	2011	1976
	DFT [106]	1773	1846	1854

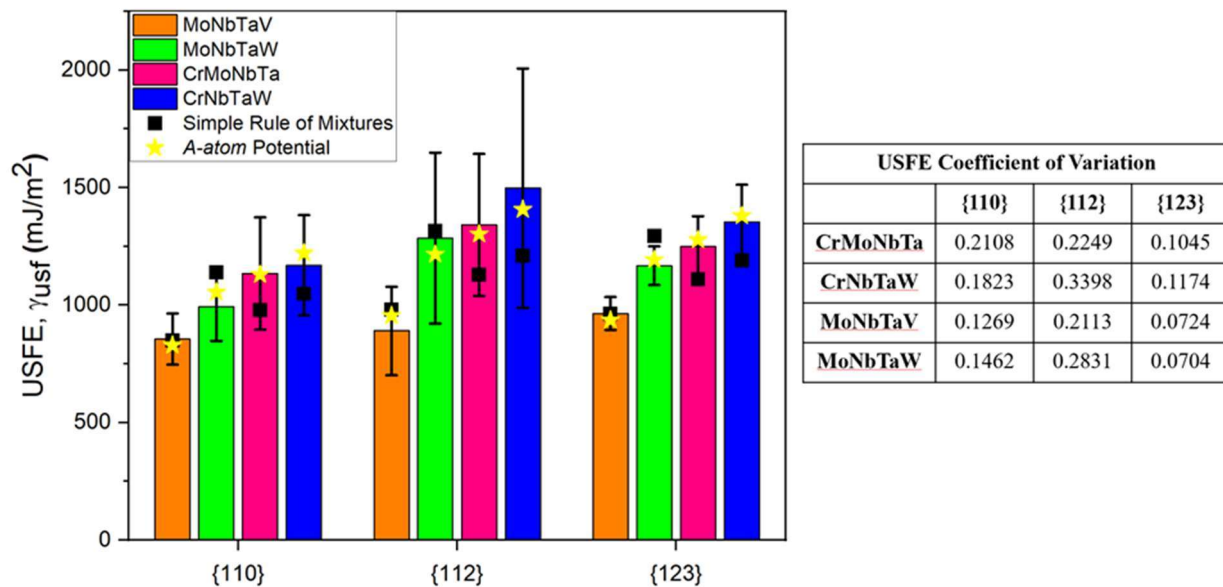


Figure 31: Average USFE values of MPEAs in the three planes and the COV.

It can be expected that the combination of Mo and W would yield a composition with the highest  $\gamma_{\text{usf}}$  value; however, this is not the case. As shown in Figure 31, the simple rule of mixtures estimation for  $\gamma_{\text{usf}}$  MoNbTaW on the {110} plane is 1139 mJ/m<sup>2</sup>, while the estimation of  $\gamma_{\text{usf}}$  for CrMoNbTa and  $\gamma_{\text{usf}}$  for CrNbTaW are 978 and 1048 mJ/m<sup>2</sup>, respectively. However, based on alloy potentials, the mean  $\gamma_{\text{usf}}$  for CrMoNbTa and that for CrNbTaW on the {110} plane is respectively 76 and 166 mJ/m<sup>2</sup> higher than the mean  $\gamma_{\text{usf}}$  for MoNbTaW on the same plane. These indicate that  $\gamma_{\text{usf}}$  cannot solely be considered based on constituent elements and their proportions. An estimation of  $\gamma_{\text{usf}}$  using simple rule of mixtures may not be accurate. Results based on the *A*-atom potentials are also included in Figure 30. They are in good agreement with those using alloy potentials. This indicates that calculations using *A*-atom potentials may provide more accurate estimates of  $\gamma_{\text{usf}}$  than the simple rule of mixtures.

The variation among curves of the same MPEA and plane type is due to the dispersion of the mean values. A different crystallographic plane from a random atomic arrangement in a 3D solid solution is evaluated for each GSFE curve. The change in atomic arrangement causes the variation in local maxima values. The Cr-containing compositions not only have higher overall USFE values, but also obtain higher standard deviations and COV. The COV is calculated from the 20 values of each MPEA and is presented in Figure 31. A higher COV gives rise to the MPEA effect as a variation among the curves. This may be due to the presence of Cr that causes increased lattice distortion, which was considered when calculating the relaxed GSFE curves.

The ideal shear strength ( $T_{\text{is}}$ ) is calculated from the gradient of the GSFE curve as the maximum of these values. Figure 31 shows only the mean values of  $T_{\text{is}}$ . For reference, the  $T_{\text{is}}$  values calculated through MS and DFT are presented in Table 12. Similar to the USFE, the

CrNbTaW MPEA achieves the highest  $T_{is}$  value on all three planes, with the highest of the values on the {112} plane. The order also follows the same as seen in the USFE,

$$T_{is}^{\text{MoNbTaV}} < T_{is}^{\text{MoNbTaW}} < T_{is}^{\text{CrMoNbTa}} < T_{is}^{\text{CrNbTaW}}$$

A large standard deviation is associated with higher  $T_{is}$  values. The COV is given in the corresponding table in Figure 32. A large variation is once again related to a difference in local chemical composition and atomic arrangement along the different crystallographic planes that may be sampled. For comparison, the values of  $A$ -atom potential and estimation using the simple rule of mixtures are included. Like the USFE, results based on the  $A$ -atom potentials are close to those based on the alloy potentials. This indicates that the former provides a relatively accurate representation of  $T_{is}$ . However, unlike the  $A$ -atom potential, the data based on the simple rule of mixtures largely overestimates  $T_{is}$ . The largest difference was seen in the {110} and {112} planes in the three MPEAs containing Mo. This difference is most likely due to the high  $T_{is}$  values obtained in both planes for Mo, which inflate the average value calculation. This indicates that the values for pure metals used to calculate  $T_{is}$  must be accurate or the simple rule of mixtures is not a reliable model in this case. Note that the calculated  $T_{is}$  for those MPEAs that do not contain Mo are also overestimated on the {110} and {112} planes, which further proves that a prediction using the simple rule of mixtures is not always accurate.

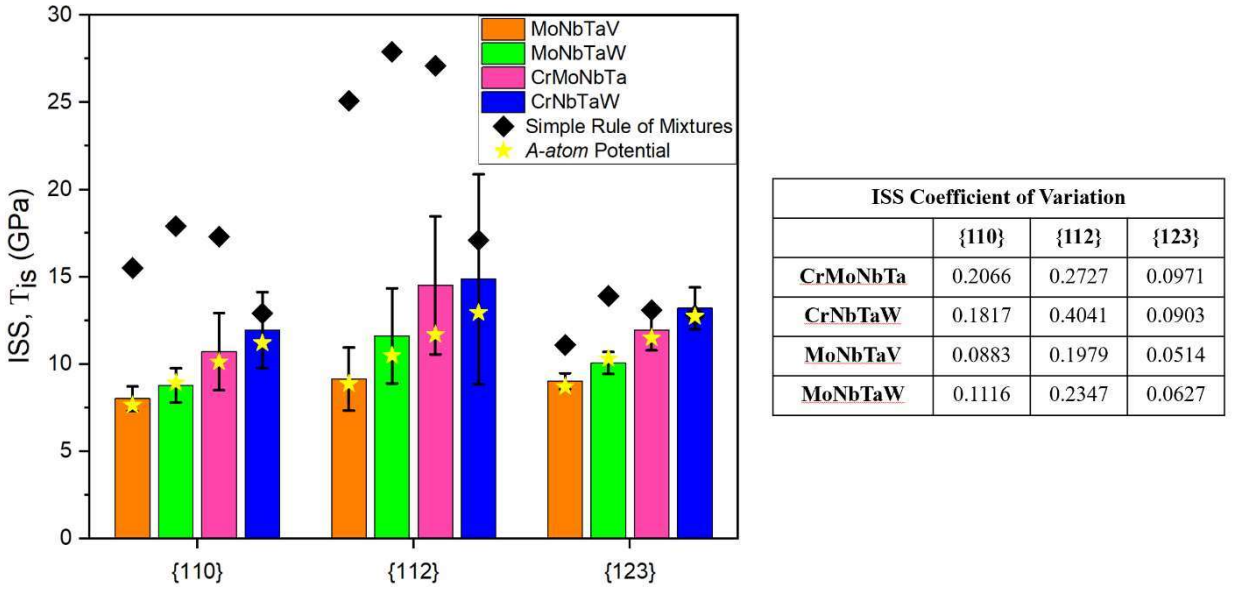


Figure 32: Average ideal shear strength (ISS) values of four MPEAs in three slip planes and the COV for each composition

Table 12: Ideal shear strength values (in GPa) of the reference pure metals for both MS and DFT calculations. For Cr, DFT results without spin-polarization are presented here.

	Method	{110}	{112}	{123}
Cr	MS	13.3	15.3	15.1
	DFT [106]	20.8	26.1	24.65
Mo	MS [102]	33.1	58.4	19.3
	DFT [106]	17.7	21.7	20.4
Nb	MS [102]	14.1	24.5	8.1
	DFT [106]	7.5	9.9	8.9
Ta	MS [107]	8.7	10.1	9.9
	DFT [106]	7.8	11.4	10
V	MS	6.2	7.2	7.1
	DFT [106]	8.3	10.8	9.7
W	MS [107]	15.6	18.4	18.1
	DFT [106]	21	26.5	25

### **5.3.3 Local Slip Resistance**

#### **5.3.3.1 Peierls Stresses in Pure Metals and A-atom Potential Based MPEAs**

The Peierls stresses of both screw and edge dislocations for pure metals and MPEAs using the *A*-atom potentials on three planes — {110}, {112}, and {123} — are presented in Table 13. Values of the Peierls stress were all calculable for edge dislocations; however, many cases were incalculable in screw dislocations. Incalculable Peierls stress or incalculable LSR here refers to when the screw dislocation is unstable and cross slips, hence the critical stress for habit plane cannot be calculated. Discussions for incalculable screw dislocation Peierls stresses have previously been presented by [109]. Among the screw dislocations on the {110} plane, only the Peierls stress in Cr was calculable. The Peierls stresses of screw dislocations in all pure metals except Cr were calculable on the {112} plane. There were no calculable screw Peierls stress values on the {123} plane for any pure metals. On all three planes, Cr has the highest Peierls stress among the six pure metals considered. Estimations of LSR of the MPEAs following the simple rule of mixtures based on the results of the pure metals can be found in Table 13. Calculations for the MPEAs using the *A*-atom potentials are also included. For the *A*-atom potentials, none of the screw dislocation Peierls stresses in the {110} and {123} planes were calculable, while all were calculable in the {112} plane. All edge dislocations on all planes were once again calculable. The calculated values on the {110} plane for the edge dislocations were all similar, ranging from 4.09 MPa for MoNbTaW<sub>A</sub> to 4.74 MPa for CrNbTaW<sub>A</sub>. However, this is not the case for either {112} or {123} plane, on which the MoNbTaW<sub>A</sub> MPEA obtains the highest Peierls stress for edge dislocations.

Table 13: Peierls stresses and LSR values, in units of MPa, of (a) pure metals, (b) MPEAs based on simple rule of mixtures estimation, (c) MPEAs based on A-atom potentials, and (d) MPEAs based on alloy potentials.

Plane	Dislocation	Cr	Mo [108]	Nb [108]	Ta	V	W
{110}	Edge	102	50	6	13	9	55
	Screw	3631	-	-	-	-	-
{112}	Edge	900	533	118	276	119	411
	Screw	-	2496	859	2137	817	3427
{123}	Edge	245	160	12	30	10	86
	Screw	-	-	-	-	-	-

(a) Peierls stresses of six pure metals

Plane	Dislocation	CrMoNbTav	CrNbTaWv	MoNbTaWv	MoNbTaVv
{110}	Edge	43	44	31	20
	Screw	-	-	-	-
{112}	Edge	457	426	335	262
	Screw	-	-	2230	1577
{123}	Edge	112	93	72	53
	Screw	-	-	-	-

(b) Simple rule of mixtures estimation of the LSR in MPEAs using the reference pure metals  
Peierls stress

Plane	Dislocation	CrMoNbTa <sub>A</sub>	CrNbTaW <sub>A</sub>	MoNbTaW <sub>A</sub>	MoNbTaV <sub>A</sub>
{110}	Edge	4.45	4.74	4.09	4.18
	Screw	-	-	-	-
{112}	Edge	41.9	5.65	84.15	9.005
	Screw	795.9	810.3	1158.4	335.76
{123}	Edge	3.168	3.47	5.25	2.95
	Screw	-	-	-	-

(c) Peierls stresses of four MPEAs using the *A*-atom potentials

Plane	Dislocation	CrMoNbTa		CrNbTaW		MoNbTaW		MoNbTaV	
		Mean	Std. Dev.	Mean	Std. Dev.	Mean	Std. Dev.	Mean	Std. Dev.
{110}	Edge	2003	1046	2183	937	912	402	1011	465
	Screw	2009	718	2619	405	1391	-	1274	202
{112}	Edge	1916	710	2115	882	1566	468	1188	364
	Screw	2405	620	2007	777	1421	553	1281	541
{123}	Edge	2011	525	2079	764	912	409	676	335
	Screw	2050	829	1822	856	1789	584	1130	269

(d) Mean LSR values of four MPEAs using the alloy potentials. Note, there is no standard deviation for the MoNbTaW screw dislocation on the {110} plane as there was only one calculable result.

### 5.3.3.2 LSR Values: Mean and Distribution

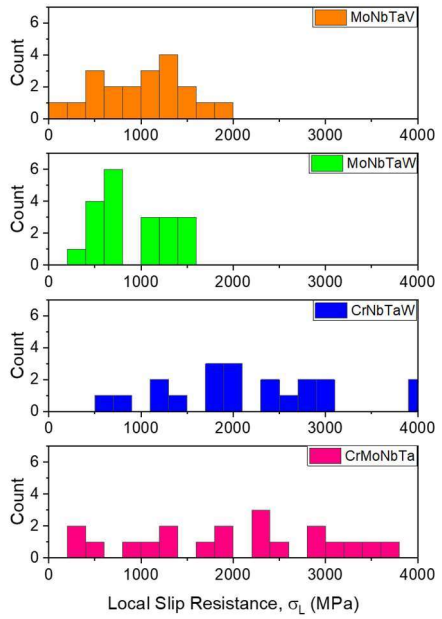
The mean and standard deviation of the 20 calculated LSR values for the four MPEAs are presented in Table 13. Among them, CrNbTaW obtained the highest LSR value of 2619 MPa on the {110} plane for the screw dislocation. This could not be compared to the Peierls stress of CrNbTaW<sub>A</sub> or the simple rule of mixtures-based value, as both were incalculable. In all cases, the mean LSR value was higher for the same MPEA than the corresponding Peierls stress using the A-atom potential. In both edge and screw dislocations on all planes, the Cr-containing MPEAs had higher mean LSR values than those without Cr. A higher mean LSR in the MPEAs containing Cr can be attributed to two factors: (1) a higher lattice distortion and (2) Cr pure metal has the highest Peierls stress. The effect of the lattice distortion will be discussed later.

Figure 33 shows the distribution of LSR values on all planes for both edge and screw dislocations. On the {110} plane for edge dislocations, the Cr-containing MPEAs have a large variation across the distribution. CrMoNbTa has a range of 3444 MPa and CrNbTaW has a range of 3366 MPa, while those without Cr have much smaller ranges. MoNbTaW has a range of 1353 MPa and MoNbTaV has a 1651 MPa range. Unlike the edge dislocation calculations, many of the

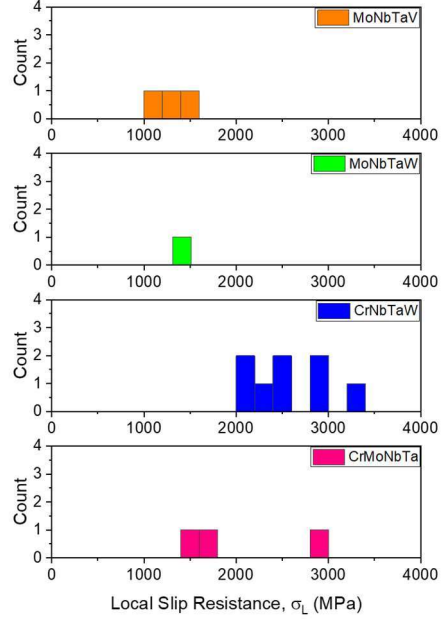
screw dislocation calculations were incalculable. CrNbTaW had the most calculable results among the four MPEAs with 8 out of the possible 20 results. The MoNbTaW MPEA had the least number of calculable results with only 1 out of the possible 20. Both CrMoNbTa and MoNbTaV had 3 out of 20 calculable results.

Like the  $\{110\}$  plane for edge dislocations, the Cr-containing MPEAs have a larger distribution for the edge dislocations, ranging from 398 to 3286 MPa for CrMoNbTa and 332 to 3302 MPa for CrNbTaW in the  $\{112\}$  plane. Despite a large variation, the mean LSR values of the Cr-containing MPEAs are higher. CrMoNbTa has 10 out of the possible 20 results and CrNbTaW has 11 out of the possible 20 results above 2000 MPa. MoNbTaW had only 5 out of the possible 20 LSR values above 2000 MPa, while MoNbTaV had none. For the same MPEA, screw dislocations in the  $\{112\}$  plane had a larger number of calculable LSR than those in the  $\{110\}$  plane. Once again, the Cr-containing compositions have a larger standard deviation, but obtain higher values of mean LSR compared to those without Cr.

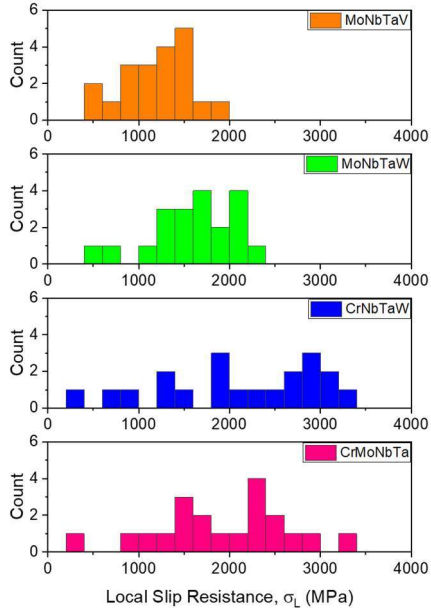
On the  $\{123\}$  plane, the mean and distribution of LSR are similar to those in the  $\{110\}$  and  $\{112\}$  planes. The CrMoNbTa and CrNbTaW compositions vary over large ranges but have more counts above 2000 MPa. MoNbTaW has only one count above 2000 MPa, while MoNbTaV does not have any. For the screw dislocations in the  $\{123\}$  plane, the results were calculable for approximately half of the time among all MPEAs.



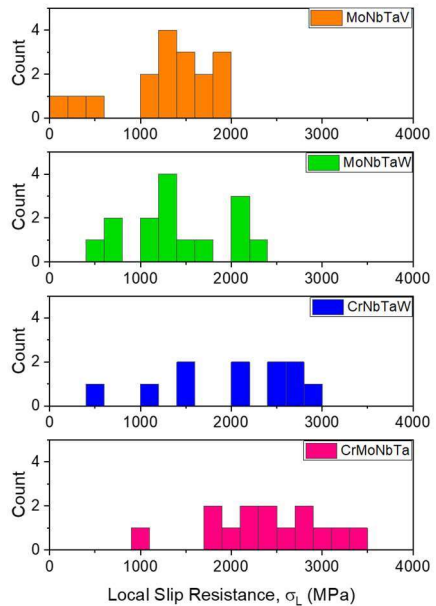
(a)  $\{110\}$  Edge



(b)  $\{110\}$  Screw



(c)  $\{112\}$  Edge



(d)  $\{112\}$  Screw

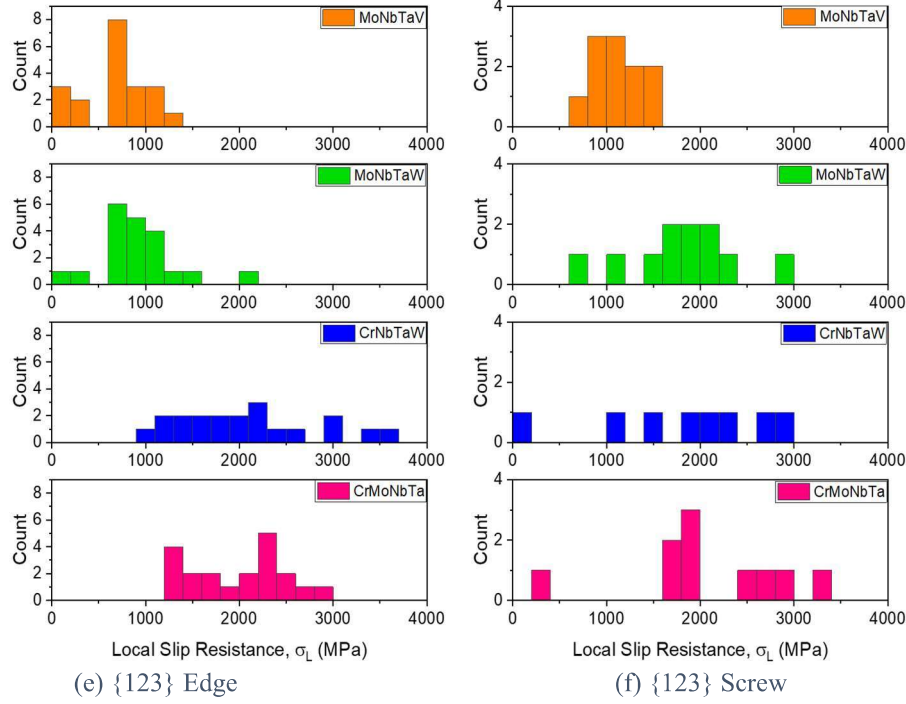


Figure 33: Distribution of the LSR of the four MPEAs on the (a) {110} edge plane, (b) {110} screw plane, (c) {112} edge plane, (d) {112} screw plane, (e) {123} edge plane, and the (f) {123} screw plane.

### 5.3.3.3 Slip Plane Anisotropy

Understanding the plastic anisotropy in BCC metals has proven to be significant since many of these mechanisms are not as well understood as in FCC metals . Xu et al., 2021 [109] proposed two measures of slip resistance anisotropy in MoNbTi. Wang et al., 2021 [108] then applied them to four BCC pure metals. One measure is based on the Peierls stress or LSR among different slip planes. When considering the ranking of the Peierls stress in pure metals, all six elements follow the order  $\sigma_p^{\{110\}} < \sigma_p^{\{123\}} < \sigma_p^{\{112\}}$ . Dislocation glide is considered and experimentally studied most frequently on the {110} plane and described as an elementary slip plane [109, 110]. Findings in pure metals match previous studies that dislocation glide occurs the easiest on the {110} plane. When considering the mean LSR values of edge dislocations of the

MPEAs, this ranking no longer matches. The results indicate that glide occurs easiest on the {112} plane and most difficult on the {123} plane in the CrMoNbTa MPEA. In contrast, glide is the easiest on the {123} plane and most difficult on the {110} plane in the CrNbTaW MPEA. Such findings differ from the pure metal behavior. Though rankings differ, the ranges of the mean values among different planes are very small, 95 MPa and 104 MPa, respectively in the two alloys of the edge dislocations. This suggests that slips may occur on any of the three planes and is dependent on the local chemical environment. MoNbTaW matches the pure metal behavior in that the slip is easiest on the {110} plane and most difficult on the {112} plane based on the mean LSR values. Similarly, glide is the most difficult on the {112} plane in the MoNbTaV alloy, while easiest on the {123} plane. In the MoNbTaW composition, the difference is near zero, as both the {110} and {123} average 912 MPa; however, the difference in mean values between the {110} and {123} planes of the MoNbTaV MPEA are much larger at 512 MPa. The small difference in mean on the {110} and {123} planes suggests that it is possible for slip to occur on either of the two planes. The difference between the mean LSR values for edge dislocations on either {110} or {123} and those on the {112} plane is much larger. The range of mean values of the MoNbTaW and MoNbTaV are 654 and 512 MPa respectively. This indicates that slip is significantly more difficult on the {112} plane for the two compositions. To quantify the slip resistance anisotropy among different slip planes, we calculated the COV in Peierls stresses and LSR among the three planes for edge and screw dislocations, respectively. Results are summarized in Table 14. The COV is the highest for edge dislocations in the MoNbTaW MPEA with a value of 0.346, and the COV in MoNbTaV is similar at 0.279. The two Cr-containing MPEAs have much lower COV's for edge dislocations at 0.027 and 0.025 respectively. This behavior does not follow suit for the screw dislocations, as the CrNbTaW COV is the highest with a value of 0.196 while the MoNbTaV

possesses the lowest COV of screw dislocations at 0.069. Overall, in the MPEAs, the two Cr-containing compositions, which have a larger lattice distortion, have smaller COVs than the other two MPEAs. The MPEAs' COVs are much smaller than those in *A*-atom potential-based MPEAs and pure metals, which are also presented in Table 14.

Table 14: COV across all planes for each dislocation.

	CrMoNbTa	CrNbTaW	MoNbTaV	MoNbTaW
Edge	0.027	0.025	0.279	0.346
Screw	0.101	0.196	0.069	0.145

- (a) COV of the four MPEAs based on alloy potentials across all three planes for each dislocation type.

	CrMoNbTa <sub>A</sub>	CrNbTaW <sub>A</sub>	MoNbTaV <sub>A</sub>	MoNbTaW <sub>A</sub>
Edge	2.622	0.242	0.666	3.768

- (b) COV of the four MPEAs based on *A*-atom potentials across all planes for the edge dislocation.

	Cr	Mo	Nb	Ta	V	W
Edge	1.507	1.561	3.088	3.094	2.868	1.580

- (c) COV of the Peierls stresses of the individual metals across all planes for the edge dislocation.

Another measure of the slip resistance anisotropy is the screw-to-edge ratio on the same slip plane. Table 15 reports these ratios in pure metals, *A*-atom potential-based MPEAs, and the alloy potential-based MPEAs. Because some screw dislocation calculations were incalculable due to instability, not all ratios could be determined. The calculations indicate a significantly decreased ratio in the MPEAs as compared to pure metals. On the {110} plane, only Cr can be compared, as the rest of the screw dislocations of the pure metals were unstable. The ratios of the MPEAs are much lower at 1.003 and 1.200 respectively for CrMoNbTa and CrNbTaW, compared to the much larger value of 35.6 for Cr. On the contrary, for the {112} plane, the ratio for every pure metal except Cr could be determined. The ratios of the MPEAs range from 0.908 to 1.255 which is approximately four to eight times less than the values for pure metals. Pure metals could be compared on the {123} plane, as none of the screw dislocations were calculable. The *A*-atom

potential-based ratios could only be determined on the  $\{112\}$  plane and, when compared to the alloy potential-based MPEAs, they are much higher. CrMoNbTa has the lowest ratio on the  $\{110\}$  plane, however all are relatively similar, with a range of only 0.252. CrNbTaW differs, in that the  $\{123\}$  plane contains the lowest ratio, however the range is still small, only 0.324. Both MoNbTaV and MoNbTaW have the lowest ratio on the  $\{112\}$  plane, being 0.908 and 1.079 respectively. These are two of the lowest ratios determined of the MPEAs. While these have low values, they do have a larger range on the three planes of 0.593 and 1.053 for the MoNbTaV and MoNbTaW compositions. Low screw-to-edge ratios in LSR have previously been reported [109], but only in one MPEA: MoNbTi. Here, the results show that the screw-to-edge ratios in LSR are lower in MPEAs with higher lattice distortion. In MoNbTaW, which has a low lattice distortion, previous atomstic simulations found that the edge-to-screw ratio in mobility on the  $\{110\}$  plane is as high as 20 at 300 K [112] and the dislocation loop expansion left no debris behind, unlike other BCC MPEAs with large lattice distortion [113].

Table 14: Screw-to-edge ratios in (a) pure metals, (b) MPEAs with A-atom potentials, and (c) MPEAs with alloy potentials.

Plane	Cr	Mo	Nb	Ta	V	W
$\{110\}$	35.6	-	-	-	-	-
$\{112\}$	-	4.68	7.28	7.74	6.87	8.34
$\{123\}$	-	-	-	-	-	-

(a) Screw-to-edge ratio of the Peierls stresses in pure metals

Plane	$\text{CrMoNbTa}_A$	$\text{CrNbTaW}_A$	$\text{MoNbTaW}_A$	$\text{MoNbTaV}_A$
$\{110\}$	-	-	-	-
$\{112\}$	19.0	143.4	13.8	37.3
$\{123\}$	-	-	-	-

(b) Screw-to-edge ratio of the Peierls stresses in  $A$ -atom potential-based MPEAs

Plane	$\text{CrMoNbTa}$	$\text{CrNbTaW}$	$\text{MoNbTaW}$	$\text{MoNbTaV}$
$\{110\}$	1.003	1.200	1.526	1.260
$\{112\}$	1.255	0.949	0.908	1.078
$\{123\}$	1.019	0.876	1.961	1.671

(c) Screw-to-edge ratio of the LSR in alloy potential-based MPEAs

### 5.3.3.4 Correlation Between the Ideal Shear Strength and the Mean LSR

The motivation for calculating both the GSFE curves and the LSR values was to compare the ideal shear strength, obtained from the GSFE curve, with the LSR. Figure 34 presents the ideal shear strength on each plane against the mean LSR value for both edge and screw dislocations. The correlation between the ideal shear strength and the LSR show a generally positive correlation. The  $\{112\}$  plane obtains a higher LSR and corresponding ideal shear strength for its relative MPEA for edge dislocations. The  $\{110\}$  and  $\{123\}$  planes obtained similar values. For screw dislocations, the  $\{110\}$  plane had the highest values and a strong positive correlation. The  $\{112\}$  and  $\{123\}$  planes show similar values; however, the positive correlation is the strongest on the  $\{112\}$  plane.

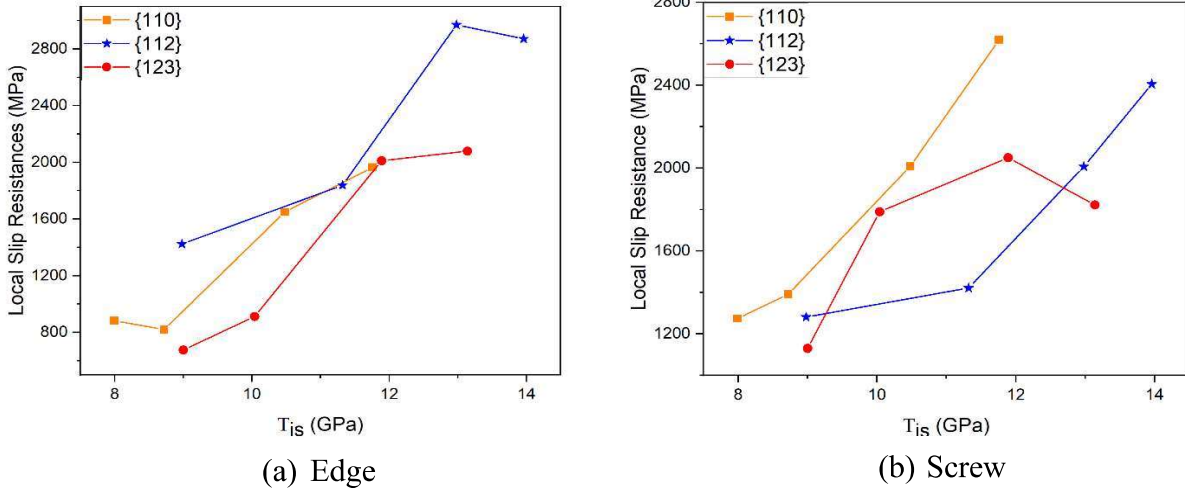


Figure 34: Mean local slip resistance (MPa) versus the ideal shear strength (GPa) for (a) edge and (b) screw dislocations in the four MPEAs.

### 5.3.4 Lattice Distortion

The effect of local lattice distortion induced by atomic size mismatch is one of the four core effects of MPEAs that contribute to the superior mechanical properties [19]. The energy caused by the lattice distortion in combination with high configurational entropy of mixing may significantly contribute to the thermodynamic stability of these alloys. In any alloy potential-based MPEAs, lattice distortion was naturally introduced following energy minimization. To quantify the lattice distortion, the atomic size mismatch is calculated by

$$\delta = 100 \sqrt{\sum_{i=1}^n c_i (1 - \frac{r_i}{\underline{r}})} \quad (1)$$

Where  $\underline{r} = \sum_{i=1}^n c_i r_i$  with  $c_i$  and  $r_i$  being the atomic percentage and atomic radius of element  $i$ , respectively [113]. Here, the atomic percentage for each component is 25% and the atomic radii can be derived from the lattice parameters of the six pure metals. Note that there is no lattice distortion in any pure metals or in any  $A$ -atom potential-based MPEAs. Table 15 shows the

lattice distortion in the four MPEAs calculated from Eq. 1. Of the six elements used, Cr has the smallest atomic radius, and is considerably lower than those of Nb and Ta. Thus, Cr-containing compositions had a higher mismatch estimation than those without Cr. The difference in atomic radii that increases the lattice mismatch is believed to be a significant contribution to the strength of the material [84, 115-120]. Lattice distortion has also shown to be influential on the dislocation behavior in MPEAs [121]. It has been shown that the lattice distortion creates local stress fields that cause a dislocation line to bend and enhance glide resistance.

Table 15: Calculated lattice distortion  $\delta$  values for the four MPEAs.

	CrMoNbTa	CrNbTaW	MoNbTaV	MoNbTaW
$\delta$	0.0545	0.0543	0.0367	0.0237

When comparing two different MPEAs, there are usually two differences: chemical compositions and lattice distortion. Both factors may contribute to the mechanical properties, such as strength. To understand which of the factors may play a more significant role, the quotient of the LSR by the simple rule of mixtures estimation was calculated. This is noted as the normalized value with respect to the lattice distortion in Figure 35(a). Similar plots are presented for the normalized USFE and normalized ideal shear strength, respectively, in Figure 35(b) and Figure 35(c). Since not all values of the simple rule of mixtures were calculable for the screw dislocations, only the edge dislocations were considered on each plane of the LSR calculations. On the {110} plane, normalized LSR in MoNbTaW is higher than both Cr-containing MPEAs. This result shows that lattice distortion effects are not the primary factor for strengthening for this plane. On the {112} and {123} planes, the normalized LSR in the Cr-containing MPEAs are either similar or slightly higher than those in MPEAs without Cr, suggesting that the lattice distortion serves as the

primary strengthening effect. In the meantime, the normalized USFE and normalized ideal shear strength positively correlate with the lattice distortion on the {110} and {123} planes, but not on the {112} planes. Taken together, the results suggest that whether the chemical composition or lattice distortion plays a more important role is strengthening differs among different slip planes.

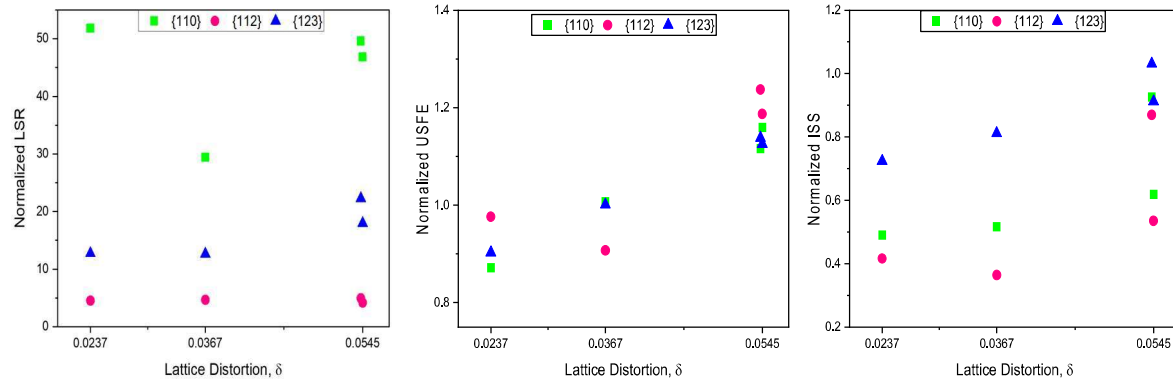


Figure 35: Plot of (a) normalized LSR, (b) normalized USFE, and (c) normalized ideal shear strength, with respect to the lattice distortion, in four MPEAs

On the three identified planes, the Peierls stress of Cr is nearly double the of the next closest value (either Mo or W) in edge dislocations. In all the edge dislocation calculations, the values obtained following simple rule of mixtures were much lower than the mean LSR values for the MPEAs but appear better than the results obtained from the *A*-atom potentials. This comparison indicates that estimating the LSR of MPEAs via the simple rule of mixtures or *A*-atom potentials is not an accurate representation of the stress required to move a dislocation.

### 5.3.5 Further Discussion

This work discusses the effects of lattice distortion and chemical composition to understand its role on four refractory MPEAs. An increase in strength has been experimentally studied in several refractory alloys, which have seen higher values compared to that of pure metals [23, 37-

39, 41, 42]. In these studies, the increased strength was attributed to a solid solution strengthening effect or a lattice distortion effect. Both the MoNbTaV and MoNbTaW compositions have been examined experimentally. In MoNbTaW, Han et al., 2018 [37] found that the compressive yield strength was 996 MPa at room temperature, while Senkov et al., 2011 [35] determined the value to be 1058 MPa. Both of were polycrystalline materials. In MoNbTaV, Yao et al., 2016 [36] showed that the compressive yield strength was 1525 MPa. These differ from the result obtained in this work, where MoNbTaW has higher LSR than MoNbTaV.

The GSFE and LSR calculations provide similar results in terms of which composition may perform better mechanically. Both calculations indicated that the Cr-containing compositions are superior to those without Cr. This result is attributed to the lattice distortion effect due to the small atomic size of Cr relative to the other elements. This was shown to the predominant factor according to the edge dislocations on the {112} and {123} planes, however not on the {110} plane. Increased lattice distortion has previously demonstrated a positive effect on the yield stress or lattice friction stress [84, 115, 122, 123]. Unlike this work, the previously mentioned studies did not contain all constituent elements of the same crystal structure (BCC or FCC), but rather mixed. This may have contributed to the increase lattice mismatch. The current work allowed for the opportunity to compare the two main factors, i.e., chemical compositions or lattice distortion. This was considered by the simple rule of mixtures, which averaged the values of individual elements. The results showed that the composition that had a higher calculated value using the simple rule of mixtures did not always have the highest calculated value based on the simulations. This implies that the lattice distortion is the predominant factor to benefit yield strength in some cases. Both calculations may also provide insight on the local chemical composition. The variation from a

symmetrical curve of the GSFE and large variations of the LSR values demonstrate alterations in the local chemical compositions.

The ideal shear strength was used to understand what the preferred glide plane is. The {110} plane obtained the lowest value for all four MPEA compositions. This indicates the {110} plane is the most likely slip plane for glide to occur, which is common of BCC metals. Though the {123} plane had slightly higher values, they were very comparable to those of the {110} plane, suggesting that slip may also occur on the {123} plane.

Among the four MPEAs, MoNbTaW had the highest screw-to-edge ratios on the respective plane on the {110} and {123} planes, but lowest on the {112} plane. This indicates that MoNbTaW has the highest degree of anisotropy on these two planes, while it had the lowest lattice distortion. The MPEA with the highest lattice distortion has the highest screw-to-edge ratio on the {112} plane, but the lowest of the four MPEAs on the {110} plane.

## PART B: MOLECULAR DYNAMICS

### **5.4 Molecular Dynamics Simulation Details**

As a continuation of the MS work, the further atomic simulations were run using MD to study the critical resolved shear stresses (CRSS) required for long dislocation (30nm) to glide in both a void-free and void-containing lattice. A series of six chemical compositions were studied following  $\text{CrMo}_x\text{NbTaVW}_{1-x}$  with  $x$  varying from 0 to 1 in increments of 0.2. For comparison, the same two stresses were studied in the six individual pure metals.

The simulation cells of the HEAs were constructed using the six randomly assigned chemical elements to BCC lattice sites. A single dislocation was built into each cell. This was done by applying the corresponding isotropic elastic displacement fields to all atoms [124, 125]. Edge

dislocations were studied on the {110} and {112} planes, while screw dislocations were only studied on the {112} plane.

A non-periodic y boundary was applied, while in the x and z directions, periodic boundaries were applied.  $L_x$ ,  $L_y$ , and  $L_z$  are the edge lengths of the cell along the three directions. For all cells,  $L_x \approx 40$  nm,  $L_y \approx 50$  nm, and  $L_z \approx 30$  nm following [126]. Embedded atom potentials are used to describe the interatomic interactions. The first peak stress of the stress strain curve related to the first dislocation movement of a void-free lattice and the first break away from a void in a void-containing lattice are reported as the CRSS.

The atomistic simulations are carried out using LAMMPS. A dynamic relaxation step for 10 ps was used using an NPT ensemble at 5K with zero strain applied with a step size of 1 fs. A shear strain tensor,  $\Delta\epsilon$ , with eight strain components set to zero and one set to non-zero is applied. A strain rate of  $10^7$  s<sup>-1</sup> is used for all cases. While deformation occurs, atoms within the boundary regions are continuously displaced to create shearing. Atomistic movements are visualized using OVITO.

#### **5.4.1 Molecular Dynamics Results**

The focus is placed on two main stresses: one is the stress required for a long dislocation line to glide in a void-free lattice and the second is to identify the stress required for a dislocation to bypass a void. The objective is to understand the strengthening effect that an obstacle may play to hinder dislocation movement in different HEAs. Since plastic deformation behavior and strengthening is related to the inhibition of dislocation movement, it is expected that an obstacle would play a role.

When the simulation cell is subject to an applied shear strain, the dislocation experiences either multiple movements in the void-free lattice or multiple bypasses of a void. For this reason,

only the first peak on a stress-strain curve that is related to the first movement or bypass of the void is reported in this work.

To understand how the stress-strain curve is related to the dislocation movement, Figure 36 presents a schematic representation. There are key points on the stress-strain curve and how they relate to the position of the dislocation. Point a is the initial position of the dislocation, as strain is applied and increased, the dislocation begins to move towards the void. Upon interaction with the void, a small peak stress is experienced and then a slight drop. These are points b and c. As strain is further applied, the stress correspondingly increases until it reaches a peak value, denoted as d. This corresponds to the dislocation bowing around the void, attempting to break away. When the dislocation breaks away from the void, it experiences a rapid drop in stress, noted as point e. As strain is further applied, the dislocation continues to move through the simulation cell, thus an increase in stress begins and will repeat the process. This is noted as point f.

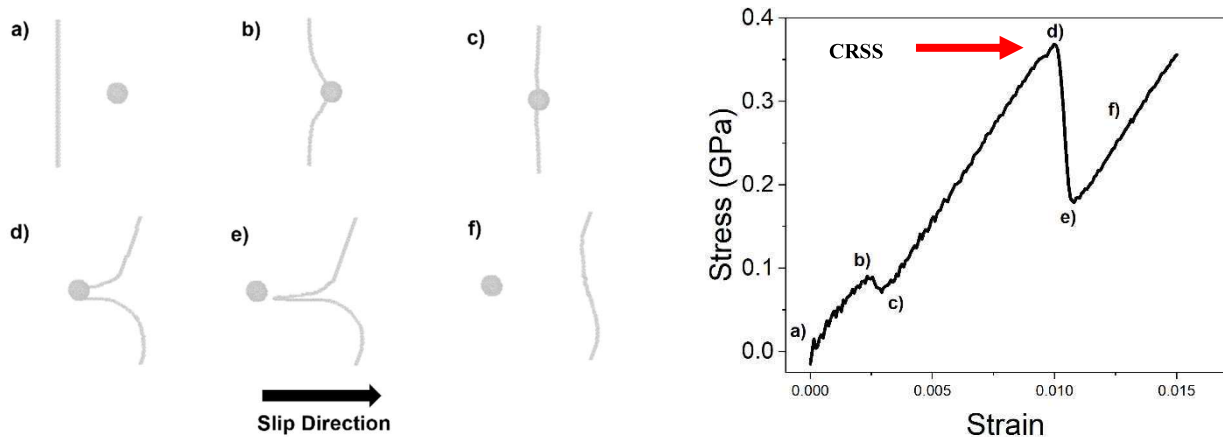


Figure 36: Depiction of the dislocation position according to the values indicated on the stress-strain curve.

#### 5.4.1.1 Critical Resolved Shear Stresses in Pure Metals

The stress-strain curves of the gliding (void-free) cases for edge dislocations on the {110} and {112} plane and screw dislocations on the {112} plane is presented in Figure 37. On the {110} plane for edge dislocations, the stress-strain curves are very noisy and similar among the six pure metals. The CRSS values of the pure metals are presented in Table 17. All six pure metals have relatively low values, indicating that dislocation glide is relatively easy for edge dislocations on the {110} plane. On the contrary, this differs for edge dislocations on the {112} plane, where the CRSS values increase, and Cr is significantly higher than the other five pure metals. The strain was increased to 0.005 for Cr because within the initial strain of 0.0035, there was no dislocation glide or peak on the stress-strain curve. For the screw dislocations on the same plane, the CRSS are significantly higher than the edge dislocations.

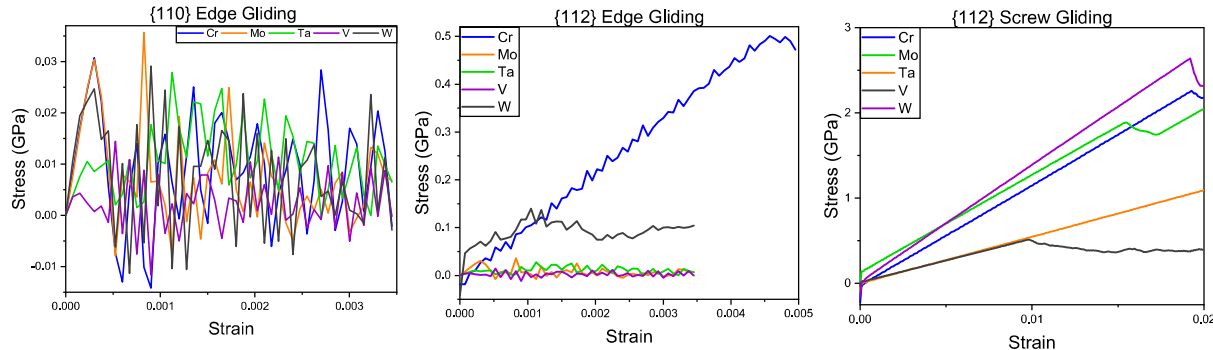


Figure 37: The stress-strain curves of pure metals in a void-free lattice.

In a void-containing lattice, the stress-strain curves of the pure metals exhibit a more uniform nature, especially in the {110} plane. The stress-strain curves are presented in Figure 38. The CRSS values obtained are significantly higher than in the void-free lattice. The values are listed in Table 16.

Table 16: CRSS of pure metals for both gliding and void-containing lattice.

		Cr	Mo	Nb	Ta	V	W
{110} Edge	CRSS <sub>glide</sub> (MPa)	31	30	11	11	14	25
	CRSS <sub>void</sub> (MPa)	687	639	179	413	194	771
{112} Edge	CRSS <sub>glide</sub> (MPa)	500	232	33		25	137
	CRSS <sub>void</sub> (MPa)	817	561	219	368	247	617
{112} Screw	CRSS <sub>glide</sub> (MPa)	2260	1889	509	1493	510	2638
	CRSS <sub>void</sub> (MPa)	-	1996	405	1552	510	2593

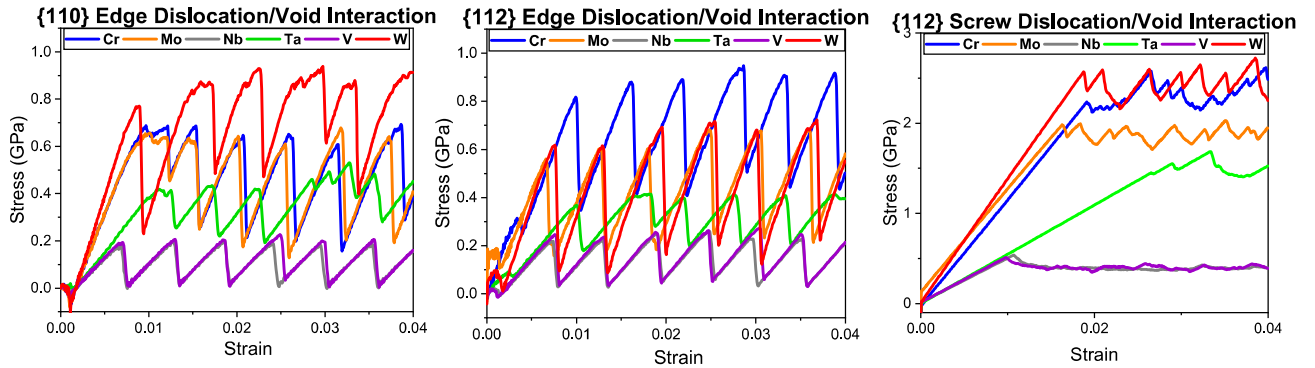


Figure 38: The stress-strain curves of pure metals in a void-containing lattice.

The strengthening effect of the void can be evaluated by dividing the CRSS<sub>void</sub> by the CRSS<sub>glide</sub>. Figure 39 presents these measures. The strongest strengthening effect is seen in edge dislocations on the {110} plane. The ratios range from 16-37, with the highest seen in Ta. The strengthening effect is not as strong on the {112} plane, especially for screw dislocations. For edge dislocations, the ratios range from 1.6-9.9, with the highest being V. The strengthening effect Ta could not be evaluated because of visualization issues of the dislocation in OVITO. For screw dislocations on the {112} plane, there was little to no strengthening effects seen, with some experiencing a loss in

stress in a void containing lattice such as the case in Nb. Similar to the Ta case in the edge dislocation, Cr could not be evaluated for the screw dislocation.

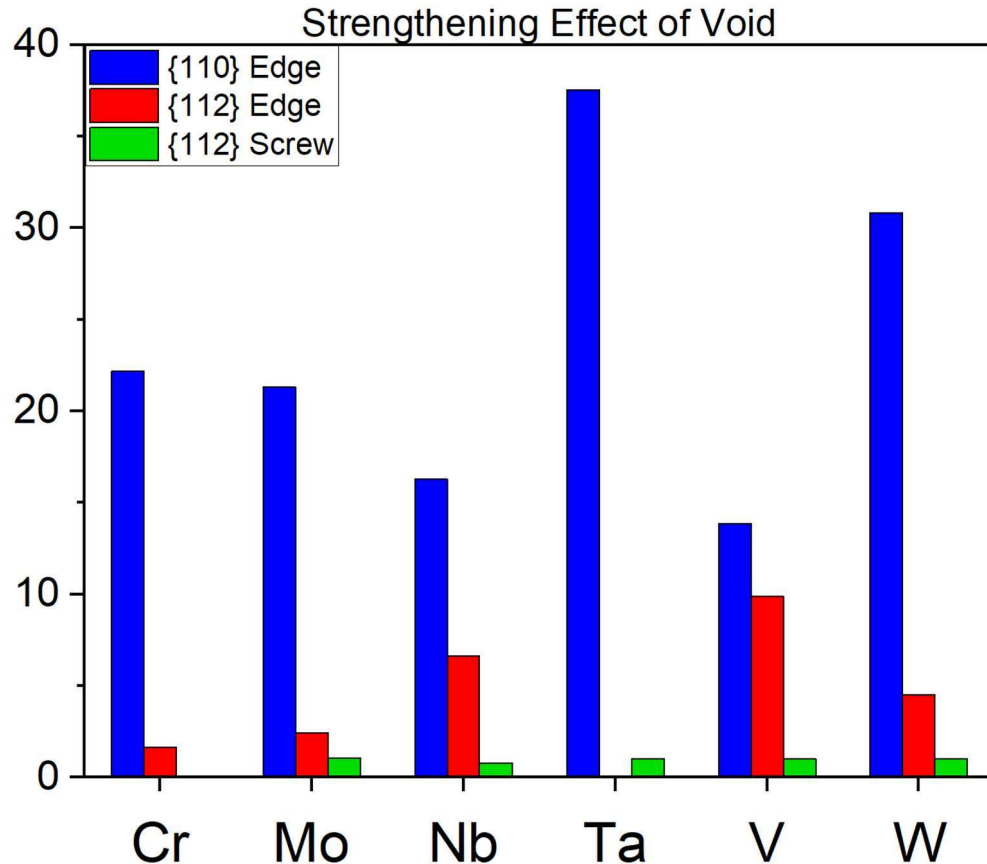


Figure 39: The strengthening effect of void-containing lattices.

#### **5.4.1.1 Critical Resolved Shear Stresses in HEAs**

The CRSS values of both gliding and void-containing cases of HEAs of  $\text{CrMo}_x\text{NbTaVW}_{1-x}$ , where  $x$  ranges from 0 to 1 in increments of 0.2 were evaluated. Just as the case in pure metals, the first movement or break away from the void is reported in this work. Table 17 outlines the CRSS for both glide and void cases for the six HEA compositions.

Table 17: CRSS for gliding and void-containing lattices.

		x = 0	x = 0.2	x = 0.4	x = 0.6	x = 0.8	x = 1
{110} Edge	CRSS <sub>glide</sub> (MPa)	2138	1930	1900	1732	1678	1825
	CRSS <sub>void</sub> (MPa)	2376	2757	2316	2525	2062	2200
{112} Edge	CRSS <sub>glide</sub> (MPa)	1469	1516	1650	1580	1487	1241
	CRSS <sub>void</sub> (MPa)	1879	1581	1772	1643	1806	1615
{112} Screw	CRSS <sub>glide</sub> (MPa)	1995	-	2413	2078	1959	1867
	CRSS <sub>void</sub> (MPa)	2153	2396	-	2279	2072	-

Figure 40 presents the CRSS for both the glide and void cases as a function of the amount of Mo present in increments of 0.2. For the glide cases, the general trend is that as the Mo amount increases, the CRSS decreases. This, however, is not always the case, specifically for the edge dislocation on the {112} plane. At x = 0.4, the CRSS increases and continues to decrease as Mo increases. The void cases show a different behavior, as there is a slight decreasing trend as Mo increases, but there is much variation.

Figure 41 shows the strengthening effect of voids in the critical resolved shear stress. Unlike in the case of pure metals, the strengthening effect is not always as strong on the {110} plane for edge dislocations. For those cases that the strengthening effect is the highest in that case, it is not significantly higher than the dislocations on the {112} plane. All the ratio values are similar, ranging from only 1 to only 1.4 at the highest value. The strengthening of the HEAs can

be attributed to the inherent strength obtained by the random atomic arrangement of atoms. The lattice distortion effect was also evaluated. Figure 42 shows the Mo content versus the CRSS<sub>Glide</sub> and lattice distortion. It is important to note that the lattice distortion does not change much, as the atomic radius of Mo and W are similar. It is expected that with an increase in lattice distortion would be an increase in strength, however this is not the case. This indicates that the lattice distortion does also not contribute to significant strengthening of the alloy and is dominated by other mechanisms.

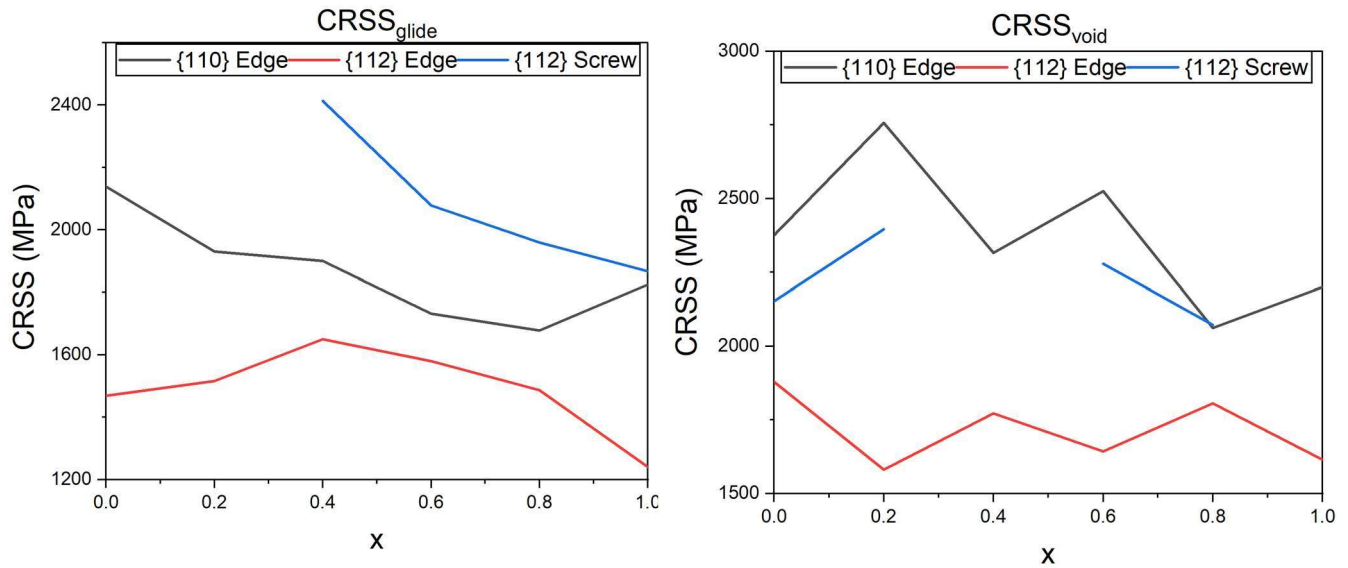


Figure 40: The CRSS of the gliding and void-containing cases of the HEAs as a function of x, Mo content.

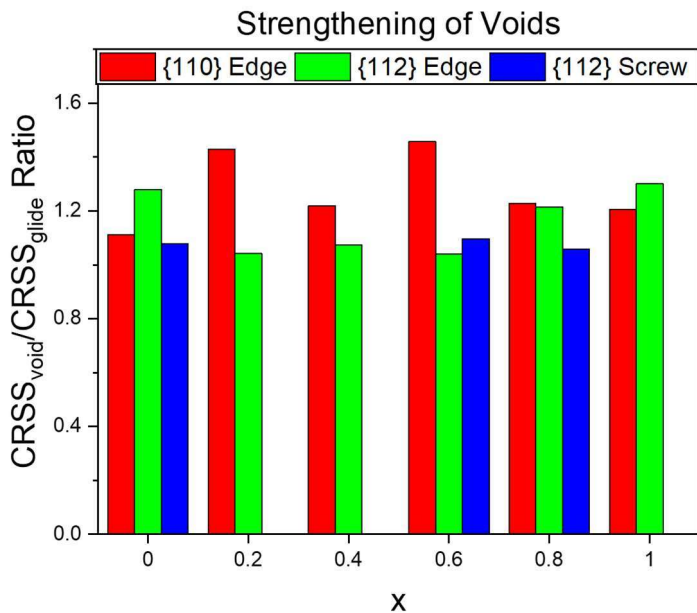


Figure 41: The ratio of the  $\text{CRSS}_{\text{void}}/\text{CRSS}_{\text{glide}}$  to represent the strengthening effect of voids present in the lattice.

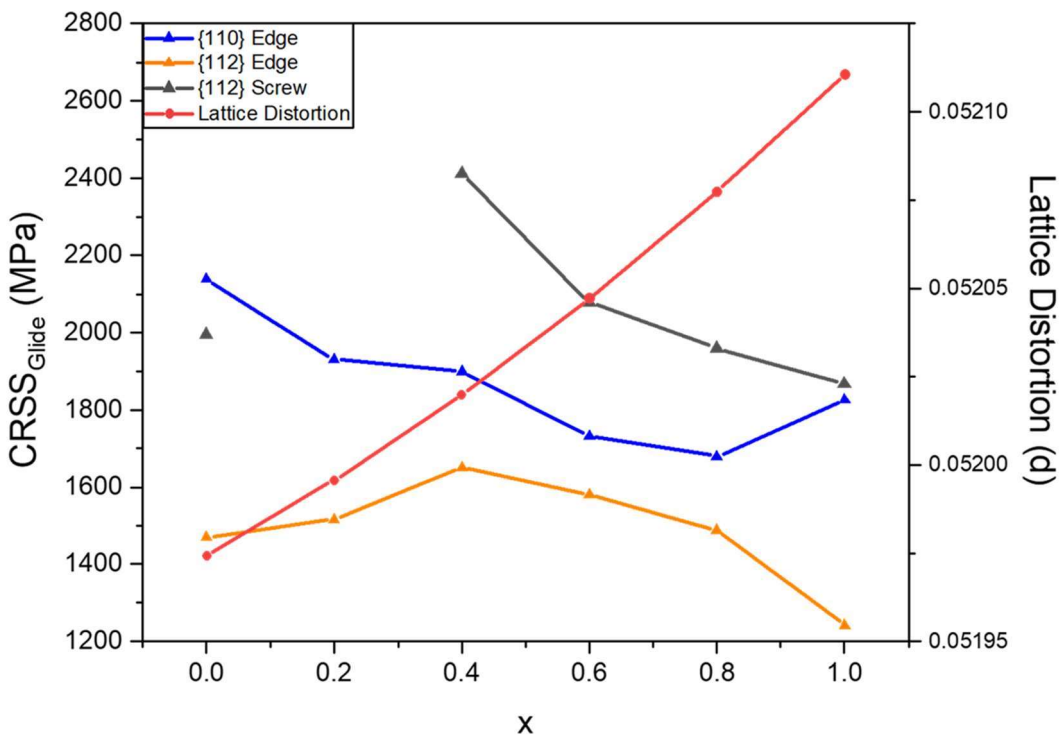


Figure 42: The  $\text{CRSS}_{\text{Glide}}$  and lattice distortion versus plotted as Mo content.

## **Chapter Six: Conclusions**

A series of novel high entropy alloys containing refractory elements including Cr, Mo, Nb, Ta, V, and W were investigated to evaluate their potential use in extreme environments, such as high temperature applications. Both experimental and theoretical techniques were applied to a an alloy family, originally investigated by [23], to evaluate the presented alloys holistically.

A CrNbTaVW alloy was investigated following results reported in [55] that the alloy was able to sustain adequate oxidation until 800<sup>0</sup>C. The interface of the alloy revealed that Cr, Ta, and W were the three main elements to oxidize, but did not indicate any evidence of selective oxidation. The previously identified phases in the microstructure were also able to be identified within the structure. V appeared to stay near the interface and did not appear throughout the oxide scale at the top surface. This was confirmed during surface analysis, as only two distinct oxides were seen at both 700 and 800<sup>0</sup>C, which were an elongated Ta-W oxide and a granular Cr-oxide. There was no V present at the surface and only minimal Nb was seen. The thicknesses of the oxide layers were also measured, from 700 to 800<sup>0</sup>C, the oxide scale nearly tripled in length, indicating that there is a significant amount of oxidation that begins to place at 800<sup>0</sup>C. XRD data revealed complex oxide growth, which begins oxidation around 500<sup>0</sup>C, however shows significant changes beginning at 700<sup>0</sup>C.

For comparison, a CrMoNbTaW alloy was also investigated. The as-fabricated vacuum arc melting structure was evaluated. The microstructure revealed a multiphase microstructure consisting of one W-rich phase, which has a bright, white appearance, and a Mo-rich phase, which has a dark, rounded, black appearance. The two phases are surrounded by a gray matrix of a nearly equiatomic solution of the five constituent elements. The XRD results revealed that the alloy retained a BCC structure and had excellent microhardness values, comparable to or exceeding

values obtained by other RHEAs. The alloy was annealed at 600-900<sup>0</sup>C for 6 hours and revealed no significant changes within the microstructure. The microhardness values of the annealed samples did not differ significantly from the as-fabricated samples, indicating thermal stability and showing no significant softening at elevated temperatures.

Oxidation of the alloy at 12 and 24 hours in the temperature range from 600-1400<sup>0</sup>C initially showed a parabolic mass gain until 1200<sup>0</sup>C, where the mass gain began to decrease and at 1300<sup>0</sup>C experienced mass loss. The alloy was considered to have adequate oxidation resistance up to 1000<sup>0</sup>C. The surface oxidation layers revealed similar structures after both 12 and 24 hours of oxidation at respective temperatures. At 800<sup>0</sup>C the oxide surface began to show a decrease in Mo content on the surface, until which there was little to no Mo seen at the surface beginning around 1100<sup>0</sup>C. As oxidation temperature increased, the oxide morphology became more defined. There were two distinct oxides in the temperature range from 1100-1300<sup>0</sup>C of an elongated Ta-W-Nb oxide and a granular Cr-oxide. At 1400<sup>0</sup>C at both oxidation times, the oxides change to be an elongated Nb-rich oxide with dispersed black, globular oxides of Ta and W. The oxidation characteristics of the two alloys investigated are similar, as they both contain oxidation products resulting from Cr, Ta, and W.

Both alloys indicate decent oxidation resistance at moderate temperatures, however, do not exceed comparable commercially used superalloys, such as Inconel 718. There were no protective oxides identified in either of the alloys, which is believed to be detrimental to the oxidation resistance, especially at elevated temperatures. Though the oxidation resistance does not compare to commercial alloys, the strength values obtained of the as-received CrMoNbTaW alloy indicates a higher strength material compared to Inconel 718. The alloys do show potential for moderate

temperature applications, however, further investigation of mechanical properties, both at room temperature and elevated temperatures, is necessary.

Atomistic simulations of quaternary alloys using MS and MD were conducted to understand the plastic deformation of a series of four alloy compositions. LSR values were calculated to provide information about the preferred slip system. Cr-containing compositions indicated better strength values, which was related to the increased lattice distortion because of the small atomic size relative to the other constituent elements, though had higher values of variation. To expand on the dislocation behavior, a series of  $\text{CrMo}_x\text{NbTaVW}_{1-x}$  alloys were evaluated through MD simulations. Long dislocation lines were evaluated for two main critical stresses: one required to move the dislocation in a void-free lattice and one containing a void. The strengthening effect was the strongest in pure metals along the {110} plane for edge dislocation but was not as significant on the {112} plane for both edge and screw dislocations. In the HEA compositions, the strengthening was not significant because of voids in the lattice. This indicates that the strength of HEAs is not reliant on obstacles that may be present in the lattice. Both studies provide significant insight into the characteristics of these materials which may make it easier to decide on specific compositions for experimental testing.

## References

- [1.] Yeh, J.W., Chen, S.K., Lin, S.J., Gan, J.Y., Chin, T.S., Shun, T.T., Tsau, C.H., Chang, S.Y., 2004. Nanostructured high-entropy alloys with multiple principal elements: Novel alloy design concepts and outcomes. *Adv. Eng. Mater.* 6, 299–303.  
<https://doi.org/10.1002/adem.200300567>
- [2.] Cantor, B., Chang, I.T.H., Knight, P., Vincent, A.J.B., 2004. Microstructural development in equiatomic multicomponent alloys. *Mater. Sci. Eng. A* 375–377, 213–218. <https://doi.org/10.1016/j.msea.2003.10.257>
- [3.] Zhang, C., Gao, M.C., Yeh, J.W., Liaw, P.K. and Zhang, Y., 2016. High-Entropy alloys: fundamentals and applications.
- [4.] Lai KT, Chen SK, Yeh JW, 1998. Properties of the multicomponent alloy system with equal-mole elements. Master's thesis, National Tsing Hua University, Taiwan
- [5.] Hsu YH, Chen SK, Yeh JW, 2000. A study on the multicomponent alloy systems with equal-mole FCC or BCC elements. Master's thesis, National Tsing Hua University, Taiwan
- [6.] Hung YT, Chen SK, Yeh JW, 2001. A study on the Cu-Ni-Al-Co-Cr-Fe-Si-Ti multicomponent alloy system. Master's thesis, National Tsing Hua University, Taiwan
- [7.] Chen KY, Shun TT, Yeh JW, 2002. Development of multi-element high-entropy alloys for spray coating. Master's thesis, National Tsing Hua University, Taiwan
- [8.] Chen KY, Shun TT, Yeh JW, 2002. Development of multi-element high-entropy alloys for spray coating. Master's thesis, National Tsing Hua University, Taiwan
- [9.] Tung CC, Shun TT, Chen SK, Yeh JW, 2002. Study on the deformation microstructure and high temperature properties of Cu-Co-Ni-Cr-Al-Fe. Master's thesis, National Tsing Hua University, Taiwan
- [10.] Chen MJ, Lin SS, 2003. The effect of V, S, and Ti additions on the microstructure and wear properties of Al(0.5)CrCuFeCoNi high-entropy alloys. Master's thesis, National Tsing Hua University, Taiwan
- [11.] Chen MJ, Lin SS, 2003. The effect of V, S, and Ti additions on the microstructure and wear properties of Al(0.5)CrCuFeCoNi high-entropy alloys. Master's thesis, National Tsing Hua University, Taiwan
- [12.] Huang PK, Yeh JW, 2003. Research of multi-component high-entropy alloys for thermal spray coating. Master's thesis, National Tsing Hua University, Taiwan
- [13.] Hsu CY, Shun TT, Chen SK, Yeh JW, 2003. Alloying effect of boron on the microstructure and high-temperature properties of CuCoNiCrAl0.5Fe alloys. Master's thesis, National Tsing Hua University, Taiwan.
- [14.] Lin PC, Chin TS, Yeh JW, 2003. Development on the high frequency soft-magnetic thin films from high-entropy alloys. Master's thesis, National Tsing Hua University, Taiwan
- [15.] Tsai CW, Shun TT, Yeh JW, 2003. Study on the deformation behavior and microstructure of CuCoNiCrAlxFe high-entropy alloys. Master's thesis, National Tsing Hua University, Taiwan

- [16.] Miracle, D.B., Senkov, O.N., 2017. A critical review of high entropy alloys and related concepts. *Acta Mater.* 122, 448–511. <https://doi.org/10.1016/j.actamat.2016.08.081>
- [17.] Yeh, J.W., 2006. Recent progress in high-entropy alloys. *Ann. Chim. Sci. des Mater.* 31, 633–648. <https://doi.org/10.3166/acsm.31.633-648>
- [18.] Yeh, J.W., 2013. Alloy design strategies and future trends in high-entropy alloys. *Jom* 65, 1759–1771. <https://doi.org/10.1007/s11837-013-0761-6>
- [19.] Yeh, J.W., 2015. Physical Metallurgy of High-Entropy Alloys. *Jom* 67, 2254–2261. <https://doi.org/10.1007/s11837-015-1583-5>
- [20.] Tsai, K.Y., Tsai, M.H., Yeh, J.W., 2013. Sluggish diffusion in Co-Cr-Fe-Mn-Ni high-entropy alloys. *Acta Mater.* 61, 4887–4897. <https://doi.org/10.1016/j.actamat.2013.04.058>
- [21.] Ranganathan, S., 2003. Alloyed pleasures: Multimetallic cocktails. *Curr. Sci.* 85, 1404–1406.
- [22.] Savitskii, E.M., 2012. Physical metallurgy of refractory metals and alloys. Springer Science & Business Media.
- [23.] Senkov, O.N., Wilks, G.B., Miracle, D.B., Chuang, C.P., Liaw, P.K., 2010. Refractory high-entropy alloys. *Intermetallics* 18, 1758–1765. <https://doi.org/10.1016/j.intermet.2010.05.014>
- [24.] Senkov, O.N., Miracle, D.B., Chaput, K.J., Couzinie, J.P., 2018. Development and exploration of refractory high entropy alloys - A review. *J. Mater. Res.* 33, 3092–3128. <https://doi.org/10.1557/jmr.2018.153>
- [25.] Samsonov, G.V., 2013. The oxide handbook. Springer Science & Business Media.
- [26.] The Minerals, Metals & Materials Society (TMS), Defining Pathways for Realizing the Revolutionary Potential of High Entropy Alloys (Pittsburgh, PA: TMS 2021).
- [27.] Dada, M., Popoola, P., Mathe, N., 2021. Recent advances of high entropy alloys for aerospace applications: a review. *World J. Eng.* <https://doi.org/10.1108/WJE-01-2021-0040>
- [28.] Zinkle, S.J., Was, G.S., 2013. Materials challenges in nuclear energy. *Acta Mater.* 61, 735–758. <https://doi.org/10.1016/j.actamat.2012.11.004>
- [29.] Barron, P.J., Carruthers, A.W., Fellowes, J.W., Jones, N.G., Dawson, H., Pickering, E.J., 2020. Towards V-based high-entropy alloys for nuclear fusion applications. *Scr. Mater.* 176, 12–16. <https://doi.org/10.1016/j.scriptamat.2019.09.028>
- [30.] Kareer, A., Waite, J.C., Li, B., Couet, A., Armstrong, D.E.J., Wilkinson, A.J., 2019. Short communication: ‘Low activation, refractory, high entropy alloys for nuclear applications.’ *J. Nucl. Mater.* 526, 0–5. <https://doi.org/10.1016/j.jnucmat.2019.151744>
- [31.] Pickering, E.J., Carruthers, A.W., Barron, P.J., Middleburgh, S.C., Armstrong, D.E.J., Gandy, A.S., 2021. High-entropy alloys for advanced nuclear applications. *Entropy* 23, 1–28. <https://doi.org/10.3390/e23010098>
- [32.] Waseem, O.A., Ryu, H.J., 2017. Powder Metallurgy Processing of a W<sub>x</sub>TaTiVCr High-Entropy Alloy and Its Derivative Alloys for Fusion Material Applications. *Sci. Rep.* 7, 1–14. <https://doi.org/10.1038/s41598-017-02168-3>
- [33.] Ostovari Moghaddam, A., Pasandideh, J., Abdollahzadeh, A., Shaburova, N.A., Trofimov, E., 2021. On the application of NbTaTiVW refractory high entropy alloy

- particles in the manufacturing process of WC based matrix body drill bits. *Int. J. Refract. Met. Hard Mater.* 99, 105608. <https://doi.org/10.1016/j.ijrmhm.2021.105608>
- [34.] Popescu, G., Ghiban, B., Popescu, C.A., Rosu, L., Trusca, R., Carcea, I., Soare, V., Dumitrescu, D., Constantin, I., Olaru, M.T., Carlan, B.A., 2018. New TiZrNbTaFe high entropy alloy used for medical applications. *IOP Conf. Ser. Mater. Sci. Eng.* 400. <https://doi.org/10.1088/1757-899X/400/2/022049>
- [35.] Senkov, O.N., Wilks, G.B., Scott, J.M., Miracle, D.B., 2011. Mechanical properties of Nb25Mo25Ta 25W25 and V20Nb20Mo 20Ta20W20 refractory high entropy alloys. *Intermetallics* 19, 698–706. <https://doi.org/10.1016/j.intermet.2011.01.004>
- [36.] Yao, H., Qiao, J.W., Gao, M.C., Hawk, J.A., Ma, S.G., Zhou, H., 2016. MoNbTaV medium-entropy alloy. *Entropy* 18, 1–15. <https://doi.org/10.3390/e18050189>
- [37.] Han, Z.D., Luan, H.W., Liu, X., Chen, N., Li, X.Y., Shao, Y., Yao, K.F., 2018. Microstructures and mechanical properties of  $TixNbMoTaW$  refractory high-entropy alloys. *Mater. Sci. Eng. A* 712, 380–385. <https://doi.org/10.1016/j.msea.2017.12.004>
- [38.] Waseem, O.A., Lee, J., Lee, H.M., Ryu, H.J., 2018. The effect of Ti on the sintering and mechanical properties of refractory high-entropy alloy  $TixWTaVCr$  fabricated via spark plasma sintering for fusion plasma-facing materials. *Mater. Chem. Phys.* 210, 87–94. <https://doi.org/10.1016/j.matchemphys.2017.06.054>
- [39.] Kang, B., Lee, J., Ryu, H.J., Hong, S.H., 2018. Ultra-high strength WNbMoTaV high-entropy alloys with fine grain structure fabricated by powder metallurgical process. *Mater. Sci. Eng. A* 712, 616–624. <https://doi.org/10.1016/j.msea.2017.12.021>
- [40.] Han, Z.D., Chen, N., Zhao, S.F., Fan, L.W., Yang, G.N., Shao, Y., Yao, K.F., 2017. Effect of Ti additions on mechanical properties of NbMoTaW and VNbMoTaW refractory high entropy alloys. *Intermetallics* 84, 153–157. <https://doi.org/10.1016/j.intermet.2017.01.007>
- [41.] Zhang, B., Gao, M.C., Zhang, Y., Guo, S.M., 2015. Senary refractory high-entropy alloy CrxMoNbTaVW. *Calphad Comput. Coupling Phase Diagrams Thermochem.* 51, 193–201. <https://doi.org/10.1016/j.calphad.2015.09.007>
- [42.] Yao, H.W., Qiao, J.W., Gao, M.C., Hawk, J.A., Ma, S.G., Zhou, H.F., Zhang, Y., 2016. NbTaV-(Ti,W) refractory high-entropy alloys: Experiments and modeling. *Mater. Sci. Eng. A* 674, 203–211. <https://doi.org/10.1016/j.msea.2016.07.102>
- [43.] Senkov, O.N., Woodward, C.F., 2011. Microstructure and properties of a refractory  $NbCrMo0.5Ta0.5TiZr$  alloy. *Mater. Sci. Eng. A* 529, 311–320. <https://doi.org/10.1016/j.msea.2011.09.033>
- [44.] Chen, J., Zhou, X., Wang, W., Liu, B., Lv, Y., Yang, W., Xu, D., Liu, Y., 2018. A review on fundamental of high entropy alloys with promising high-temperature properties. *J. Alloys Compd.* 760, 15–30. <https://doi.org/10.1016/j.jallcom.2018.05.067>
- [45.] Couzinié, J.P., Senkov, O.N., Miracle, D.B., Dirras, G., 2018. Comprehensive data compilation on the mechanical properties of refractory high-entropy alloys. *Data Br.* 21, 1622–1641. <https://doi.org/10.1016/j.dib.2018.10.071>
- [46.] Gulbransen, E.A., Andrew, K.F., Brassart, F.A., 1963. Oxidation of Molybdenum 550° to 1700°C. *J. Electrochem. Soc.* 110, 952. <https://doi.org/10.1149/1.2425918>

- [47.] Liu, C.M., Wang, H.M., Zhang, S.Q., Tang, H.B., Zhang, A.L., 2014. Microstructure and oxidation behavior of new refractory high entropy alloys. *J. Alloys Compd.* 583, 162–169. <https://doi.org/10.1016/j.jallcom.2013.08.102>
- [48.] Gulbransen, E.A., Andrew, K.F., 1960. Kinetics of the Oxidation of Pure Tungsten from 500° to 1300°C. *J. Electrochem. Soc.* 107, 619. <https://doi.org/10.1149/1.2427787>
- [49.] Perkins, R.A., Meier, G.H., 1990. The oxidation behavior and protection of niobium. *Jom* 42, 17–21. <https://doi.org/10.1007/BF03221046>
- [50.] Lo, K.C., Chang, Y.J., Murakami, H., Yeh, J.W., Yeh, A.C., 2019. An oxidation resistant refractory high entropy alloy protected by CrTaO<sub>4</sub>-based oxide. *Sci. Rep.* 9, 3–4. <https://doi.org/10.1038/s41598-019-43819-x>
- [51.] Gorr, B., Azim, M., Christ, H.J., Mueller, T., Schliephake, D., Heilmaier, M., 2015. Phase equilibria, microstructure, and high temperature oxidation resistance of novel refractory high-entropy alloys. *J. Alloys Compd.* 624, 270–278. <https://doi.org/10.1016/j.jallcom.2014.11.012>
- [52.] Gorr, B., Mueller, F., Christ, H.J., Mueller, T., Chen, H., Kauffmann, A., Heilmaier, M., 2016. High temperature oxidation behavior of an equimolar refractory metal-based alloy 20Nb-20Mo-20Cr-20Ti-20Al with and without Si addition. *J. Alloys Compd.* 688, 468–477. <https://doi.org/10.1016/j.jallcom.2016.07.219>
- [53.] Chan, K.S., 2004. Cyclic oxidation response of multiphase niobium-based alloys. *Metall. Mater. Trans. A Phys. Metall. Mater. Sci.* 35 A, 589–597. <https://doi.org/10.1007/s11661-004-0370-7>
- [54.] Xiao, Y., Kuang, W., Xu, Y., Wu, L., Gong, W., Qian, J., Zhang, Q., He, Y., 2019. Microstructure and oxidation behavior of the CrMoNbTaV high-entropy alloy. *J. Mater. Res.* 34, 301–308. <https://doi.org/10.1557/jmr.2018.340>
- [55.] Varma, S.K., Sanchez, F., Moncayo, S., Ramana, C. V., 2020. Static and cyclic oxidation of Nb-Cr-V-W-Ta high entropy alloy in air from 600 to 1400 °C. *J. Mater. Sci. Technol.* 38, 189–196. <https://doi.org/10.1016/j.jmst.2019.09.005>
- [56.] Choi, W.J., Park, C.W., Song, Y., Choi, H., Byun, J., Kim, Y. Do, 2020. Oxidation Behavior of Pack-Cemented Refractory High-Entropy Alloy. *Jom* 72, 4594–4603. <https://doi.org/10.1007/s11837-020-04439-3>
- [57.] Gorr, B., Müller, F., Azim, M., Christ, H.J., Müller, T., Chen, H., Kauffmann, A., Heilmaier, M., 2017. High-Temperature Oxidation Behavior of Refractory High-Entropy Alloys: Effect of Alloy Composition. *Oxid. Met.* 88, 339–349. <https://doi.org/10.1007/s11085-016-9696-y>
- [58.] Osei-Agyemang, E., Balasubramanian, G., 2019. Surface oxidation mechanism of a refractory high-entropy alloy. *npj Mater. Degrad.* 3. <https://doi.org/10.1038/s41529-019-0082-5>
- [59.] Butler, T.M., 2021. High Entropy Alloys: Oxidation. *Encycl. Mater. Met. Alloy.* 2, 522–532. <https://doi.org/10.1016/B978-0-12-803581-8.12126-5>
- [60.] Varma, S.K., Sanchez, F., Ramana, C. V., 2020. Journal of Materials Science & Technology Microstructures in a Nb-Cr-V-W-Ta high entropy alloy during annealing. *J. Mater. Sci. Technol.* 53, 66–72. <https://doi.org/10.1016/j.jmst.2020.03.028>

- [61.] Wan, Y., Mo, J., Wang, X., Zhang, Z., Shen, B., Liang, X., 2021. Mechanical Properties and Phase Stability of WTaMoNbTi Refractory High-Entropy Alloy at Elevated Temperatures. *Acta Metall. Sin. (English Lett.)* 34, 1585–1590.  
<https://doi.org/10.1007/s40195-021-01263-9>
- [62.] Pandey, V.K., Shadangi, Y., Shivam, V., Sarma, B.N., Mukhopadhyay, N.K., 2021. Theoretical and experimental study on phase stability of TiVZrMoW refractory high entropy alloy. *Philos. Mag.* 0, 1–24. <https://doi.org/10.1080/14786435.2021.2001066>
- [63.] Yao, J.Q., Liu, X.W., Gao, N., Jiang, Q.H., Li, N., Liu, G., Zhang, W.B., Fan, Z.T., 2018. Phase stability of a ductile single-phase BCC Hf0.5Nb0.5Ta0.5Ti1.5Zr refractory high-entropy alloy. *Intermetallics* 98, 79–88.  
<https://doi.org/10.1016/j.intermet.2018.04.023>
- [64.] Chen, S.Y., Tong, Y., Tseng, K.K., Yeh, J.W., Poplawsky, J.D., Wen, J.G., Gao, M.C., Kim, G., Chen, W., Ren, Y., Feng, R., Li, W.D., Liaw, P.K., 2019. Phase transformations of HfNbTaTiZr high-entropy alloy at intermediate temperatures. *Scr. Mater.* 158, 50–56.  
<https://doi.org/10.1016/j.scriptamat.2018.08.032>
- [65.] Schneider, M., George, E. P., Manescu, T. J., Záležák, T., Hunfeld, J., Dlouhý, A., ... & Laplanche, G. (2020). Analysis of strengthening due to grain boundaries and annealing twin boundaries in the CrCoNi medium-entropy alloy. *International Journal of Plasticity*, 124, 155–169.
- [66.] Hasan, M.N., Liu, Y.F., An, X.H., Gu, J., Song, M., Cao, Y., Li, Y.S., Zhu, Y.T., Liao, X.Z., 2019. Simultaneously enhancing strength and ductility of a high-entropy alloy via gradient hierarchical microstructures. *Int. J. Plast.* 123, 178–195.  
<https://doi.org/10.1016/j.ijplas.2019.07.017>
- [67.] Ming, K., Bi, X., Wang, J., 2019. Strength and ductility of CrFeCoNiMo alloy with hierarchical microstructures. *Int. J. Plast.* 113, 255–268.  
<https://doi.org/10.1016/j.ijplas.2018.10.005>
- [68.] Fang, Q., Chen, Y., Li, J., Jiang, C., Liu, B., Liu, Y., Liaw, P.K., 2019. Probing the phase transformation and dislocation evolution in dual-phase high-entropy alloys. *Int. J. Plast.* 114, 161–173. <https://doi.org/10.1016/j.ijplas.2018.10.014>
- [69.] Hua, D., Xia, Q., Wang, W., Zhou, Q., Li, S., Qian, D., Shi, J., Wang, H., 2021. Atomistic insights into the deformation mechanism of a CoCrNi medium entropy alloy under nanoindentation. *Int. J. Plast.* 142, 102997.  
<https://doi.org/10.1016/j.ijplas.2021.102997>
- [70.] Smith, L.T.W., Su, Y., Xu, S., Hunter, A., Beyerlein, I.J., 2020. The effect of local chemical ordering on Frank-Read source activation in a refractory multi-principal element alloy. *Int. J. Plast.* 134, 102850. <https://doi.org/10.1016/j.ijplas.2020.102850>
- [71.] George, E.P., Raabe, D., Ritchie, R.O., 2019. High-entropy alloys. *Nat. Rev. Mater.* 4, 515–534. <https://doi.org/10.1038/s41578-019-0121-4>
- [72.] Mitchell, T.E., 1968. Slip in body-centred cubic crystals. *Philos. Mag.* 17, 1169–1194.  
<https://doi.org/10.1080/14786436808223194>
- [73.] Zhou, S. J., Carlsson, A. E., & Thomson, R. (1994). Dislocation core-core interaction and Peierls stress in a model hexagonal lattice. *Phys. Rev. B*, 49, 6451.  
<https://doi.org/10.1103/PhysRevB.49.6451>

- [74.] Wang, F., Balbus, G.H., Xu, S., Su, Y., Shin, J., Rottmann, P.F., Knipling, K.E., Stinville, J.C., Mills, L.H., Senkov, O.N., Beyerlein, I.J., Pollock, T.M., Gianola, D.S., 2020. Multiplicity of dislocation pathways in a refractory multiprincipal element alloy. *Science*. 370, 95–101. <https://doi.org/10.1126/science.aba3722>
- [75.] Liu, X., Pei, Z., Eisenbach, M., 2019. Dislocation core structures and Peierls stresses of the high-entropy alloy NiCoFeCrMn and its subsystems. *Mater. Des.* 180, 107955. <https://doi.org/10.1016/j.matdes.2019.107955>
- [76.] Aitken, Z.H., Sorkin, V., Zhang, Y.W., 2019. Atomistic modeling of nanoscale plasticity in high-entropy alloys. *J. Mater. Res.* 34, 1509–1532. <https://doi.org/10.1557/jmr.2019.50>
- [77.] Pei, Z., 2018. An overview of modeling the stacking faults in lightweight and high-entropy alloys: Theory and application. *Mater. Sci. Eng. A* 737, 132–150. <https://doi.org/10.1016/j.msea.2018.09.028>
- [78.] Huang, R., Zhang, Q., Zhang, X., Li, J., Cao, T., Yao, J., Xue, Y., Gao, H. and Li, X., 2021. Dynamic recrystallization-induced temperature insensitivity of yield stress in single-crystal Al1.2 CrFeCoNi micropillars. *Sci. China Tech. Sci.*, 64, 11-22. <https://doi.org/10.1007/s11431-020-1660-1>
- [79.] Zhang, Q., Huang, R., Zhang, X., Cao, T., Xue, Y. and Li, X., 2021. Deformation Mechanisms and Remarkable Strain Hardening in Single-Crystalline High-Entropy-Alloy Micropillars/Nanopillars. *Nano Letters*. 21, 3671-3679. <https://doi.org/10.1021/acs.nanolett.1c00444>
- [80.] Hull, Derek, and D. J. Bacon., 2011. Introduction to Dislocations. 5th ed. Elsevier Science.
- [81.] Vitek, V., 2011. Atomic level computer modelling of crystal defects with emphasis on dislocations: Past, present and future. *Prog. Mater. Sci.* 56, 577–585. <https://doi.org/10.1016/j.pmatsci.2011.01.002>
- [82.] Vitek, V., 1992. Structure of dislocation cores in metallic materials and its impact on their plastic behaviour. *Prog. Mater. Sci.* 36, 1–27. [https://doi.org/10.1016/0079-6425\(92\)90003-P](https://doi.org/10.1016/0079-6425(92)90003-P)
- [83.] Mayahi, R., 2020. An investigation concerning generalized stacking fault behavior of Al<sub>x</sub>Cr<sub>2-x</sub>FeNi ( $0.25 \leq x \leq 2$ ) high entropy alloys: Insights from first-principles study. *J. Alloys Compd.* 818, 152928. <https://doi.org/10.1016/j.jallcom.2019.152928>
- [84.] Zhao, Q., Li, J., Fang, Q., Feng, H., 2019. Effect of Al solute concentration on mechanical properties of Al<sub>x</sub>FeCuCrNi high-entropy alloys: A first-principles study. *Phys. B Condens. Matter* 566, 30–37. <https://doi.org/10.1016/j.physb.2019.04.025>
- [85.] Hayakawa, S., Doihara, K., Okita, T., Itakura, M., Aichi, M., Suzuki, K., 2019. Screw dislocation–spherical void interactions in fcc metals and their dependence on stacking fault energy. *J. Mater. Sci.* 54, 11509–11525. <https://doi.org/10.1007/s10853-019-03716-0>
- [86.] Xu, S., McDowell, D.L., Beyerlein, I.J., 2019. Sequential obstacle interactions with dislocations in a planar array. *Acta Mater.* 174, 160–172. <https://doi.org/10.1016/j.actamat.2019.05.030>

- [87.] Xu, S., Cheng, J.Y., Li, Z., Mara, N.A. and Beyerlein, I.J., 2022. Phase-field modeling of the interactions between an edge dislocation and an array of obstacles. Computer Methods in Applied Mechanics and Engineering, 389, p.114426.
- [88.] Hidnert, P. (1929) Thermal expansion of tantalum. Bur. Stand. J. Res., 2 (5), 887
- [89.] Hidnert, P., and Sweeney, W.T. (1925) Thermal expansion of tungsten. Sci. Pap. Bur. Stand., 20, 483.
- [90.] Greene, G.A. and Finfrock, C.C., 2001. Oxidation of Inconel 718 in air at high temperatures. Oxidation of metals, 55(5), 505-521.  
<https://doi.org/10.1023/A:1010359815550>
- [91.] Lin, Z., Johnson, R.A., Zhigilei, L. V., 2008. Computational study of the generation of crystal defects in a bcc metal target irradiated by short laser pulses. Phys. Rev. B - Condens. Matter Mater. Phys. 77, 1–15. <https://doi.org/10.1103/PhysRevB.77.214108>
- [92.] Zhou, X.W., Johnson, R.A., Wadley, H.N.G., 2004. Misfit-energy-increasing dislocations in vapor-deposited CoFe/NiFe multilayers. Phys. Rev. B - Condens. Matter Mater. Phys. 69, 1–10. <https://doi.org/10.1103/PhysRevB.69.144113>
- [93.] Lin, D.Y., Wang, S.S., Peng, D.L., Li, M., Hui, X.D., 2013. Erratum: An n-body potential for a Zr-Nb system based on the embedded-atom-method (Journal of Physics Condensed Matter (2013) 25 (105404)). J. Phys. Condens. Matter 25.  
<https://doi.org/10.1088/0953-8984/25/20/209501>
- [94.] Ghafarollahi, A., Maresca, F., Curtin, W.A., 2019. Solute/screw dislocation interaction energy parameter for strengthening in bcc dilute to high entropy alloys. Model. Simul. Mater. Sci. Eng. 27. <https://doi.org/10.1088/1361-651X/ab4969>
- [95.] Johnson, R.A., 1989. Alloy models with the embedded-atom method. Phys. Rev. B 39, 12554–12559. <https://doi.org/10.1103/PhysRevB.39.12554>
- [96.] Zhou, X.W., Wadley, H.N.G., Johnson, R.A., Larson, D.J., Tabat, N., Cerezo, A., Petford-Long, A.K., Smith, G.D.W., Clifton, P.H., Martens, R.L., Kelly, T.F., 2001. Atomic scale structure of sputtered metal multilayers. Acta Mater. 49, 4005–4015.  
[https://doi.org/10.1016/S1359-6454\(01\)00287-7](https://doi.org/10.1016/S1359-6454(01)00287-7)
- [97.] Maresca, F., Curtin, W.A., 2020. Mechanistic origin of high strength in refractory BCC high entropy alloys up to 1900K. Acta Mater. 182, 235–249.  
<https://doi.org/10.1016/j.actamat.2019.10.015>
- [98.] Varvenne, C., Luque, A., Nöhring, W.G., Curtin, W.A., 2016. Average-atom interatomic potential for random alloys. Phys. Rev. B 93, 1–7.  
<https://doi.org/10.1103/PhysRevB.93.104201>
- [99.] Zunger, A., Wei, S.H., Ferreira, L.G., Bernard, J.E., 1990. Special Quasirandom Structures. Phys. Rev. Lett. 65, 353-356. <https://doi.org/10.1103/PhysRevLett.65.353>
- [100.] Van De Walle, A., Tiwary, P., De Jong, M., Olmsted, D.L., Asta, M., Dick, A., Shin, D., Wang, Y., Chen, L.Q., Liu, Z.K., 2013. Efficient stochastic generation of special quasirandom structures. Calphad Comput. Coupling Phase Diagrams Thermochem. 42, 13–18. <https://doi.org/10.1016/j.calphad.2013.06.006>
- [101.] Xu, S., Chavoshi, S.Z. and Su, Y., 2022. On calculations of basic structural parameters in multi-principal element alloys using small atomistic models. Computational Materials Science, 202, p.110942. <https://doi.org/10.1016/j.actamat.2020.10.042>

- [102.] Kumar, A., Kedjar, B., Su, Y., Thilly, L., Beyerlein, I.J., 2020. Atomic-level calculations and experimental study of dislocations in InSb. *J. Appl. Phys.* 127. <https://doi.org/10.1063/1.5139285>
- [103.] Xu, S., Hwang, E., Jian, W.R., Su, Y., Beyerlein, I.J., 2020. Atomistic calculations of the generalized stacking fault energies in two refractory multi-principal element alloys. *Intermetallics* 124, 106844. <https://doi.org/10.1016/j.intermet.2020.106844>
- [104.] Warlimont, Hans, and Werner Martienssen, eds., 2018. Springer handbook of materials data. Springer.
- [105.] Yao, H.W., Qiao, J.W., Gao, M.C., Hawk, J.A., Ma, S.G., Zhou, H.F., Zhang, Y., 2016. NbTaV-(Ti,W) refractory high-entropy alloys: Experiments and modeling. *Mater. Sci. Eng. A* 674, 203–211. <https://doi.org/10.1016/j.msea.2016.07.102>
- [106.] Li, X.G., Chen, C., Zheng, H., Zuo, Y., Ong, S.P., 2020. Complex strengthening mechanisms in the NbMoTaW multi-principal element alloy. *npj Comput. Mater.* 6, 1–10. <https://doi.org/10.1038/s41524-020-0339-0>
- [107.] Xu, S., Su, Y., Smith, L.T.W., Beyerlein, I.J., 2020. Frank-Read source operation in six body-centered cubic refractory metals. *J. Mech. Phys. Solids* 141, 104017. <http://dx.doi.org/10.1016/j.jmps.2020.104017>
- [108.] Wang, X., Xu, S., Jian, W.R., Li, X.G., Su, Y., Beyerlein, I.J., 2021. Generalized stacking fault energies and Peierls stresses in refractory body-centered cubic metals from machine learning-based interatomic potentials. *Comput. Mater. Sci.* 192, 110364. <https://doi.org/10.1016/j.commatsci.2021.110364>
- [109.] Xu, S., Su, Y., Jian, W.R., Beyerlein, I.J., 2021. Local slip resistances in equal-molar MoNbTi multi-principal element alloy. *Acta Mater.* 202, 68–79. <https://doi.org/10.1016/j.actamat.2020.10.042>
- [110.] Srivastava, K., Gröger, R., Weygand, D., Gumbsch, P., 2013. Dislocation motion in tungsten: Atomistic input to discrete dislocation simulations. *Int. J. Plast.* 47, 126–142. <https://doi.org/10.1016/j.ijplas.2013.01.014>
- [111.] Lim, H., Weinberger, C.R., Battaile, C.C., Buchheit, T.E., 2013. Application of generalized non-Schmid yield law to low-temperature plasticity in bcc transition metals. *Model. Simul. Mater. Sci. Eng.* 21, 045015. <https://doi.org/10.1088/0965-0393/21/4/045015>
- [112.] Yin, S., Zuo, Y., Abu-Odeh, A., Zheng, H., Li, X.G., Ding, J., Ong, S.P., Asta, M., Ritchie, R.O., 2021. Atomistic simulations of dislocation mobility in refractory high-entropy alloys and the effect of chemical short-range order. *Nat. Commun.* 12, 1–14. <https://doi.org/10.1038/s41467-021-25134-0>
- [113.] Chen, B., Li, S., Zong, H., Ding, X., Sun, J., Ma, E., 2020. Unusual activated processes controlling dislocation motion in body-centered-cubic high-entropy alloys. *Proc. Natl. Acad. Sci. U. S. A.* 117, 16199–16206. <https://doi.org/10.1073/pnas.1919136117>
- [114.] Song, H., Tian, F., Hu, Q.M., Vitos, L., Wang, Y., Shen, J., Chen, N., 2017. Local lattice distortion in high-entropy alloys. *Phys. Rev. Mater.* 1, 1–8. <https://doi.org/10.1103/PhysRevMaterials.1.023404>

- [115.] Lee, C., Chou, Y., Kim, G., Gao, M.C., An, K., Brechtl, J., Zhang, C., Chen, W., Poplawsky, J.D., Song, G., Ren, Y., Chou, Y.C., Liaw, P.K., 2020. Lattice-Distortion-Enhanced Yield Strength in a Refractory High-Entropy Alloy. *Adv. Mater.* 32, 1–9. <https://doi.org/10.1002/adma.202004029>
- [116.] Oh, H.S., Odbadrakh, K., Ikeda, Y., Mu, S., Körmann, F., Sun, C.J., Ahn, H.S., Yoon, K.N., Ma, D., Tasan, C.C., Egami, T., Park, E.S., 2021. Element-resolved local lattice distortion in complex concentrated alloys: An observable signature of electronic effects. *Acta Mater.* 216, 117135. <https://doi.org/10.1016/j.actamat.2021.117135>
- [117.] Li, L., Fang, Q., Li, J., Liu, B., Liu, Y., Liaw, P.K., 2020. Lattice-distortion dependent yield strength in high entropy alloys. *Mater. Sci. Eng. A* 784. <https://doi.org/10.1016/j.msea.2020.139323>
- [118.] Roy, A., Sreeramagiri, P., Babuska, T., Krick, B., Ray, P.K., Balasubramanian, G., 2021. Lattice distortion as an estimator of solid solution strengthening in high-entropy alloys. *Mater. Charact.* 172, 110877. <https://doi.org/10.1016/j.matchar.2021.110877>
- [119.] Kim, I.H., Oh, H.S., Lee, K.S., Park, E.S., 2021. Optimization of conflicting properties via engineering compositional complexity in refractory high entropy alloys. *Scr. Mater.* 199, 113839. <https://doi.org/10.1016/j.scriptamat.2021.113839>
- [120.] Kim, I.H., Oh, H.S., Kim, S.J., Park, E.S., 2021. Rapid assessment of solid solution hardening via atomic size misfit parameter in refractory concentrated alloys. *J. Alloys Compd.* 886, 161320. <https://doi.org/10.1016/j.jallcom.2021.161320>
- [121.] Li, J., Chen, H., Fang, Q., Jiang, C., Liu, Y., Liaw, P.K., 2020c Unraveling the dislocation-precipitate interactions in high-entropy alloys. *Int. J. Plast.* 133, 102819. <https://doi.org/10.1016/j.ijplas.2020.102819>
- [122.] Zhao, Y.Y., Nieh, T.G., 2017. Correlation between lattice distortion and friction stress in Ni-based equiatomic alloys. *Intermetallics.* 86, 45–50. <https://doi.org/10.1016/j.intermet.2017.03.011>
- [123.] Ali, M. L., Shinzato, S., Wang, V., Shen, Z., Du, J. P., Ogata, S., 2020. An Atomistic Modeling Study of the Relationship between Critical Resolved Shear Stress and Atomic Structure Distortion in FCC High Entropy Alloys-Relationship in Random Solid Solution and Chemical-Short-Range-Order Alloys. *Matr. Trans.* 61, 605. <https://doi.org/10.2320/matertrans.MT-MK2019007>
- [124.] S. Xu, L. Smith, J. R. Mianroodi, A. Hunter, B. Svendsen, and I. J. Beyerlein, 2019. A comparison of different continuum approaches in modeling mixed-type dislocations in Al,” *Modell. Simul. Mater. Sci. Eng.* 27, 074004. <https://doi.org/10.1088/1361-651X/ab2d16>
- [125.] S. Xu, Y. Su, and I. J. Beyerlein, 2019. Modeling dislocations with arbitrary character angle in face-centered cubic transition metals using the phase-field dislocation dynamics method with full anisotropic elasticity,” *Mech. Mater.* 139, 103200. <https://doi.org/10.1016/j.mechmat.2019.103200>
- [126.] Jian, W.R., Zhang, M., Xu, S., Beyerlein, I.J., 2020. Atomistic simulations of dynamics of an edge dislocation and its interaction with a void in copper: a comparative study. *Model. Simul. Mater. Sci. Eng.* 28. <https://doi.org/10.1088/1361-651X/ab8358>

## Vita

Rebecca Alexandra Romero earned her Bachelor of Science in Metallurgical and Materials Engineering from the University of Texas at El Paso in 2019. She received a Postgraduate Diploma in Subsea and Pipeline Engineering from the University of Strathclyde in Glasgow, Scotland in 2019. In the fall of 2019, she joined the doctoral program in Materials Science and Engineering.

Throughout her academic career, Rebecca has worked a multitude of jobs, from co-ops and internships with Halliburton Drill Bits and Services to Nucor Steel. Most recently, she has joined the Future Leaders in Advanced Materials (FLAM) program in coordination with the University of California, Santa Barbara for both the summer of 2020 and 2021. During her time as a graduate student, she also worked as a teaching assistant, research assistant, and as a graduate fellow with the Nuclear Regulatory Commission. She also worked as a tutor for most of her academic career.

After graduation, she will move to Rockville, Maryland to continue her career with the Nuclear Regulatory Commission as a part of the Nuclear Regulatory Apprenticeship Network. Her passion for materials runs in the family and is proud to continue the metallurgy legacy. She has a passion for teaching and helping others learn and would like to incorporate that into her future career.

ProQuest Number: 29208466

INFORMATION TO ALL USERS

The quality and completeness of this reproduction is dependent on the quality  
and completeness of the copy made available to ProQuest.



Distributed by ProQuest LLC (2022).

Copyright of the Dissertation is held by the Author unless otherwise noted.

This work may be used in accordance with the terms of the Creative Commons license  
or other rights statement, as indicated in the copyright statement or in the metadata  
associated with this work. Unless otherwise specified in the copyright statement  
or the metadata, all rights are reserved by the copyright holder.

This work is protected against unauthorized copying under Title 17,  
United States Code and other applicable copyright laws.

Microform Edition where available © ProQuest LLC. No reproduction or digitization  
of the Microform Edition is authorized without permission of ProQuest LLC.

ProQuest LLC  
789 East Eisenhower Parkway  
P.O. Box 1346  
Ann Arbor, MI 48106 - 1346 USA